

REPORT SAMSO-TR-78-99

LEVEL II

②

ADA057929

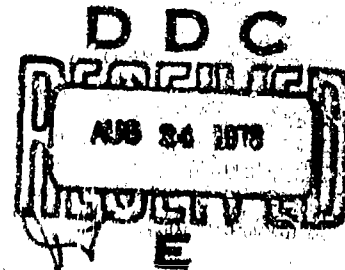
The Challenge of Reentry Vehicle Instrumentation

Prepared by P. J. LEGENDRE, W. R. GRABOWSKY, R. G. FOWLER
Reentry Systems Division
The Aerospace Corporation
and
J. M. CASSANTO
General Electric Company

31 May 1978

Interim Report

APPROVED FOR PUBLIC RELEASE;
DISTRIBUTION UNLIMITED



AD NO.

DDC FILE COPY

Prepared for

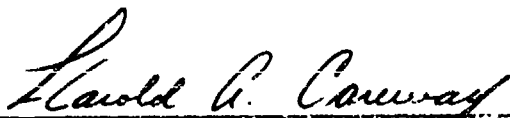
SPACE AND MISSILE SYSTEMS ORGANIZATION
AIR FORCE SYSTEMS COMMAND
Los Angeles Air Force Station
P.O. Box 92960, Worldway Postal Center
Los Angeles, Calif. 90009

78 17 08 102

This interim report was submitted by The Aerospace Corporation, El Segundo, CA 90245, under Contract F04701-77-C-0078 with the Space and Missile Systems Organization, Deputy for Reentry Systems, P. O. Box 92960, Worldway Postal Center, Los Angeles, CA 90009. It was reviewed and approved for The Aerospace Corporation by R. E. Herold, Reentry Systems Division. The project officer was Capt. Harold A. Careway, SAMSO (RSSE).

This report has been reviewed by the Information Office (OI) and is releasable to the National Technical Information Service (NTIS). At NTIS, it will be available to the general public, including foreign nations.

This technical report has been reviewed and is approved for publication. Publication of this report does not constitute Air Force approval of the report's findings or conclusions. It is published only for the exchange and stimulation of ideas.

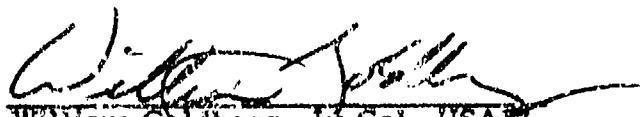


Harold A. Careway, Capt, USAF
Project Officer
Deputy for Reentry Systems



James M. McCormack, Lt Col, USAF
Chief, Reentry Technology Division
Deputy for Reentry Systems

FOR THE COMMANDER



William Goldberg, Lt Col, USAF
Director, Systems Technology
Deputy for Reentry Systems

UNCLASSIFIED

SECURITY CLASSIFICATION OF THIS PAGE (When Data Entered)

19 REPORT DOCUMENTATION PAGE		READ INSTRUCTIONS BEFORE COMPLETING FORM
1. REPORT NUMBER (18) SAMSO TR-78-99	2. GOVT ACCESSION NO.	3. RECIPIENT'S CATALOG NUMBER
4. TITLE (and Subtitle) (6) THE CHALLENGE OF REENTRY VEHICLE INSTRUMENTATION.	5. TYPE OF REPORT & PERIOD COVERED (9) Interim rept.	6. PERFORMING ORG. REPORT NUMBER (14) TR-0078(3550-74)-1
7. AUTHOR(s) (1) Phillip J./ Legendre, Wallis R./ Grabowsky, Roy G./ Fowler John M./ Cassanto	8. CONTRACT OR GRANT NUMBER(s) (15) F04701-77-C-0078	10. PROGRAM ELEMENT, PROJECT, TASK AREA & WORK UNIT NUMBERS (12) 140p
9. PERFORMING ORGANIZATION NAME AND ADDRESS The Aerospace Corporation El Segundo, Calif. 90245	11. CONTROLLING OFFICE NAME AND ADDRESS (11)	14. REPORT DATE 31 May 78
14. MONITORING AGENCY NAME & ADDRESS (if different from Controlling Office) Space and Missile Systems Organization Air Force Systems Command Los Angeles Air Force Station Los Angeles, Calif. 90009	15. SECURITY CLASS. (of this report) Unclassified	13. NUMBER OF PAGES 135
16. DISTRIBUTION STATEMENT (of this Report) Approved for public release; distribution unlimited.	15a. DECLASSIFICATION/DOWNGRADING SCHEDULE	
17. DISTRIBUTION STATEMENT (of the abstract entered in Block 20, if different from Report)		
18. SUPPLEMENTARY NOTES		
19. KEY WORDS (Continue on reverse side if necessary and identify by block number)		
Reentry Vehicles	BRAG Sensor	Off-Board Instrumentation
Instrumentation	Roll Rate Gyro	TRADEX Radar
Thermocouples	Accelerometer	ALTAIR Radar
RAT Sensor	Magnetometer	Recession Measurement
Seedants	Off-Board Radar	Shape Change Measurement
20. ABSTRACT (Continue on reverse side if necessary and identify by block number)		
<p>This tutorial presents a summary of the environments, problems, and performance of the on-board instrumentation used on the U. S. Air Force Space and Missile Systems Organization (SAMSO) flight test programs to measure reentry vehicle (RV) performance. In addition, a brief description of the off-board instrumentation will be presented. In RV instrumentation, the specific discipline performance areas covered are the thermodynamic and the aerodynamic. Within the aerodynamic discipline are the group of instruments concerned with RV dynamics (gyros, magnetometers, etc.) and</p>		

DD FORM 1473

78 17 08 103

UNCLASSIFIED

SECURITY CLASSIFICATION OF THIS PAGE (When Data Entered)

409 055

UNCLASSIFIED

SECURITY CLASSIFICATION OF THIS PAGE(When Data Entered)

19. KEY WORDS (Continued)

Temperature History
Backface Temperature
Vehicle Diagnostics
Angle-of-Attack History

20. ABSTRACT (Continued)

with RV fluid dynamic measurements (boundary layer transition and progression sensors, etc.). The thermodynamic instruments include radiation sensors, multiwire isothermal thermocouples, optical seedants, acoustic sensors, calorimeters, etc. The overriding objective of this tutorial is to provide the instrumentation supplier with a detailed feeling for SAMSO's RV instrumentation problems so that the supplier will be able to propose better instruments to solve these problems.



UNCLASSIFIED

SECURITY CLASSIFICATION OF THIS PAGE(When Data Entered)

PREFACE

The material reported in this tutorial was developed from various reentry vehicle instrumentation programs sponsored by the United States Air Force Space and Missile Systems Organization (SAMSO) during the past 15 years.

The authors wish to thank the following individuals for their assistance in preparing this presentation:

- 1) Dr. R. Hallse, Mr. R. Herold, and Ms. R. Pervorse of The Aerospace Corporation.
- 2) Mr. C. Droms, Mr. M. DiGicamo, Mr. H. Van Dusen, and Mr. R. Krieter of the General Electric Company.

Special thanks to Mr. F. Yocum and N. Satin of GE for their support of the various flight instrumentation flown to obtain the needed data.

Special thanks are also extended to Mr. R. Mortensen of The Aerospace Corporation and Capt. H. Careway, SAMSO/RSSE, who conducted the detailed reviews and critical proofreading of this tutorial. In addition, the authors would like to thank Capt. M. Elliott, Lt. Col. R. Jackson and Capt. T. Graham of the Air Force (SAMSO) who supported the special instrumentation flown and supportive analysis on the GE reentry vehicle.

ACCESSION for	
NTIS	White Section <input checked="" type="checkbox"/>
DOC	Buff Section <input type="checkbox"/>
UNANNOUNCED	<input type="checkbox"/>
JUSTIFICATION
BY	
DISTRIBUTION/AVAILABILITY CODES	
Dist.	AVAIL. and/or SPECIAL
A	

CONTENTS

PREFACE	1
1. INTRODUCTION	13
2. THERMODYNAMIC INSTRUMENTATION	17
2.1 General	17
2.2 Nosetip Specific	17
2.3 Backface Temperature Measurement	18
2.4 In-Depth Temperature Measurement	20
2.5 Breakwire Ablation Gage	20
2.6 Seedants	21
2.7 Radiation Transducer Sensor	22
2.8 Backscatter Radiation Ablation Gage	23
2.9 Light Pipe	24
2.10 Analog Resistance Ablation Detector	25
2.11 Acoustic Instrumentation	26
2.12 Heatshield Specific	27
2.13 Makewire and Breakwire Gages	28
2.14 Radioactive Tracer Technique	28
2.15 In-Depth Temperature Techniques	29
2.16 Measurement Planning	31
2.17 Analytical Procedures and Data Usage	32
3. AERODYNAMIC AND VEHICLE DYNAMIC INSTRUMENTATION	55
3.1 Purpose and Introduction	55
3.2 Flight Instrumentation Principles	56
4. AERODYNAMIC/FLIGHT MECHANIC DATA	73
4.1 Introduction	73
4.2 Drag	73
4.3 Roll Performance	74

CONTENTS (Continued)

4.4	Angle of Attack/Trims	74
4.5	C_{my} Stability Parameter and Center of Pressure.	75
4.6	Normal Force and Pitching Moment Coefficient.	76
4.7.	Axial and Lateral Loads	77
4.8	Conclusions/Flight Dynamic Instrumentation Trends.	77
5.	FLUID DYNAMIC MEASUREMENT	89
5.1	General	89
5.2	Heat Transfer Measurements	90
5.3	Steady State Pressure Measurements	91
5.4	Acoustic Measurements	91
6.	OFF-BOARD INSTRUMENTATION	111
7.	INSTRUMENTATION ASPECTS OF FUTURE REENTRY TESTING.	127
7.1	Weather Effects on Reentry Vehicle Performance	127
7.2	Communication To and From Reentry Vehicles	128
7.3	Increased Use of Ground Facilities	130
	REFERENCES.	130

TABLES

2-1.	Combinations of Seedants	22
2-2.	Isothermal-Type Thermocouple Measurement/ Correlation Accuracies	35
3-1.	Technology Parameter/Flight Instrumentation Requirements	56
6-1.	ALCOR Operating Parameters	113
6-2.	TRADEX Operating Parameters	115
6-3.	ALTAIR Operating Parameters	117
6-4.	LITE Operating Parameters	118

FIGURES

1-1.	Typical Reentry Vehicle	15
2-1.	Instrumentation Locations	37
2-2.	Backface Nosetip Thermocouple Performance	38
2-3.	Nosetip With Single Backface Thermocouple	39
2-4.	Nosetip With Multiple Backface Thermocouples	39
2-5.	Graphite Shell Nosetip Backface Temperature Instrumentation	40
2-6.	Stagnation Region Backface Temperature Response	40
2-7.	Nosetip With In-Depth Temperature Measurements	41
2-8.	Nosetip In-Depth Temperature Data	42
2-9.	Breakwire Ablation Sensor	42
2-10.	Nosetip Instrumented With Seedants	43
2-11.	Radiation Transducer Sensor Block Diagram	43
2-12.	RAT Installation	44
2-13.	Stagnation Point Recession History	45
2-14.	Recession Along 5-1/2 deg View Angle (Sonic Point)	45
2-15.	BRAG Sensor Block Diagram	46
2-16.	Nose Assembly With BRAG Sensor	46
2-17.	Nose Stagnation Point Recession - BRAG	47
2-18.	Light Pipe Ablation Sensor and Installation	47
2-19.	Light Pipe Instrumented Nosetip	48
2-20.	Light Pipe Vehicle Shape Change History	48

FIGURES (Continued)

2-21.	ARAD Sensor Design	49
2-22.	ARAD Schematic	49
2-23.	Nose Assembly With ARAD	50
2-24.	Nosetip Recession History	51
2-25.	Nosetip Acoustic Instrumentation	51
2-26.	Makewire Gage	52
2-27.	Post-Type Thermocouple Installation	52
2-28.	Isothermal-Type Thermocouple Installation	53
2-29.	Typical Measurement System	53
2-30.	Frustum Shell Thermal Instrumentation	54
2-31.	Isothermal-Type Thermocouple Temperature-Time History	54
3-1.	Typical V- γ Map	62
3-2.	Single Range-Type Displacement Accelerometer	62
3-3.	Typical Axial Accelerometer Flight Data (Displacement-Type Pot Sensor)	63
3-4.	Force Balance-Type Accelerometer Schematic	63
3-5.	Dual-Range Force Balance Accelerometer Schematic	64
3-6.	Vernier Step Accelerometer Schematic	64
3-7.	Typical Flight Data - Vernier Step Accelerometer Output	65
3-8.	Typical Analog Traces of Raw Lateral Accelerometer Flight Data	65

FIGURES (Continued)

3-9.	Typical Lateral Accelerometer Showing Trim Buildup	66
3-10.	Pitch and Yaw Rate Gyro	66
3-11.	Dual-Axis Rate Gyro	67
3-12.	Raw Flight Data for Pitch and Yaw Rate Gyro From a Typical Reentry Vehicle	68
3-13.	Raw Roll Rate Flight Data for a Typical Reentry Vehicle . . .	68
3-14.	Magnetometer	69
3-15.	Typical Raw Magnetometer Flight Data	69
3-16.	Potentiometer Pressure Sensor (Early Generation Steady State)	70
3-17.	Flight Pressure Sensor	70
3-18.	Pressure Sensor/Port Flight Experiment	71
3-19.	Capacitance Pressure Sensor	71
3-20.	Transition Indicators (Flight B)	72
3-21.	Low Range Base Pressure Data	72
4-1.	Typical Drag Component Buildup	79
4-2.	Flight Test Pressure Data	80
4-3.	Typical Flight Test Data - Measured Drag Components vs Altitude	81
4-4.	Roll Rate vs Heatshield Type and Altitude	82
4-5.	Early Buy Roll Torque Statistics	83
4-6.	Total Angle-of-Attack History	83

FIGURES (Continued)

4-7.	Petal Plot for a Typical Flight Test	84
4-8.	$C_{m\alpha}$ vs Altitude	84
4-9.	Vehicle Dynamic Schematic	85
4-10.	Nominal Angle-of-Attack History	85
4-11.	Normal Force and Pitching Moment Histories	86
4-12.	Flight Test Analysis (Angle-of-Attack Reconstruction)	86
4-13.	Typical Axial and Lateral Load Histories	87
4-14.	Magnetometer Data	87
5-1.	Rate (ΔT) Gage Installation in Heatshield	96
5-2.	Rate and Integration Calorimeter Gages Installation in Heatshield	96
5-3.	Hycal Detector Principle of Operation	97
5-4.	Calorimeter	97
5-5.	ΔT Detector Principle of Operation	98
5-6.	Internal Installation of Rate Calorimeters	98
5-7.	Thermal Transition Detectors	99
5-8.	Summary of Transition Data	99
5-9.	Transition Front Progression and Acoustic Sensor Response (Ground Test Data)	100
5-10.	Transition Sensor Locations (Flight A)	100
5-11.	Piezoelectric Acoustic Gage for Fluctuating Pressures (Early Generation).	101
5-12.	Transition Noise (Flight A)	101

FIGURES (Continued)

5-13.	Transition Onset From Acoustic Data (Flight A)	102
5-14.	Acoustic (Fluctuating Pressure) Flight Data Showing Transition Onset (Flight B)	102
5-15.	Acoustic Flight Data (Flight B)	103
5-16.	Flight Pressure Sensor	103
5-17.	Present Generation (1976) Miniaturized Integrated Pressure Transducer for Steady State and Fluctuating (Acoustic) Pressures	104
5-18.	Kulite-Ported Acoustic Gage	104
5-19.	Dual-Band Pressure Measurement System for Flight Experiment	105
5-20.	RV Flight Test Pressure Sensor Overview History	106
5-21.	Fluctuating Pressure Time Histories	106
5-22.	Flight Test Data Showing Simultaneous Measurement of Fluctuating and Steady State Pressure From Same Sensor/Port	107
5-23.	BLAM Detector Principle of Operation	107
5-24.	Transition Acoustic	108
5-25.	Internal RV	108
5-26.	Kaman (BLAM) Transducer Output	109
5-27.	Kaman Detector	109
5-28.	Nonported Acoustic Sensor	110
6-1.	KREMS Instrumentation	121
6-2.	Kwajalein Missile Range	121
6-3.	ALCOR	122

FIGURES (Continued)

6-4.	ALCOR Sensitivity	123
6-5.	TRADEX Sensitivity	123
6-6.	ALCOR/TRADEX Threshold Water Content Levels	124
6-7.	ALTAIR	125
6-8.	LITE Sensitivity to Ice Cloud	126
6-9.	High-Altitude Weather Aircraft	126
7-1.	Particle Measurement Radar	132

1. INTRODUCTION

Each Space and Missile Systems Organization flight test program has specific program objectives to be met. The flight performance evaluation of an experimental reentry vehicle (Figure 1-1) is identified as a number of detailed flight test objectives where it is required to obtain sufficient flight test data for application to future operational reentry vehicles. A typical list of detailed flight test objectives may include the following:

- a. Nosetip performance as measured by recession and shape change sensors
- b. Frustum and aft cover heatshield performance as measured by surface recession and in-depth temperature histories, steady state and acoustic pressure histories, surface heat flux histories, and boundary layer onset and progression from laminar to turbulent flow
- c. Control surface shape change and surface pressure distribution histories as measured by the same instruments used for the frustum and aft cover heatshields
- d. Vehicle internal temperatures
- e. Vehicle dynamic performance as measured by on-board instrumentation and as observed by off-board instrumentation
- f. Vehicle structural performance as measured by both on-board and off-board instrumentation.
- g. Vehicle observables, signature characteristics, and accuracy as measured by off-board instrumentation

The summary of detailed flight test objectives, the measured and derived parameters required to verify the attainment of the flight test objectives, and the instrumentation with the associated accuracies required for the direct measurements are outlined in a document for each flight called the Detailed Flight Test Plan (DFTP).

The typical RV reenters the earth's atmosphere at velocities between 18,000 and 25,000 fps (5490 and 7625 m/sec). These velocities yield the following representative severe environments encountered by the RV:

- a. P_s , Stagnation Point Pressure, 200 atm.
- b. Q_s , Stagnation Point Heating, 20,000 Btu/ft²-sec
(2.29×10^8 W/m²).
- c. H_s , Stagnation Point Enthalpy, 8000 to 12000 Btu/lb
(1.86×10^7 to 2.22×10^7 J/kg).
- d. P , Heatshield Pressure, 2 to 20 atm (about 5 to 10 percent of P_s).
- e. Q , Heatshield Heating, 500 to 2500 Btu/ft²-sec
(5.76×10^6 to 2.84×10^7 W/m²) (about 5 to 10 percent of Q_s).
- f. Surface Temperatures, 7000° R (3900° K).
- g. Vibration Amplitudes to 2.0 g²/Hz in the 20 Hz to 4 kHz frequency range and an overall level of 90 g's rms for components attached to the nosetip. The levels experienced by components attached to the heatshield are a fraction of those attached to the nosetip.
- h. Acceleration loads up to 200 g's.

A typical reentry from 300,000 ft (275 km) to impact takes from 30 to 45 sec depending on the reentry angle, shape, weight, etc., of the RV.

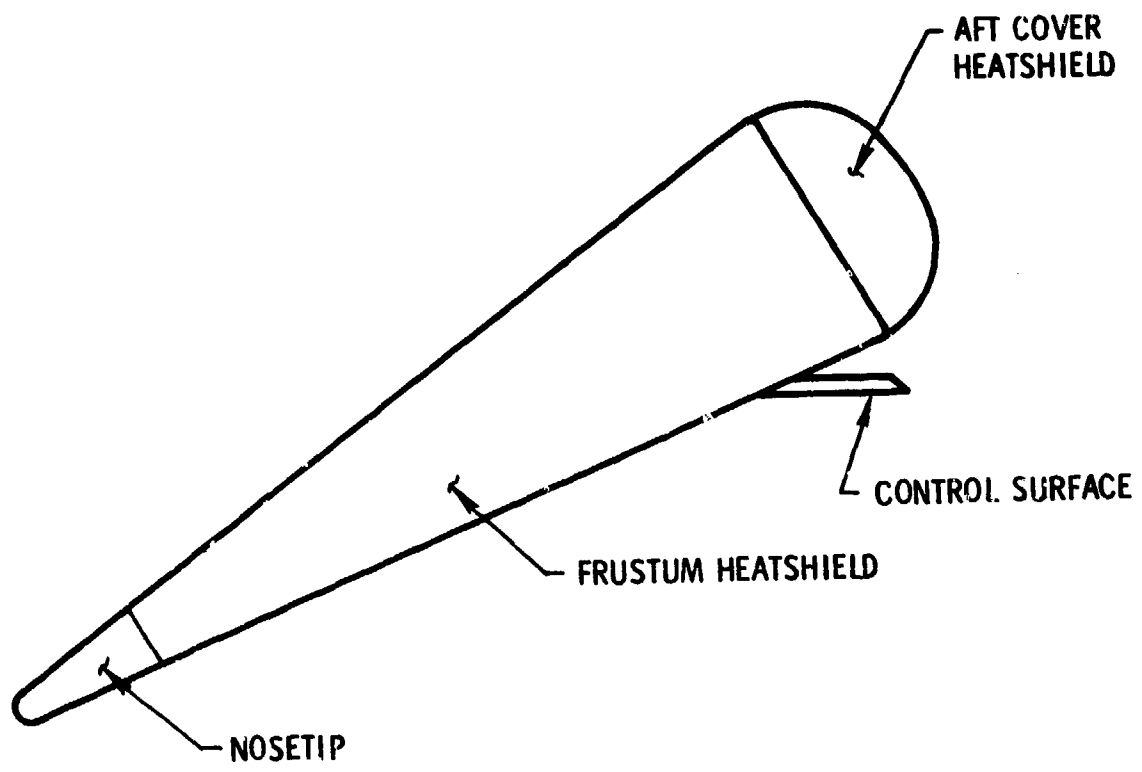


Figure 1-1. Typical Reentry Vehicle

2. THERMODYNAMIC INSTRUMENTATION

2.1 GENERAL

Thermodynamic instrumentation is concerned primarily with instrumentation of the nosetip, frustum and aft cover heatshield, internal heating, and control surfaces, if any. Generally, the types of instruments required for the nosetip are not applicable to the heatshields or control surfaces. Nosetip instrumentation usually measures through large thicknesses of material (over 30.5 cm, 1 ft, in a few extreme cases) whereas heatshield and control surface thicknesses are relatively thin (1.27 to 5.08 cm, 0.5 to 2.0 in.). The internal heating measurements are made usually with 0 to 500° F (-17 to 226° C) thermistors and have presented no problems over the past decade. The nosetip and heatshield areas that do present problems will be dealt with in this tutorial.

A typical RV thermodynamic instrumentation plan is presented in Figure 2-1, and the meaning of Figure 2-1 will develop as this section of the tutorial progresses.

2.2 NOSETIP SPECIFIC

As discussed in Reference 1, the measure of nosetip performance has progressed through a number of stages over the past 15 years. Performance was initially measured in terms of determining nosetip survival to a specified altitude. Next, the measure of performance was the nosetip recession history, and now nosetip performance is measured in terms of its shape change history. In the latter case, the nosetip recession history and survival altitude determination are byproducts of the shape change history measurements. This refinement in nosetip performance determination has resulted in the evolution of vastly improved nosetip instrumentation.

Many complex nosetip materials were developed, and each material usually required a unique instrument to measure performance although some

types of nosetips made from different materials did use similar instruments. In general, the plastic ablative nosetips, like the carbon phenolics (CP) and the quartz phenolics (QP) can be drilled and fitted with thermocouples, radioactive sources, etc., without seriously degrading the nosetip thermodynamic performance. On the other hand, the refractory nosetip, like graphitic nosetips, cannot normally be drilled without reducing their flight performance due to their sensitivity to thermal strain. The newer carbon-carbon nosetips fall in between.

Nosetip instrumentation state of the art to 1975 was reviewed in Reference 1, and some of those systems discussed then and in this tutorial are covered individually in more detail in References 2 through 12 inclusive. Also, the instrumentation installation problems associated with some of the more recently developed nosetip materials are presented in References 9, 13, 14, and 15.

2.3 BACKFACE TEMPERATURE MEASUREMENT

Reentry vehicle project engineers have traditionally been concerned with the possible degradation of nosetip performance on their reentry vehicles because of discontinuities in the nosetip material due to instrumentation installation. During the mid-1960s, the only nosetip instrumentation on some of the SAMSO Programs was one or more thermistors, resistance thermometers, or thermocouples mounted on the ballast to which the nosetip was attached. The purpose of these instruments was to measure any temperature rise in the event of nosetip failure. Usually, if the nosetip performed as predicted, these thermistors, resistance thermometers, or thermocouples would show little or no temperature rise. If, on the other hand, the nosetip was not performing as predicted, but was still functioning, the ballast-mounted instruments would usually indicate a temperature history that exceeded the predicted range and that either rose to less than the maximum range of the instrument (usually 0° to 500° F) (-17 to 226° C) or reached the maximum range of the instrument at a moderate rate of change of temperature time. In the case of

a catastrophic nosetip failure, the ballast (or forward structure) instrument would either saturate instantaneously or approach saturation at an infinite positive rate of temperature change with time at loss of signal (LOS). In short, the ballast for forward-structure-mounted thermistor or resistance thermometer was primarily a disaster detection instrument. Usually, SAMSO flight test vehicles were equipped with these instruments either as primary measurement devices or as backup instruments. In some cases, thermocouples were used in lieu of thermistors or resistance thermometers (RT), and they covered temperature ranges up to 4200° F (2600° K). A thermocouple requires a 0 to 50-mV channel, whereas the thermistor or RT requires the higher level 0 to 5-V channel.

An early SAMSO vehicle provides an excellent example of how instrumentation interpretation suffers when nosetip survivability measurement depends on only one low-level (0 to 50 mV) temperature sensor. As shown in Figure 2-2, flight data indicated a negative reading (a temperature below 32° F) of approximately -30 percent full scale (for the nose thermocouple). It should have read +10 percent of full scale. This level fluctuated between -30 and -40 percent full scale until approximately 373.3 sec. At that time, there was an apparent rise, which continued to about +25 percent (565° C) at 379.3 sec when the data points became scattered. From visual data, this graphite nosetip vehicle (see Figure 2-3) was observed to have demised. Unfortunately, the one malfunctioning temperature measurement did little to pinpoint the time of nosetip demise. In short, multiple sensors are required.

An example of an early nosetip with multiple nosetip backface temperature instrumentation is shown in Figure 2-4. Eight backface thermocouples are shown between the nosetip shell and the ballast.

Thermocouples have been used to obtain the nosetip backface temperatures in special applications to graphite nosetips. Because of the thermal structural weaknesses of graphite, it is inadvisable to drill holes in high performance graphite shell nosetips to install thermocouples and other allied

instrumentation. Therefore, to get some measure of the graphite shell nosetip performance, thermocouples were pressed against the interior wall of the graphite shell. On a past SAMSO Program, the backface thermocouples were spring-loaded against the nosetip shell backface (see Figure 2-5). The flight test temperature data for this nosetip are superimposed on the analytical data in Figure 2-6. In this situation, the assumption was made that, if the flight test backface temperature data matched the predicted data, then the predicted nosetip recession and shape change histories were also grossly correct. As shown in Figure 2-6, the nosetip flight and predicted temperature data agreed quite well.

2.4 IN-DEPTH TEMPERATURE MEASUREMENT

Some measure of nosetip thermodynamic performance was obtained by locating thermocouples in the nosetip material. These were bayonet type (also called post thermocouples) mounted in holes drilled parallel to the nosetip centerline from the rear of the nosetip.

Figure 2-7 depicts a nosetip equipped with an array of 12 backface thermocouples similar to those shown in Figure 2-4. However, in the Figure 2-7 nosetip, two in-depth, bayonet-type thermocouples (A147 and A148) are located at two depths in the secondary nosetip material. In this specific case, no temperature rise was predicted by any of the 14 sensors and none was indicated by the flight test data. As shown in Figure 2-8 (a nosetip similar to that shown in Figure 2-7), one of the thermocouples did rise significantly. This permitted the nosetip designer to compare the measured and predicted results and redesign accordingly.

2.5 BREAKWIRE ABLATION GAGE

As discussed in Reference 16, the breakwire ablation gage is usually associated with the frustum heatshield (Figure 2-9). It has not been very successful in this application. Theoretically, as the heatshield surface receded and/or charred, the increasing heat entering the heatshield was supposed to progressively melt the breakwires and break the electrical

circuit. However, on some Refrasil heatshields, the receding char layer made excellent electrical contact between the melted wires and gave the erroneous readings that the surface had not yet charred to a given depth. This same principle was applied to a nosetip similar to that depicted in Figure 2-7 except that breakwires, in lieu of in-depth, bayonet-type thermocouples, were installed to detect secondary nosetip recession. However, none of the breakwire thermocouples responded. This normally would indicate that the nosetip had not receded to the position of the first breakwire, but this was not consistent with similar flights.

Both breakwire and makewire ablation gages were ground tested in nosetips on the Carbon-Carbon Nosetip Development Program (CCND).⁽¹⁷⁾ The ground tests indicated that both concepts functioned satisfactorily with respect to measuring nosetip recession, but, unfortunately, the size of the sensors degraded the carbon-carbon nosetip recession performance too much to consider them for flight applications.

2.6 SEEDANTS

Many of the previously discussed nosetips, which were instrumented with one or more forms of thermocouples, were also instrumented with optical seedants. A seedant for RVs is a material that would be highly observable by optical ground instrumentation when vaporized by the severe thermal environment to which it was subjected. Some of the seedants used are tabulated in Table 2-1. A typical seedant instrumentation scheme is shown in Figure 2-10. No trace of the indium sulfide or ytterbium carbonate was noted during flight. None of the seedants was observed on a second vehicle that demised due to nosetip failure, but the cesium in the cesium iodide crystal of a scintillator package was observed. Similar lack of success was observed in other flights on the same SAMSO program. Therefore, it was concluded that seedants did not really work and consequently were not included in the instrumentation of succeeding RV programs.

Table 2-1. Combinations of Seedants

EC 2216/indium sulfide and ytterbium carbonate
Araldite 502 - europium chloride chromium powder
Barium chloride and indium sulphide
Molybdenum coat on ballast
Zirconium oxide/molybdenum on ballast with barium chloride and indium sulphite in the bonding material
Silver indium

2.7 RADIATION TRANSDUCER SENSOR

The radiation transducer (RAT) sensor (also known as RAD sensor) has been one of the best nosetip sensors used to date for measuring stagnation point recession and nosetip shape change history for plastic nosetips (i. e., carbon phenolic, quartz phenolic, etc.). Essentially, this technique employs small radioactive particles of material deployed at known depths in the nosetip. As each source is sequentially removed in the ablation process, the reduction in radiation intensity is detected by a miniature Geiger counter mounted within the vehicle to give the precise location of the receding surface. A schematic of the RAT sensor is presented in Figure 2-11.

The RAT sensors used on a number of SAMSO programs utilized Geiger-Mueller tube detectors and Tantalum 182-carbide (TaC) sources. A typical RAT sensor pellet installation is shown in Figure 2-12. The reduced flight test data from this installation are shown in Figures 2-13 and 2-14. In the case of Figure 2-13, the first two sources along the ray of sensor SR-1 (see Figure 2-12) have been removed, but the source 6.35 cm aft of the tip has not. Similarly, in Figure 2-14, sources A and B have been removed (see Figure 2-12), but source C has not.

A second form of the RAT sensor utilizes a scintillation counter instead of a Geiger-Mueller tube for a detector. Very little (or questionable) success was obtained with this variation of the RAT sensor in the late 1960's, but in the early 1970's this variation worked very well.

In the mid-1970's, counters based on a cadmium telluride (CdTe) crystal were developed by several RV contractors. ^(18, 19) These CdTe detectors were more efficient than previous detectors thus permitting lower nosetip radiation levels per line permitting lower nosetip radiation levels per line source for a given accuracy. Also, these detectors were smaller than the Geiger-Mueller tubes, for example, and this permitted a larger number of line sources to be installed per nosetip.

References 3, 7, 8, 9, 10 and 11 cover almost every type and phase of RAT sensor development in detail.

A variation of the RAT sensor, called the shape change ablation transducer (SCAT), was flown in the early 1970's, but it was not very successful. ⁽¹⁾ Whereas the RAT sensor radiation sources were embedded wires in the plastic of nosetips, the SCAT sensor utilized tantalum 182 diffused in a graphite nosetip during the manufacturing process. Essentially, the SCAT sensor consisted of the irradiated graphite nose cap, three scintillator-photomultiplier tube gamma-ray detectors, and an electronics package to convert the measured gamma radiation to an electrical signal. Unfortunately, the diffused tantalum 182 source swamped out the signal because of (a) inadequate sidewall shielding of the detectors or (b) redeposition of the tantalum 182 on the heatshield adjacent to the detectors.

In recent years, continuous line sources ^(3, 9, 11) have been developed to replace the pellet sources to overcome performance anomalies. ⁽¹³⁻¹⁵⁾ These anomalies were caused by aggravated recession at the sites of the pellet sources due to the presence of the sources. The amount and severity of the aggravated recession was a function of source size, installation expedient, tolerances, adhesive and the post installation cure of the adhesive. A line source integrated into the structure of the nosetip eliminated all of the above problems.

2.8 BACKSCATTER RADIATION ABLATION GAGE

The backscatter radiation ablation gage (BRAG) sensor was initially proposed by the Gianni Controls Corporation under a General Electric Company (GE) development contract in the early 1960's. ^(16, 20, 21) In recent years, this instrument was developed by GE and flown on many SAMSO vehicles.

The BRAG sensor consists of a source of gamma radiation, a shield for preventing direct transmission to the gamma-ray detector unit, the detector unit itself, and the signal conditioning electronics (see Figure 2-15).

A portion of the gamma radiation from the source is backscattered from the ablation material, and a fraction of these backscattered rays reaches the detector unit. This fraction is directly proportional to the thickness of the ablation material at the specific time during which the measurement is performed. The detector unit digital sensor converts the gamma rays into electrical pulses that are simply scaled for the telemetry (TM) bandwidth and transmitted directly over the TM link. Figure 2-16 shows the installation of the source, collimation hole, and detector in a nosetip. The nose stagnation point recession is shown in Figure 2-17.

The primary advantage of the BRAG sensor is that it does not require the placement of discontinuities (drilled holes, pellets, etc.) in the nosetip material as does the RAT sensor concept, for example. This makes the BRAG sensor an excellent instrument for graphitic nosetips that do not tolerate large discontinuities.

A more detailed account of the GE BRAG sensor and its application may be obtained from Reference 22.

Sometimes it is desirable to measure the recession of the ballast material (usually tungsten) under the primary nosetip when this material is exposed prior to impact. The gamma-ray source of the previously discussed BRAG sensor will not work due to the gamma-ray attenuation qualities of tungsten. A BRAG sensor based on a neutron source was developed, but never flown, to cope with this application.⁽¹⁴⁾

2.9 LIGHT PIPE

NASA Langley Field developed an ablation gage in the early 1960's in which the surface recession was measured by the change of light intensity.⁽¹⁶⁾ The NASA Langley instrument is placed in a blind hole. When the hole is uncovered during the ablative process, the light from the incandescent ablative surface is transferred via a sapphire light pipe to a photodiode. The electrical current produced by the photodiode is transmitted via telemetry to the ground.

The light pipe was developed further by the Avco Corporation in the early 1970's for application to three-dimensional quartz phenolic (3-DQP) nosetips. It was believed that a high number of light pipe sensors installed in a nosetip would give sufficient data to enable the postflight analyst to reconstruct the nosetip shape change history of the flight test nosetip.

The Avco light pipe utilizes quartz fibers to transmit the light to the photodiode. An Avco light pipe assembly for use in a ground test is shown in Figure 2-18. In this assembly, bundles of seven 0.008-in. diameter (0.0203 cm) quartz fibers are used to transmit the light. The surfaces of the fibers are covered with chromium. The overall width of the assembly is 0.040 in. (0.103 cm); the seven light pipe assembly was developed for use on SAMSO RVs. A typical three light pipe installation in a ground test nose-tip is also shown in Figure 2-18.

The light pipe sensor was flown on a SAMSO vehicle in early 1973. The 3-DQP nosetip was instrumented with 13 light pipe sensor bundles with 7 steps per bundle. The light pipe sensor installation is outlined in Figure 2-19. Also note the other types of complementary instrumentation previously discussed in this paper. The flight test was very successful with respect to the light pipe sensor performance where data from all 91 (7×13) data points were obtained.

The reduced nosetip shape change history is presented in Figure 2-20 for the 0 deg meridian plan. Note that the 91 data points permit a more definitive nosetip shape change history than the 25 RAT data points for the vehicle presented in Figure 2-12.

2.10 ANALOG RESISTANCE ABLATION DETECTOR

The analog resistance ablation detector (ARAD) was developed by GE to determine the shape change history of ablative nosetips by determining the nosetip recession via an analog voltage proportional to the recession.

The ARAD sensor element (shown in Figure 2-21) is a three-terminal device consisting of a helix of platinum tungsten resistance wire wound over a quartz fiber-covered central platinum/conductive epoxy electrode. Quartz fiber is also used to insulate the helix from the outer conductive shell that is composed of platinum wires and conductive epoxy. The entire sensor is only 0.05 in. (0.102 cm) in diameter and can be wound to any desired length.

The nominal impedance of the helical portion of the sensor is 7000 Ω /in. (2760 Ω /cm). As the surface of the nose recedes during ablation, the resistive element is burned off with the resultant change in resistance giving a continuous measurement of the heatshield thickness. For preablation testing, the end of the sensor is coated with conductive epoxy that shorts the inner and outer conductors to the end of the helix.

During ablation, the hot quartz serves as a movable short, completing the sensor circuit. A schematic of this circuit is shown in Figure 2-22.

A nosetip and ARAD installation are presented in Figure 2-23. There were 13 ARAD sensor installations in this nosetip.

An example of ARAD data is shown in Figure 2-24 in the form of a nosetip surface recession history.

2-11 ACOUSTIC INSTRUMENTATION

Although radiation-type sensors have been performing admirably on SAMSO vehicles for over 15 years, there is a trend to use nonradiation sensors whenever possible because of the radiation handling problems. In the case of nosetip instrumentation, acoustic measurement devices have been developed and are being improved to obtain nosetip recession and shape change. (2, 5, 6)

In these applications, a transmitter at the backface of the nosetip sends a pulse through the nosetip, the pulse is reflected from the nosetip surface, and the reflected wave is picked up by a receiver mounted on the nosetip backface (Figure 2-25). The differences and lags between the transmitted and received wave forms will vary as the nosetip recedes, and it is these differences that enable the analyst to determine the resulting nosetip recession.

In addition to measuring nosetip recession, recent flight test results indicate that this sensor may sense boundary layer transition on the nosetip and encounters with weather phenomena.

2.12 HEATSHIELD SPECIFIC

The performance evaluation of the heatshield is identified as a detailed flight test objective where it is required to obtain sufficient flight test data for the design of future operational heatshields with a small margin of safety (MS). Performance is usually defined as the heatshield's time histories (surface recession and temperature). A small MS means lighter heatshields and greater operational range. Heatshields that ablate predictably and consistently indicate that the vehicle dynamic parameters (like the center of gravity offset and vehicle moment changes due to ablation-caused mass distribution changes), which are dependent upon the heatshield recession, shape change, surface roughness, etc., will be predictable and consistent. Unpredictable and inconsistent vehicle dynamics mean unpredictable, inconsistent, and usually unacceptable vehicle targeting accuracies.

Control surface shape change data, which may influence body and control surface aerodynamic designs, are valuable to the design of maneuvering vehicles and their control requirements. In-flight determination of heatshield performance on reentry vehicles has long presented a difficult measurement problem. The difficulties encountered in the measurements are a result of the previously discussed environment, which includes high heat flux, oxidation, and aerodynamic shear conditions. Included with these difficulties are the electrostatic and electrodynamic problems associated with the plasma, as well as the telemetry system RF power reflected from the plasma at the time of highest measurement interest. The response of the heatshield to the reentry environment can include surface recession, cracking, swelling, outgassing, and other physical and chemical processes that present severe heatshield instrument installation design problems.

Heatshield instrumentation state of the art to 1973 was reviewed in Reference 23. Some of the heatshield instruments developed since will be discussed briefly in this tutorial and in detail in References 24 to 26, inclusive.

2.13 MAKEWIRE AND BREAKWIRE GAGES

As discussed earlier in this tutorial and in Reference 16, many measurement techniques have been considered for measuring the surface recession of a reentry vehicle heatshield. For example, makewire (Figure 2-26) and breakwire gages (Figure 2-9) were considered in the early 1960's. In the case of the makewire gage, a continuous coil of wire was embedded in the heatshield material and a common wire was located in the center of the heatshield material within the confines of the coil. As the ablated char layer increased in thickness, electrical continuity was progressively established between the wire coils and the common wire because of the conductivity of the carbon content of the char layer. Unfortunately, all that had been directly measured was the progression of the charring process to the point that a current could be conducted between the coil and common ground. It was not a direct indication of surface recession.

In the case of the breakwire ablation gage, wires were installed in a plug of heatshield material, and a current normally flowed through the wires. As the surface receded and was charred, the increase of heat flowing into the heatshield progressively melted the wires and broke the electrical circuit to indicate heatshield degradation to a specific depth. Unfortunately, the char layer in some instances made an electrical contact between the melted wires and gave erroneous readings of char layer formation or surface recession.

2.14 RADIOACTIVE TRACER TECHNIQUE

This technique employs several small radioactive particles of material deployed at known depths in the heatshield material in a manner similar to that for nosetips (Figure 2-11). As each source is sequentially removed in the ablation process, the reduction in radiation intensity is detected by a sensing element, such as a miniature Geiger counter mounted within the vehicle, to give the precise location of the receding surface.

Difficulties in data interpretation are encountered using this concept due to the statistical nature of the radiation impingement on the Geiger counter. The "steps" produced by the removal of discrete sources overcome, to a large extent, the statistics problem if the flight is on schedule. Delays in flight dates cause increased system errors due to decay of the radioactive material, with attendant degradation of the counting statistics. Of course, some of these difficulties may be minimized by increasing the source strength and the sampling rate.

2.15 IN-DEPTH TEMPERATURE TECHNIQUES

Thermocouples mounted at predetermined depths below the heatshield surface provide temperature histories at the respective locations, from which the position of the ablating surface may be deduced. The accuracy of this system is enhanced in a high heating rate environment, where the rate of temperature change near the surface is very high. The thermocouples normally used are the tungsten-rhenium type, 3 to 5 mils in diameter, which have good calibration to 4200° F (2600° K) and may produce acceptable readings as high as 5000° F (3050° K). The chromel-alumel wire is sometimes used for applications to 2200° F (1480° K). The use of this sensor as a recession gage does not depend to a great extent on the accuracy of the temperature measurement; however, it depends on the accuracy of the extrapolation of a temperature-time plot to the temperature at which it is estimated that the heatshield material has reached its demise. At a high rate of temperature change, the slope is almost vertical and the time resolution of the sensor is inconsequentially small.

Measurements of heatshield material temperature have been made with two basic thermocouple configurations: the isothermal installation and the bayonet- or post-type installation.

The post or bayonet configuration can be simply installed as shown in Figure 2-27. Holes are drilled in the vehicle heatshield material from the inside and the thermocouple is bonded in place. The drilling of a specific depth below the surface of the heatshield is difficult, and depth locations with

uncertainties of as much as 0.020 to 0.030 in. are normal because of the awkward drill handling and dimensional measurement requirements involved in drilling the holes from the inside.

An isothermal configuration is shown in Figure 2-28. The purpose of this design is to eliminate or minimize the error inherent in the post type caused by heat conduction down the lead wires from the hot junction. The magnitude of this error is a function of the differences in conductivity between the heatshield material and the thermocouple material and can be as high as 50 percent. ⁽²⁹⁾ Several isothermal plugs have been developed without the outer sleeve depicted in Figure 2-28, and these were also flight-tested successfully on SAMSO vehicles.

After a plug has been fabricated, the plug is X-rayed to determine the location of the junctions below the surface of the plug. Using this method, the location errors can be held to less than 0.001 in. (0.00254 cm) for the cold heatshield.

In-flight measurement accuracy involves the accuracies of the series elements in the data acquisition system. For the typical measurement system shown in Figure 2-29 involving an isothermal-type thermocouple, the uncertainties are as follows:

Hot junction	< 1 percent
Reference junction	< 0.005 percent
<u>TLM system</u>	<u>< 0.2 percent</u>
Root sum square (RSS) of above errors =	< 1.1 percent

Uncertainties due to thermocouple lead wire conductivity, thermal mass, junction, lead wire shielding, insulation degradation, and contact of the thermocouple hot junction with the heatshield material can only be assessed by ground tests using the particular heatshield at a heating rate that closely approximates the rate expected for the particular trajectory.

2. 16 MEASUREMENT PLANNING

In order to determine the frustum heatshield thermodynamic performance, there are a number of general quantitative requirements that must be met to obtain the required flight test data.

The primary instrument used to measure and assess the thermodynamic performance is the four-wire, isothermal-type thermocouple plug. The distribution of these plugs in the heatshield is the key to good heatshield performance assessment. Generally, these plugs are placed at two or three body stations, depending on the length, in order to measure the heatshield's axial performance. The body station is the term used to define the axial distance aft of the nosetip stagnation point. Based on past experience, a rule of thumb for the number of body stations is one body station for every two feet of frustum heatshield length. In the case of a three-body-station instrumentation map, the body stations selected are usually located slightly aft of the nosetip frustum heatshield interface, at midfrustum, and on the aft frustum, just forward of the base. A typical installation is shown in Figure 2-30.

At each body station, the isothermal plugs will be located at three or four meridians 90° or 120° apart. With the high reliability attained with most frustum heatshield thermocouples during the past five years, three meridians per body station are usually adequate to obtain and assess the radial asymmetry in the frustum heatshield thermodynamic performance. The meridians selected at each body station should be the same for all body stations as is shown in Figure 2-30, for example, in order to track the progression of boundary layer transition from laminar to turbulent flow. At each point, which has now been defined by a meridian and a body station, there is usually one isothermal plug with four in-depth positions. Sometimes a resistance thermometer will be co-located as near as possible with each in-depth thermocouple (IDT) plug for vehicles flying heatshields with very small design margins.

On those programs where radiation detector (RAD) sensors were used to obtain surface recession, the philosophy of sensor placement was similar to that of the IDT placement. Originally, the RAD sensor was believed to be the primary instrument to obtain the surface recession. As discussed later in this paper, this belief has changed. Each RAD sensor location usually had a minimum of four radioactive pellets. Of course, the more RAD sensors and their associated radioactive pellets, the higher the overall activity of the vehicle and the attendant handling, licensing, and documentation problems. However, only one telemetry channel is required per RAD sensor, so four surface-recession data points may be obtained per channel as compared to one per channel with the four-wire thermocouple plugs.

2.17 ANALYTICAL PROCEDURES AND DATA USAGE

The frustum heatshield thermodynamic performance for the given flight environment is determined from temperature-time history, surface recession, and boundary layer transition, detection, and propagation data. Computer programs, like those in Reference 30, have been evolved during the past 15 years to utilize these data to compute the integrated frustum heating, the heatshield ablation product's mass flow rates and their associated integrated totals, and, finally, the actual as flown heatshield MS. The MS is defined as follows:

$$MS = \frac{x_d - x_r}{x_r} \times 100 \text{ percent}$$

where

x_r = heatshield thickness predicted to hold the backface to a specific temperature at impact

x_d = actual designed heatshield thickness

In general, the more predictable a heatshield material's performance the lower the MS required. The specified MS for the SAMSO vehicles varies between 25 and 50 percent, depending on the confidence in the known data of the specific material prior to flight.

The thermodynamic performance of a frustum heatshield is evaluated from a thermodynamic simulation of the heatshield. Several key inputs are required for this simulation:

- a. The actual trajectory flown by the reentry vehicle
- b. The thermodynamic and thermochemical properties of the heatshield material
- c. The onset, propagation, and nature of the laminar to turbulent flow transition of the boundary layer

The flight trajectory is reconstructed from flight data, and the heatshield material properties are usually known prior to flight, although the flight test data are occasionally used to determine some of these material properties. It is necessary to know the location of the onset and progression of transition (both axially and azimuthally over the vehicle) and the nature of the transition in order to properly program the postflight simulation. For example, if transition occurs instantaneously at a point on the heatshield the aerodynamic heating calculated up to that time will be a laminar heating calculation, and the aerodynamic heating calculated after that time will be a turbulent heating calculation. If, on the other hand, the transition is not instantaneous, a laminar to turbulent transition relationship will be used to calculate the aerodynamic heating. It is imperative that the aerodynamic heating be simulated correctly because the accuracy of the entire postflight analysis depends on that of the aerodynamic heating. Finally, when the post-flight temperature-time and surface-recession-time histories are calculated, they are compared to those measured in flight to assess the performance of the heatshield and to aid in the diagnosis of flight anomalies.

The isothermal-type thermocouple was used extensively on SAMSO flight test programs to measure the onset of boundary layer transition, heatshield temperature-time histories, and heatshield surface recession. The estimated measurement accuracies attained by the isothermal-type thermocouple are tabulated in Table 2-2 for representative vehicles from those programs.

In Table 2-2, the correlation of surface recession as predicted by postflight analysis to that measured in flight is expressed in terms of percent for vehicle D. These data show, for example, that the predicted and measured surface recession data compare to within -3.5 to +7 percent of total recession of each other, where the flight test data were derived from the temperature-time history data measured at station 39. At station 92.5, these flight and predicted data correlated from 0 to -8 percent in total recession, depending on the meridian. Back at stations 95.5 and 98.5, the correlation comparison falls off to -10 percent of the total recession. Therefore, for vehicles equipped with the proper isothermal-type thermocouple plugs, the surface recession can be deduced from the temperature-time history to within 10 percent of the total recession, and these results were comparable to those obtained by the RAD sensor installed at the same stations.

The correlation of the temperature-time histories, as predicted by postflight analysis, to that measured in flight is presented in Table 2-2 in terms of the difference between the two temperature-time histories in degrees Fahrenheit and percentage error over the altitudes defined. The latter is referenced to the predicted temperature-time history. For Vehicle A, Table 2-2 shows that the flight test data correlated precisely with the predicted values for most of the trajectory. There were a few of the sensors (130 mils or deeper into the heatshield) that deviated from -5 to +2.8 percent from the predicted values. All of the 10-mil near surface thermocouples

Table 2-2. Isothermal-Type Thermocouple Measurement/Correlation Accuracies (23)

Measurement Vehicle	Body Station	Meridian (deg)	Depth (in.)	Boundary Layer Transition Error (ft)	Temperature - Time History		Surface Recession % Error	Altitude of Error Estimate (ft)	References				
					Error °F	% Error							
A	47.82	30	0.010	±2	-500	-25	N/A	73	(17)				
	68.03	All	0.100	±1	-150	-25		196					
	92.5		±1.5	-400	-22.2	73							
	47.82		0	0	0	300 to Impact							
	68.03		0.130	0	0	300 to Impact							
			0.180	+25	+2.8	73 to Impact							
	92.50		0.100	0	0	300 to 73							
			0.130	-50	-5	10							
	92.50		0.130	0	0	300 to 56							
			0.180	-50	-5	10							
	92.50		0.180	0	0	300 to Impact							
			0.100	0	0	300 to 25							
92.50	0.130		0	0	300 to Impact								
	0.180	+25	+2.8	100 to Impact									
B	47.7	All	0.010	±1	-500	-25	N/A	300 to 35	(18)				
	68.83	150	0.100	N/A	0	0		300 to 42					
	92.5		0.100	+125	+16	22							
	47.7		0.180	0	0	300 to 42							
	68.83		All	0.180	+50	+20		42 to Impact					
			30, 270	0.100	0	0		300 to Impact					
	92.5		All	0.180	+35	+20		42 to Impact					
			30	0.100	0	0		300 to 10					
	92.5		150, 270	0.130	+35	+8.5		300 to 10					
			All	0.180	+35	+20		100 to Impact					
	C		170.3	All	0.008	±2.5		-250		-25	N/A	300 to 85	(4)
			134.4	All	0.100	N/A		0		0		85 to 60	
0.300					-100	-10	300 to 100						
134.4		0	0		75								
87		-100	-10		300 to 80								
All		0	0		Almost to Impact								
	0	0											
D	39	180, 352	0.010	±1	-250	-16.7	N/A	165 to 105	(6)				
	92.5	180, 352	0.010	N/A	0 to -350	0 to -8		195 to 75					
		All	0.080	0 to -50	0 to -5.5	165 to 85							
	92.5	All	0.080	0 to ±300	0 to ±10	85 to 40							
			0.140	0 to -50	0 to -5.5	200 to 45							
	0.21		0 to +50	0 to +5.5	200 to 20								
	0.010		-175	-10	175 to 125								
	0.010		±125	+7	125 to 110								
	0.100		0	0	200 to 50								
	92.5	225	0.180	0	0	200 to 45							
			0.010	-200	-16	165 to 110							
	95.5	All	0.010	0	0	105 to 87							
			0.100	0	0	200 to 75							
	0.020		-100	-18	75 to 50								
	0.180		0	0	50								
	98.5		All	0.300	0	0		200 to 50					
				0.020	-200	-20 to -15		300 to 20					
	0.100	0		0	200 to 100								
0.180	0	0		100									
98.5	0.100	0		0	200 to 75								
	0.300	0 to +20		=0	200 to 50								
		0.300	0 to +20	=0	200 to 20								

however, were up to 25 percent lower than predicted. Most of the Vehicle B flight test data were similar to the Vehicle A data in that:

- a. Near surface thermocouple sensors were 25 percent lower than predicted
- b. Most of the in-depth thermocouples (100 to 180 mils) correlated precisely with the predicted for low altitude
- c. Some of the 130- and 180-mil sensors deviated from the predicted values

Some of the deviations were as high as 20 percent. The correlation of Vehicles C and D data followed the same pattern of accuracies as those on Vehicles A and B. The one disturbing aspect common to all four vehicles was the 25 percent low flight test measurement (relative to the predicted) exhibited by the near surface thermocouples prior to boundary layer transition. There have been a number of discussions within the SAMSO community about this and the reasons include:

- a. The high altitude laminar heating prediction is incorrect.
- b. The 5-mil thermocouple wires plus insulation represent a significant heat sink when covered only by 10 mils of heatshield.

If the first reason were true, then none of the deeper thermocouples should have correlated. A detailed continuance of this accuracy study is presented in Reference 31.

In summary, the Table 2-2 data indicate that the isothermal-type thermocouple does yield a delivered accuracy better than ± 5 percent of actual value for most sensors over most of the trajectory. An example of a correlation between the flight test and the calculated temperature-time histories for a vehicle utilizing the isothermal-type thermocouple is presented in Figure 2-31. This correlation is nearly perfect during most of the reentry time for the isothermal-type thermocouples located at 0.080, 0.140, and 0.210 in. below the heatshield surface.

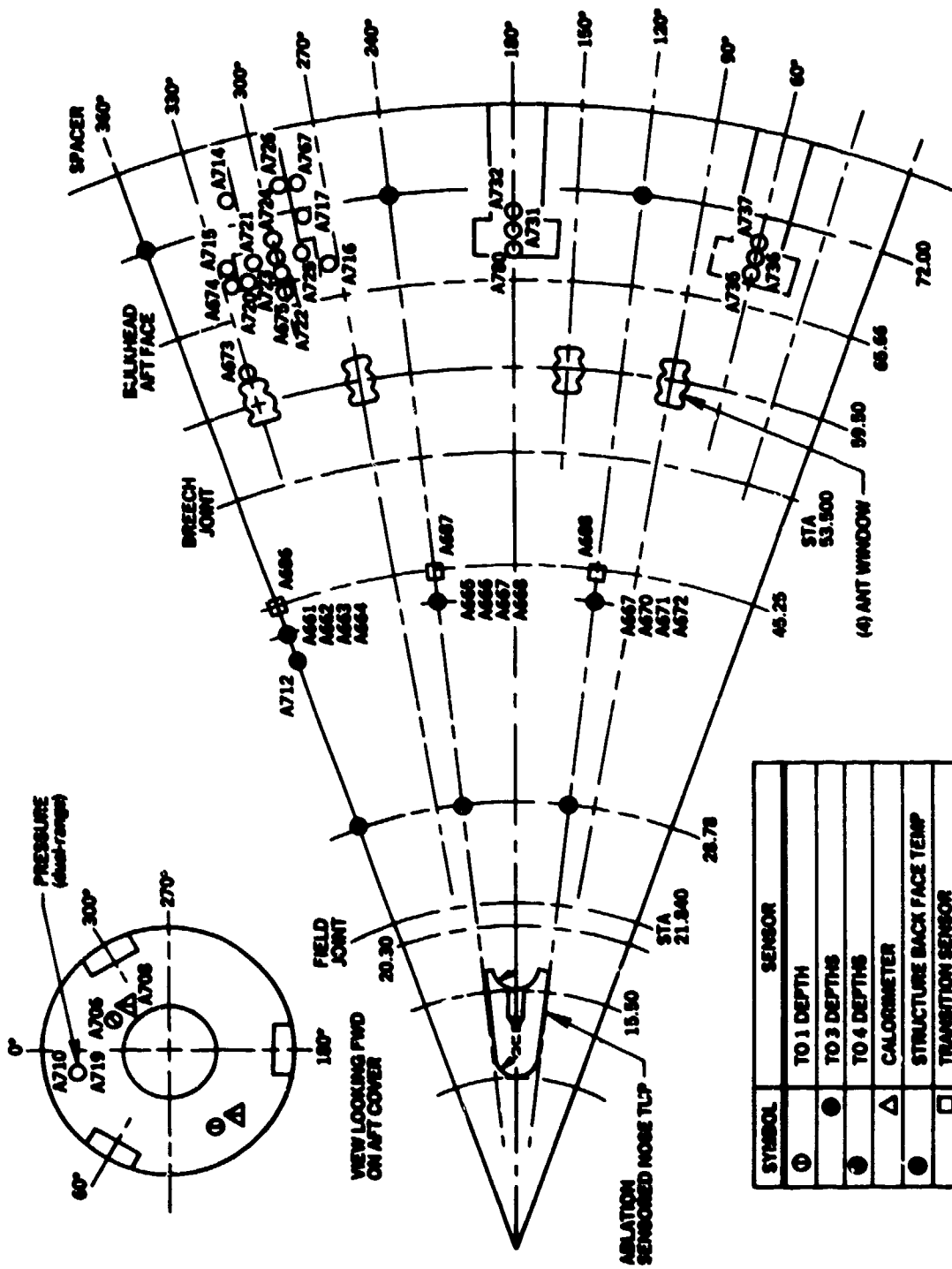


Figure 2-1. Instrumentation Locations

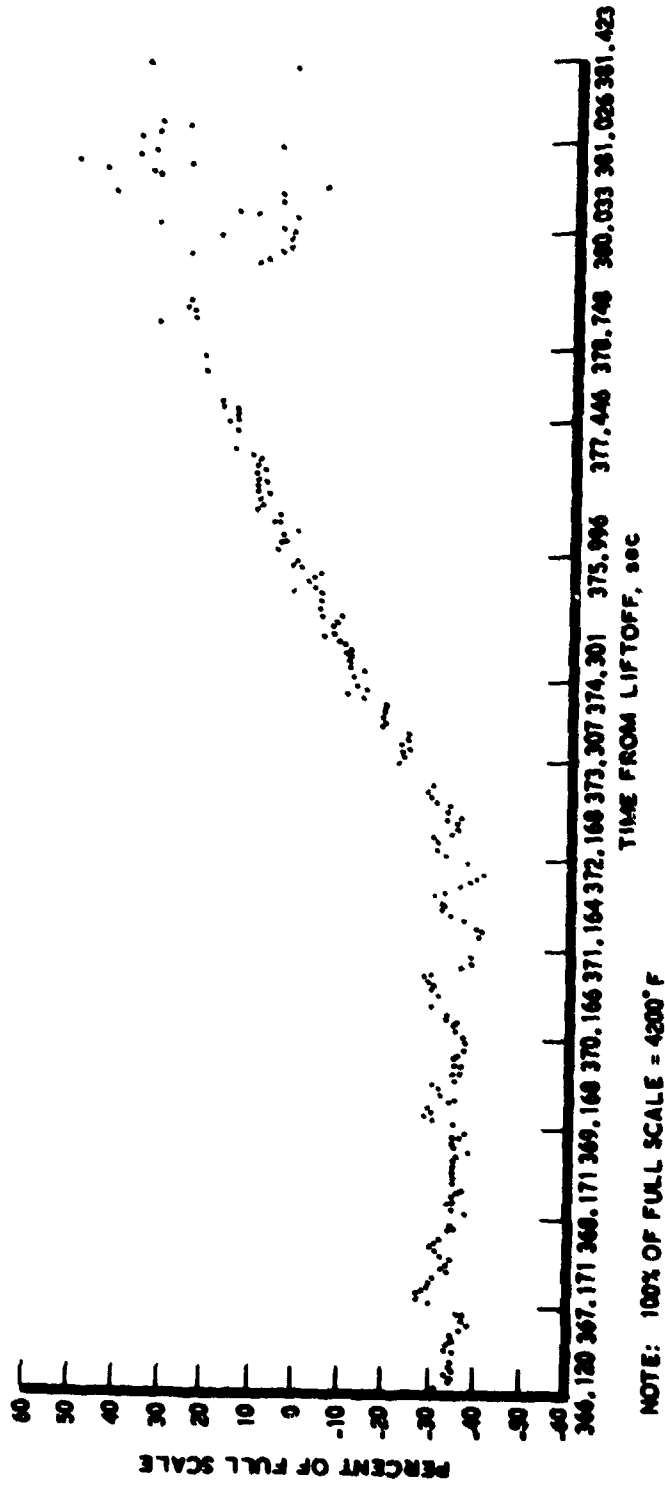


Figure 2-2. Backface Nasetip Thermocouple Performance

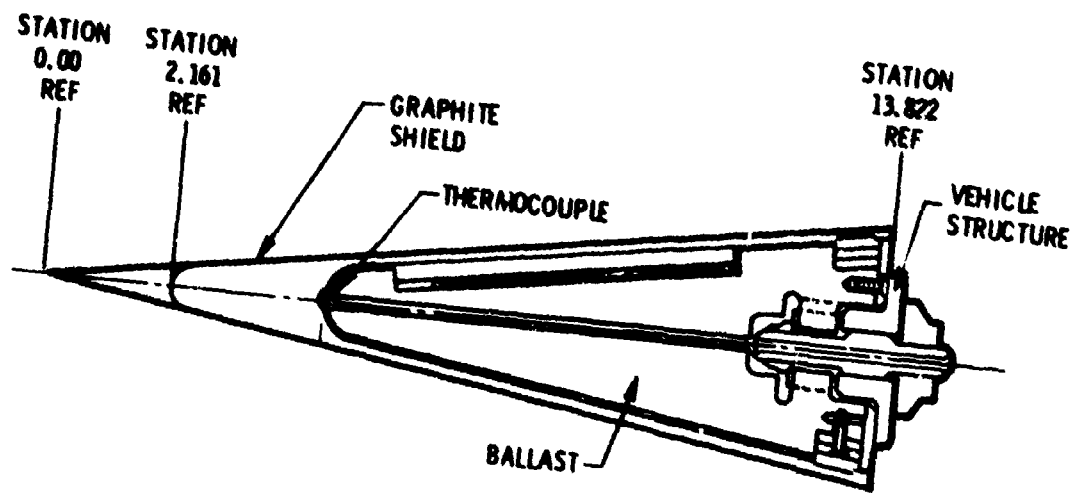


Figure 2-3. Nosetip With Single Backface Thermocouple

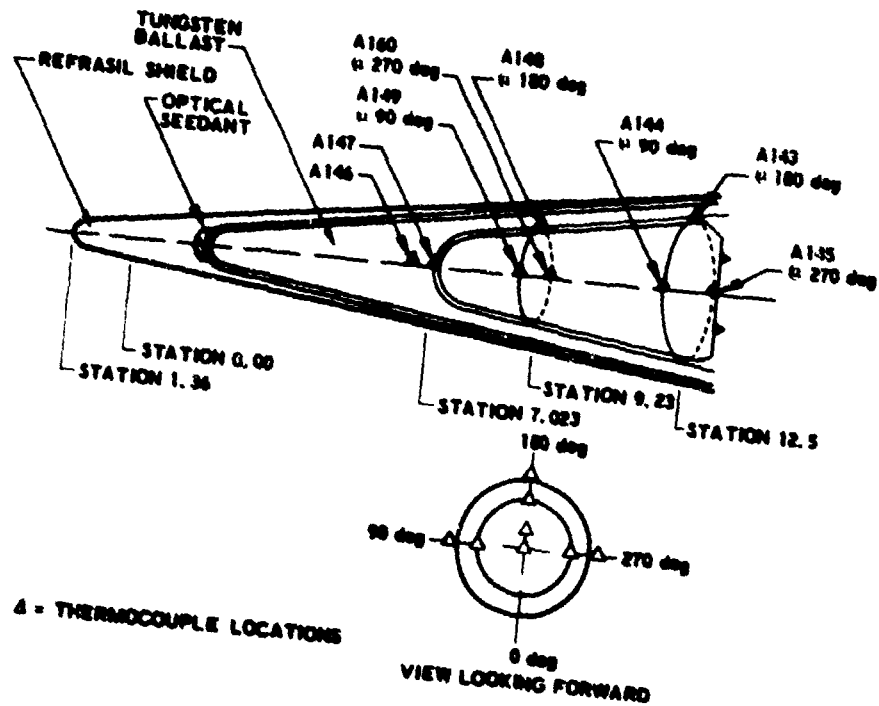


Figure 2-4. Nosetip With Multiple Backface Thermocouples

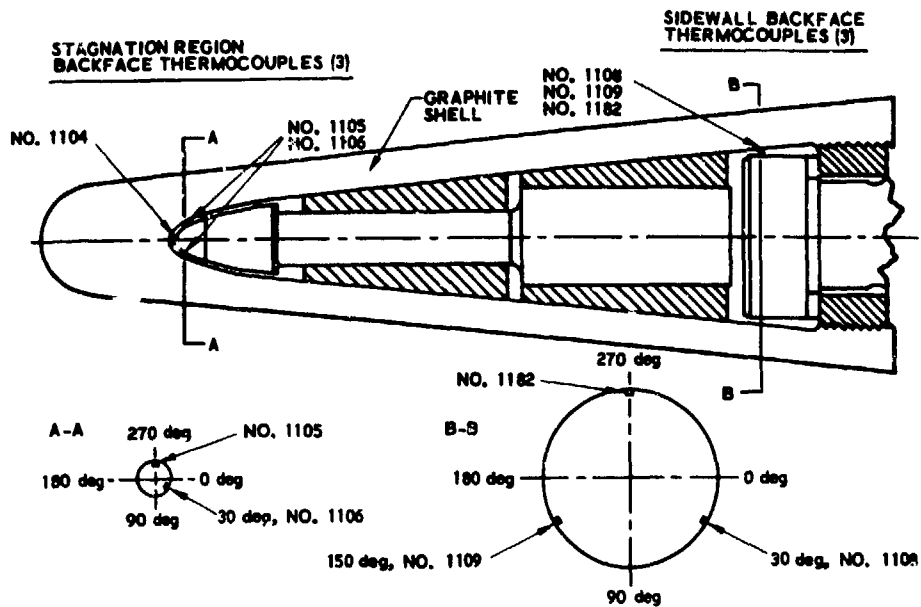


Figure 2-5. Graphite Shell Nostip Backface Temperature Instrumentation

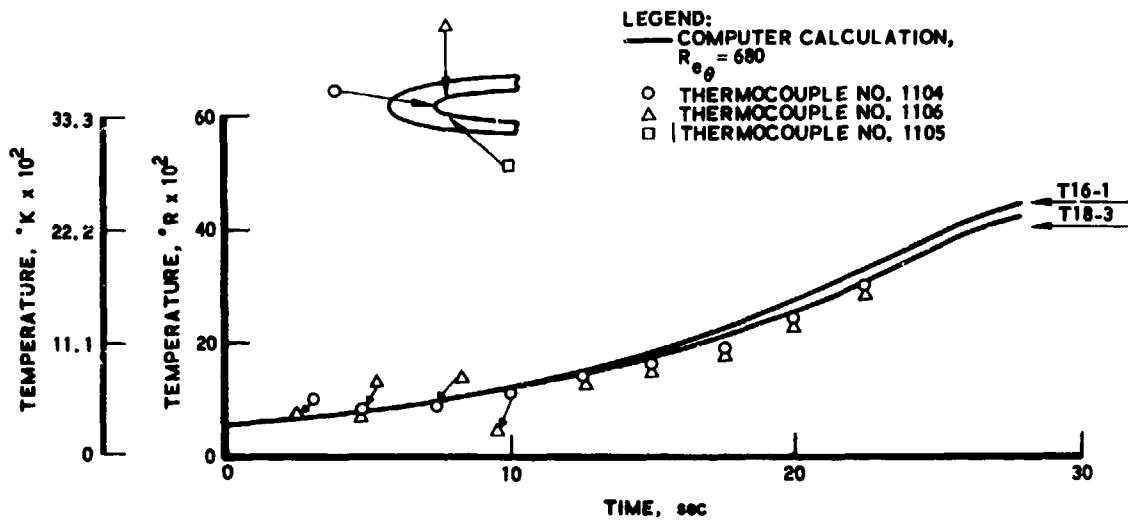


Figure 2-6. Stagnation Region Backface Temperature Response

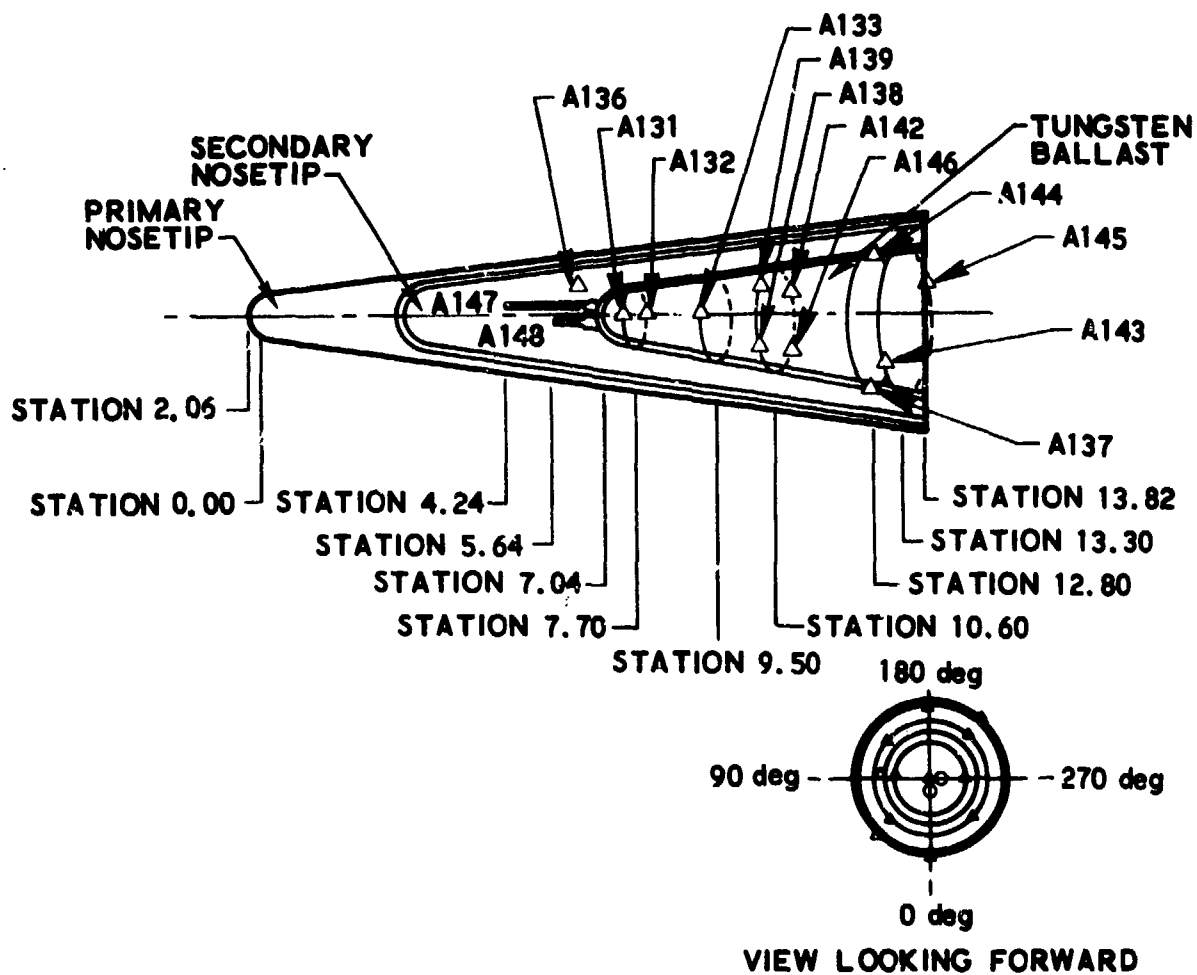


Figure 2-7. Nosetip With In-Depth Temperature Measurements

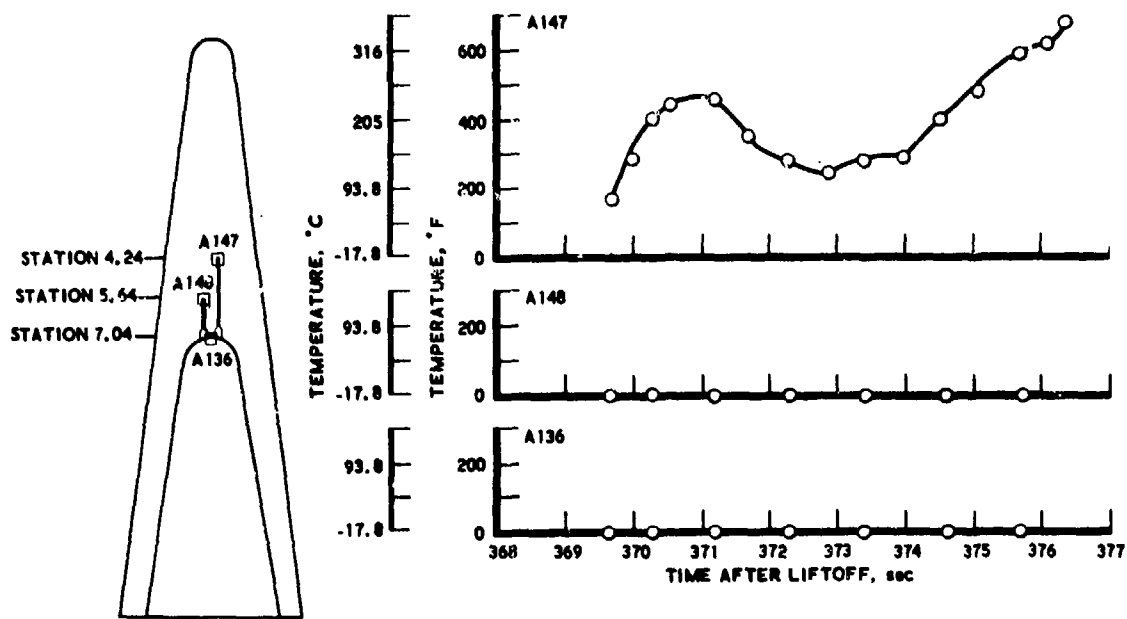


Figure 2-8. Nostip In-Depth Temperature Data

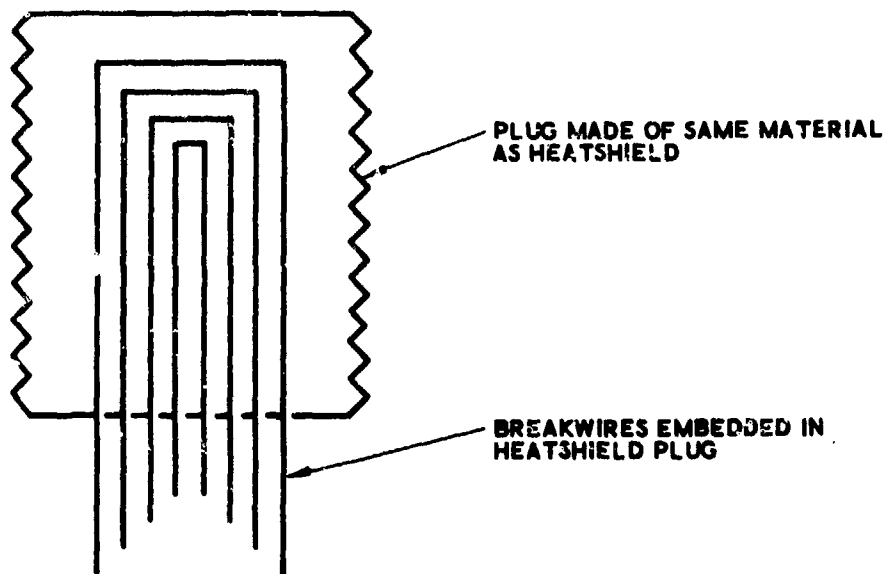


Figure 2-9. Breakwire Ablation Sensor

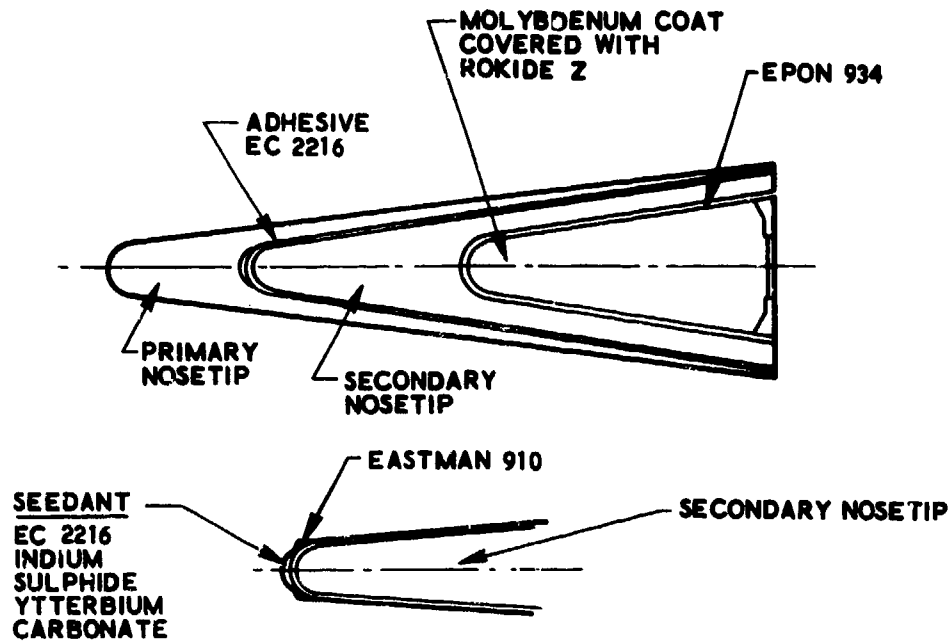


Figure 2-10. Nosetip Instrumented With Seedants

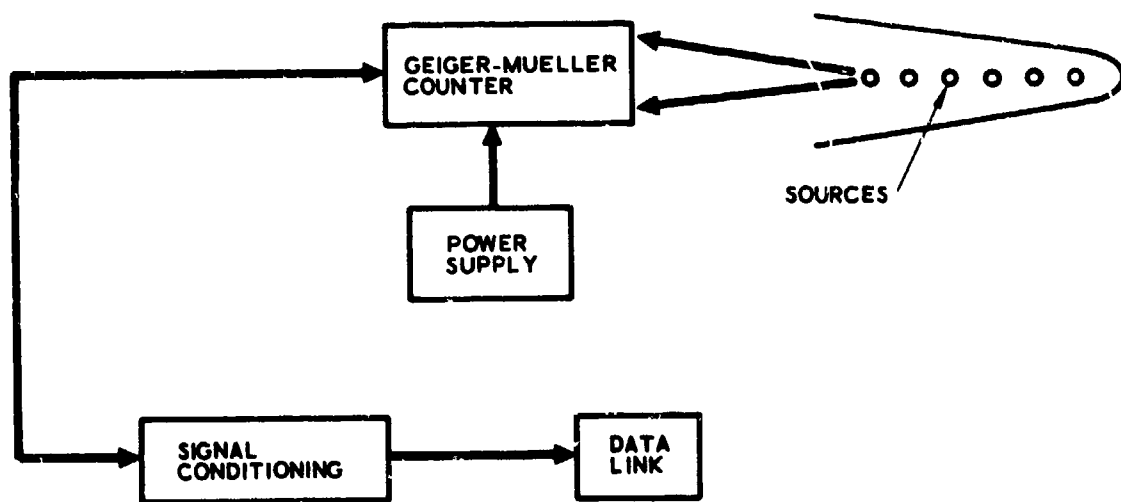


Figure 2-11. Radiation Transducer Sensor Block Diagram

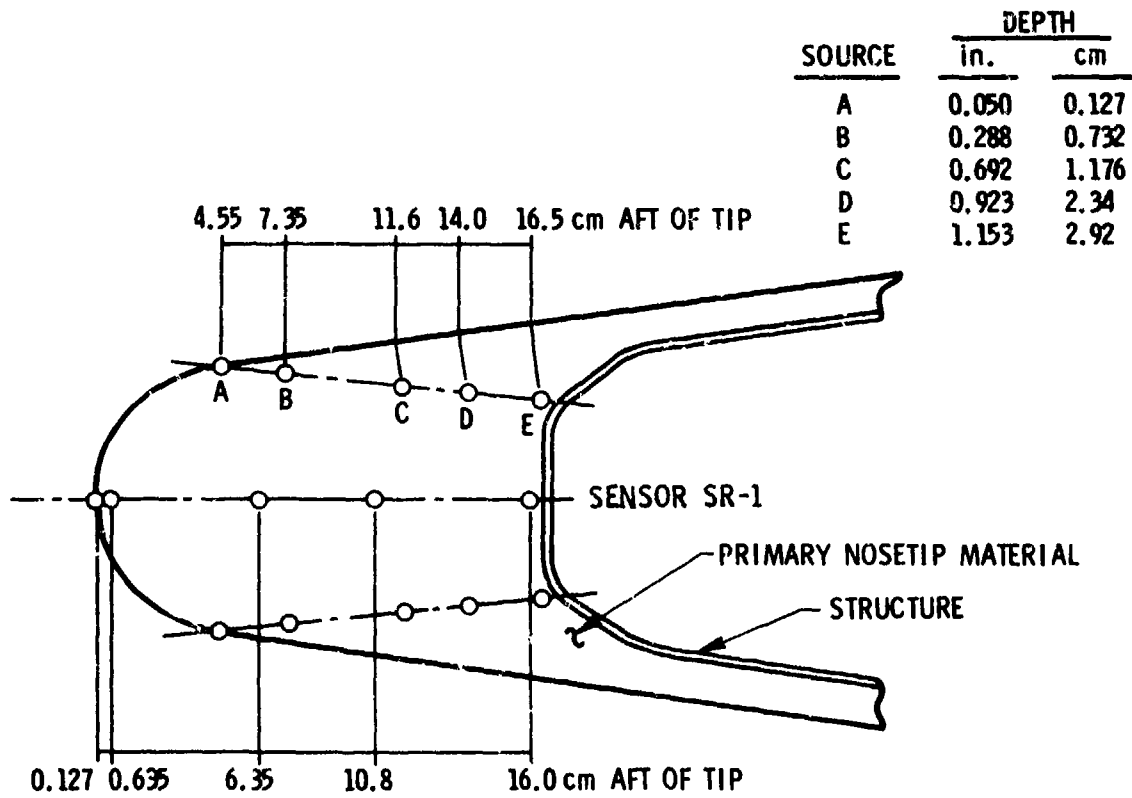


Figure 2-12. RAT Installation

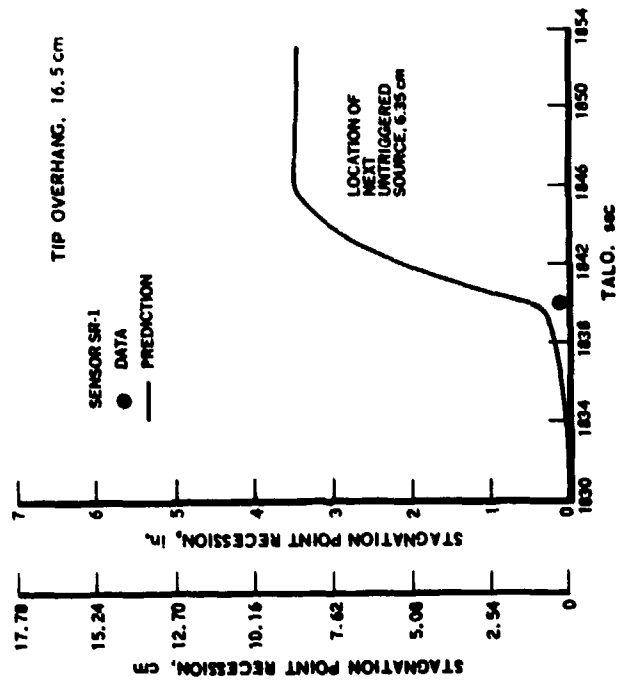


Figure 2-13. Stagnation Point Recession History

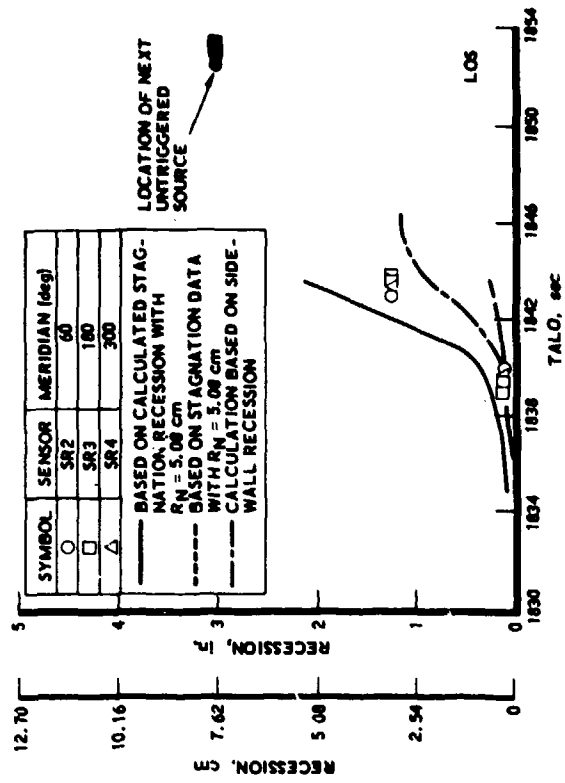


Figure 2-14. Recession Along 5-1/2-deg View Angle (Sonic Point)

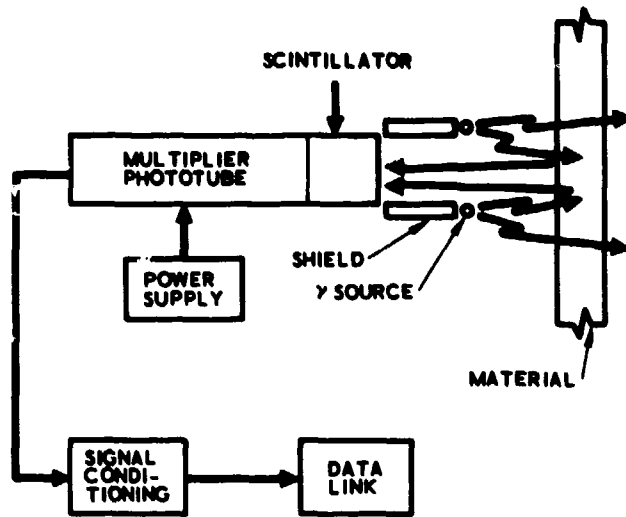


Figure 2-15. BRAG Sensor Block Diagram

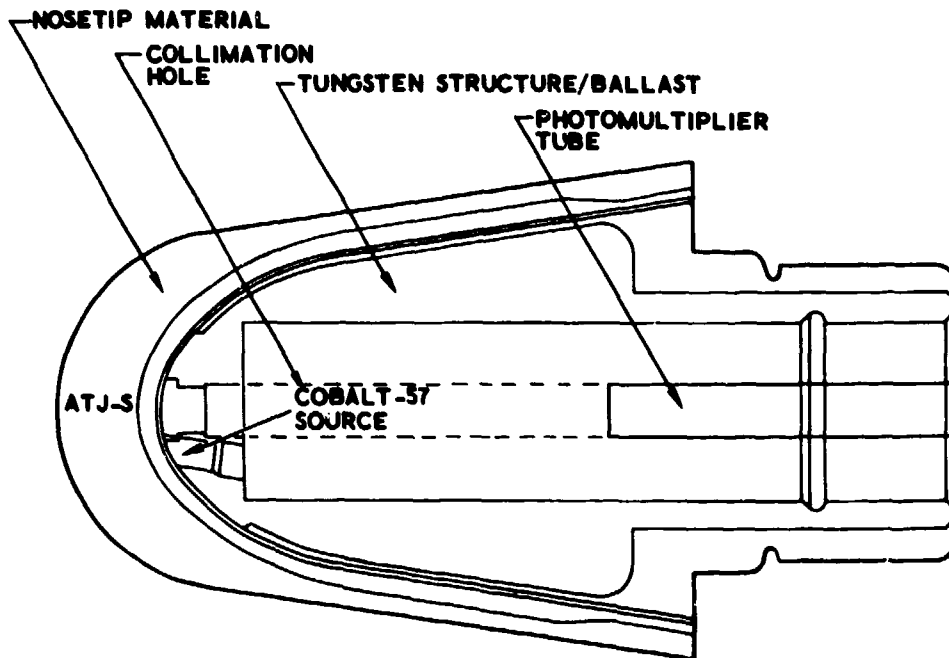


Figure 2-16. Nose Assembly With BRAG Sensor

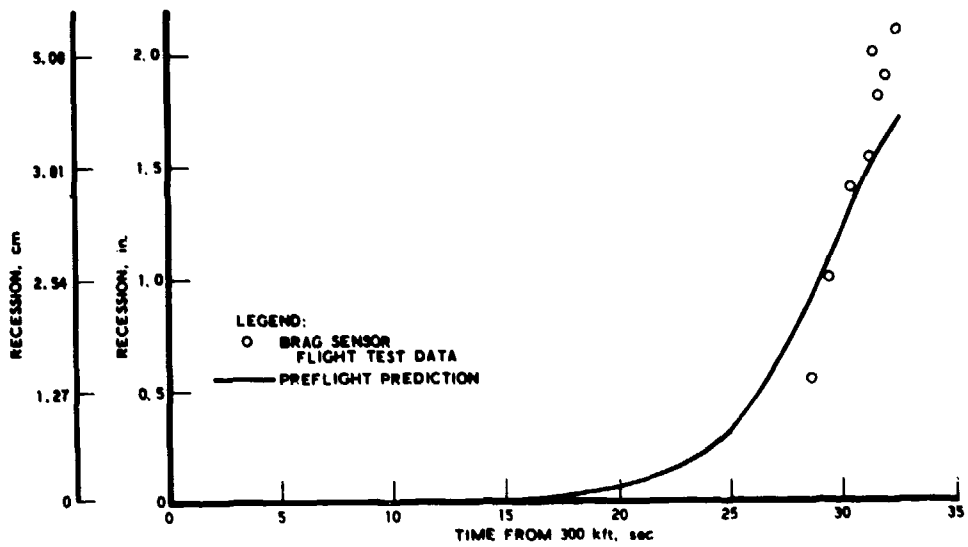


Figure 2-17. Nose Stagnation Point Recession - BRAG

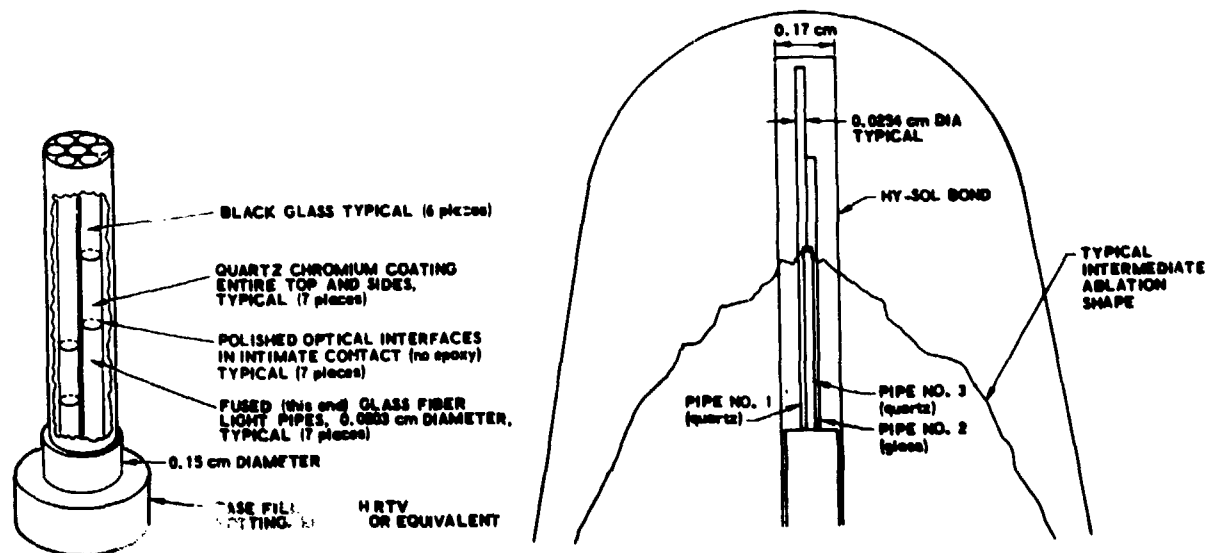


Figure 2-18. Light Pipe Ablation Sensor and Installation

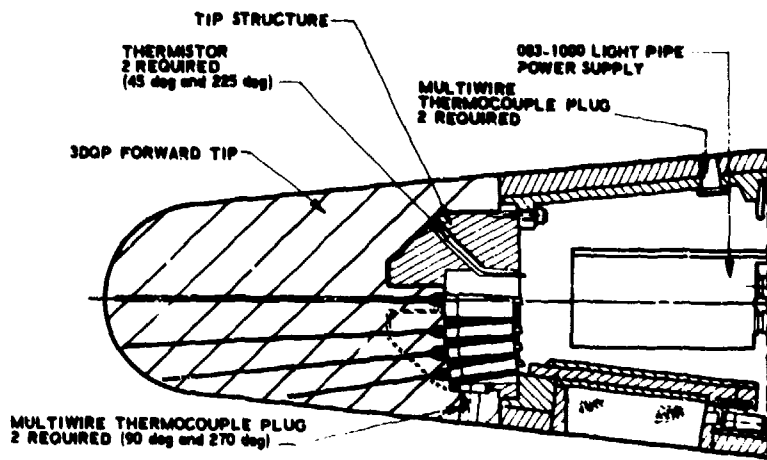


Figure 2-19. Light Pipe Instrumented Nosetip

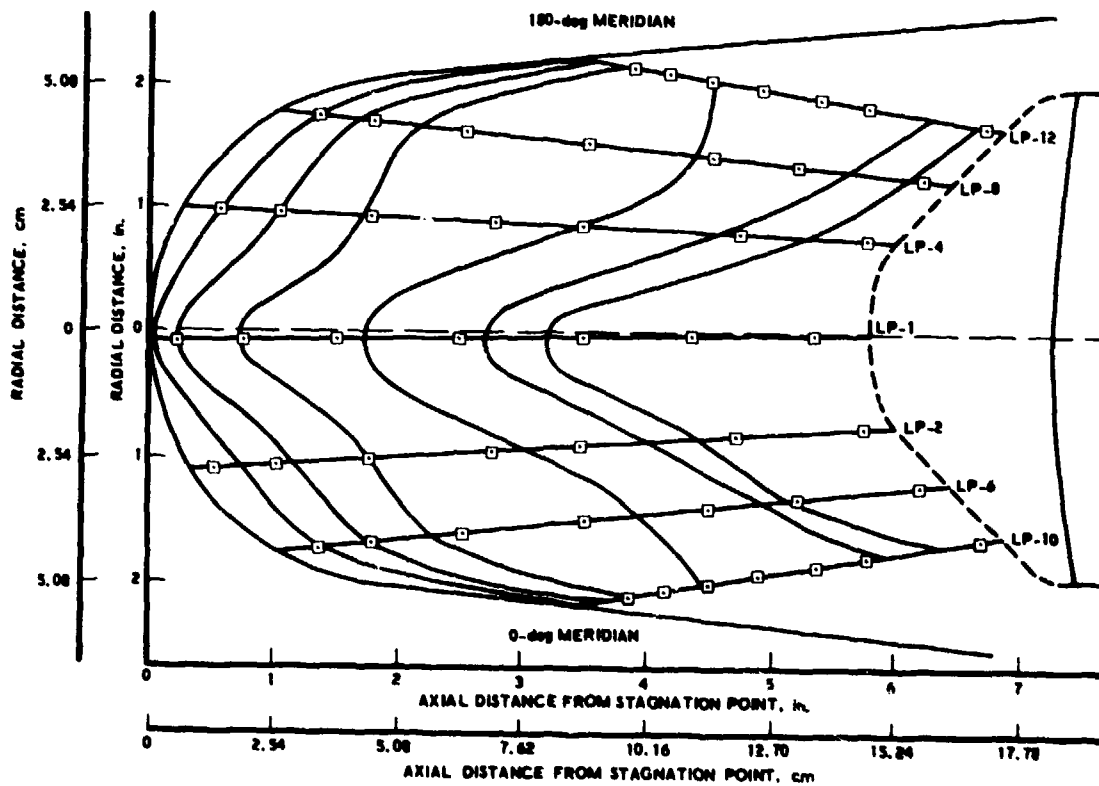


Figure 2-20. Light Pipe Vehicle Shape Change History

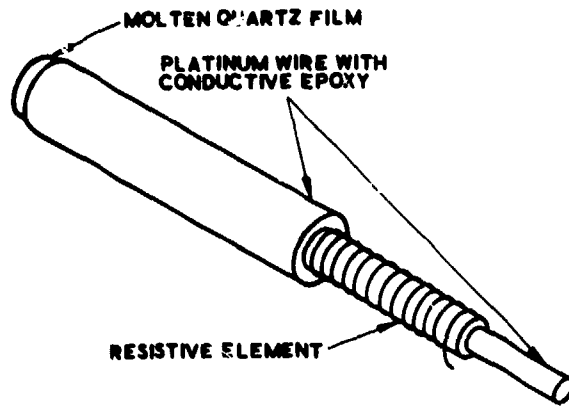


Figure 2-21. ARAD Sensor Design

R_1 = SENSOR RESISTANCE
 R_2 = CURRENT SOURCE RESISTANCE
 R_{Q1}, R_{Q2} = QUARTZ RESISTANCE

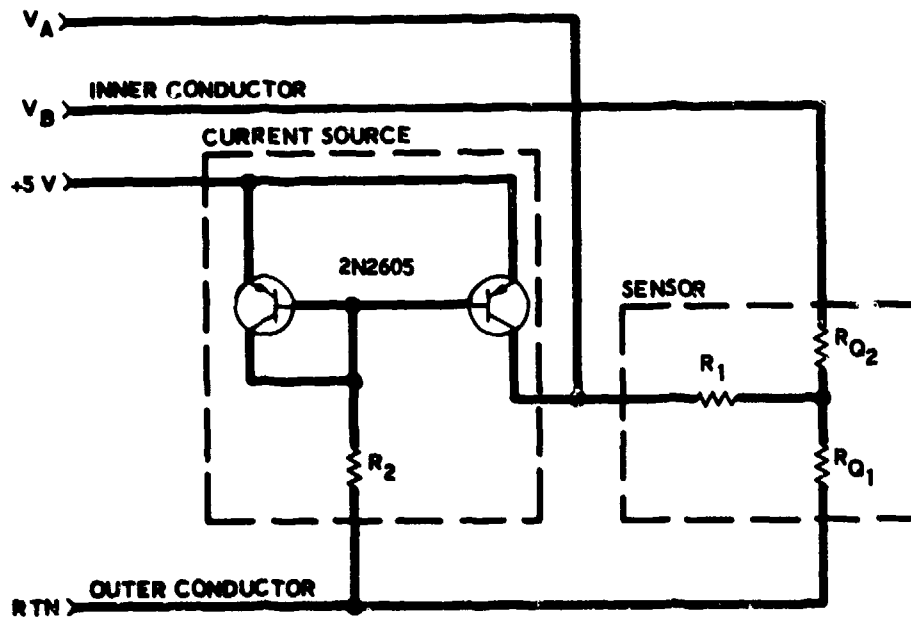


Figure 2-22. ARAD Schematic

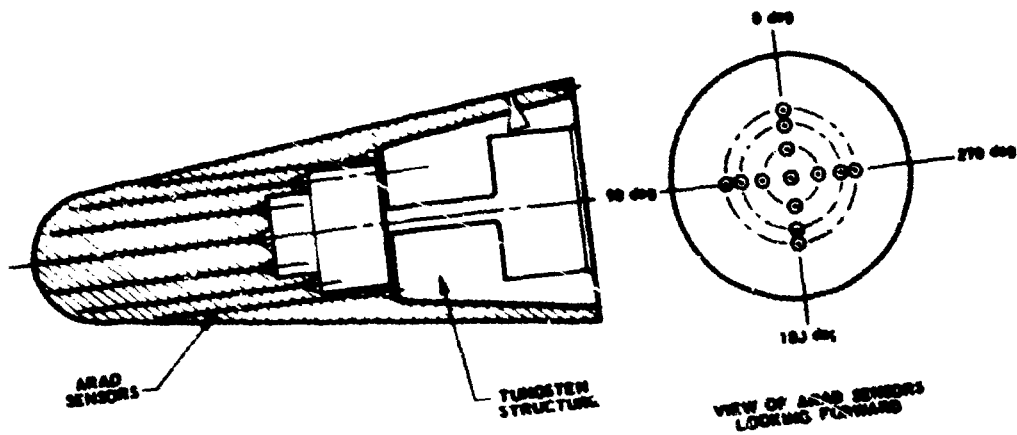


Figure 2-23. Nose Assembly With ARAD

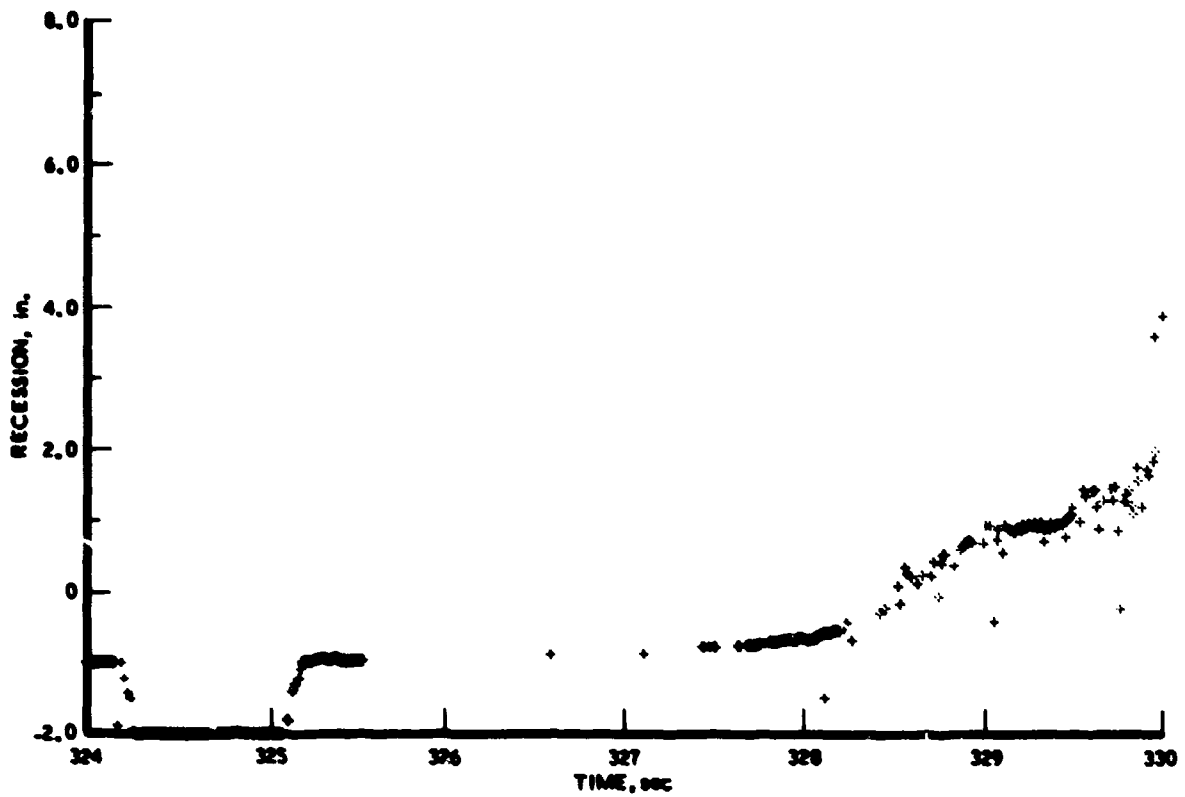


Figure 2-24. Nositip Recession History

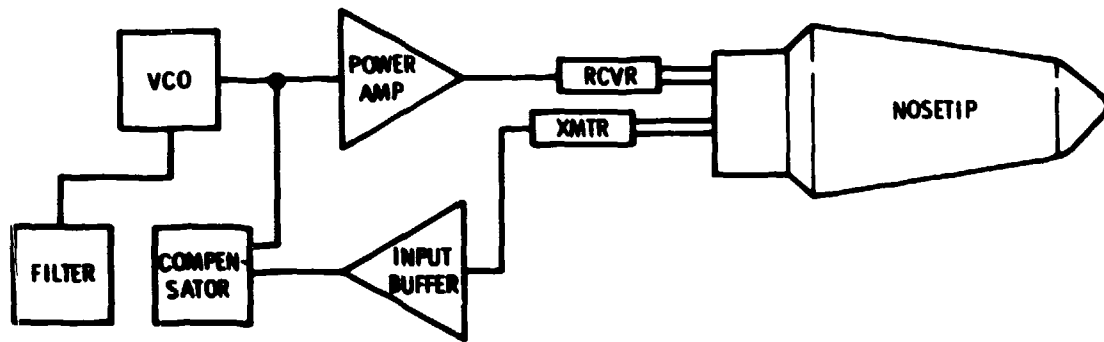


Figure 2-25. Nositip Acoustic Instrumentation

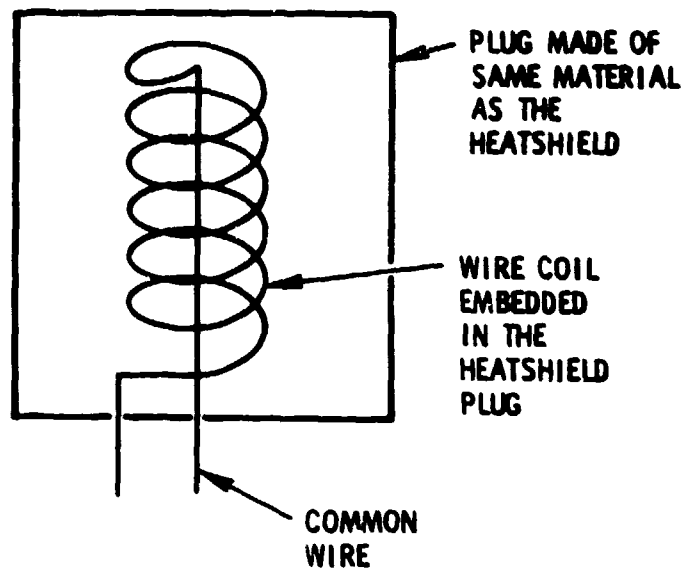


Figure 2-26. Makewire Gage

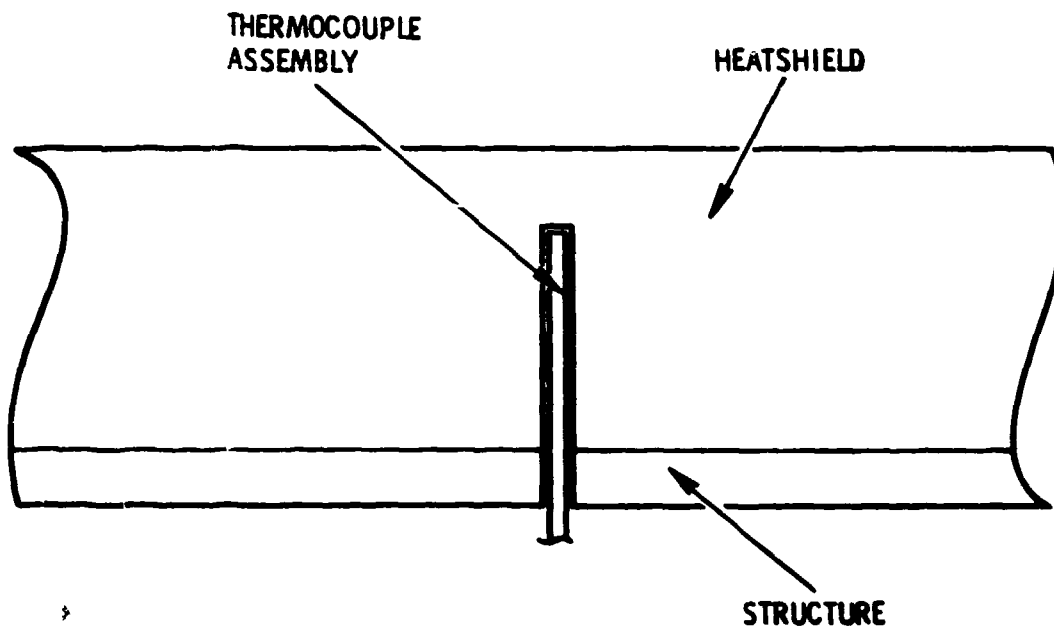


Figure 2-27. Post-Type Thermocouple Installation

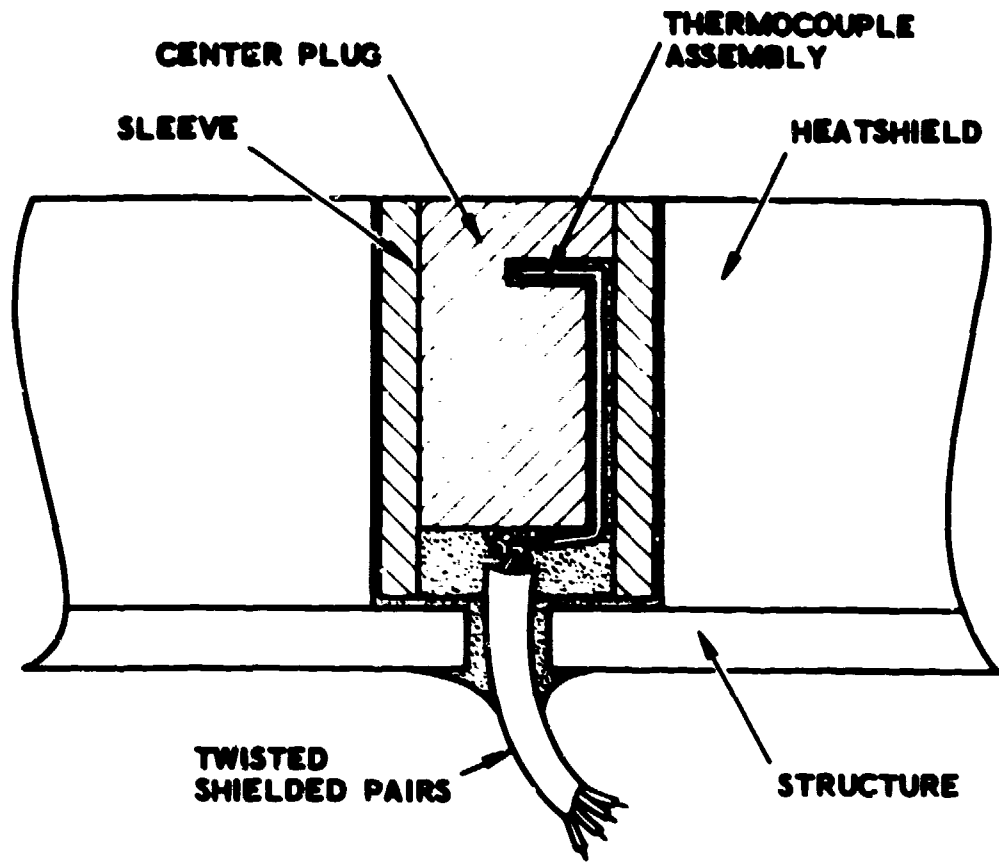


Figure 2-28. Isothermal-Type Thermocouple Installation

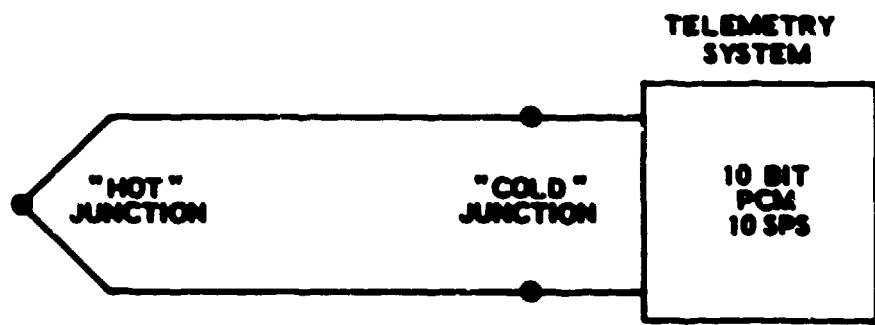


Figure 2-29. Typical Measurement System

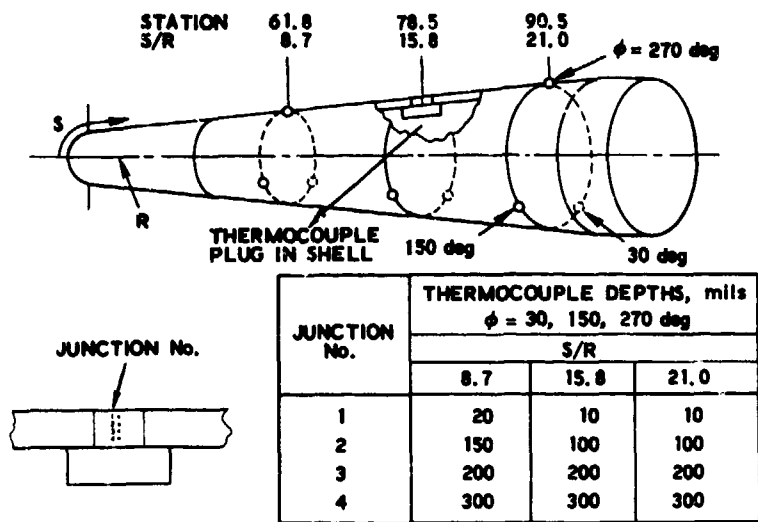


Figure 2-30. Frustum Shell Thermal Instrumentation

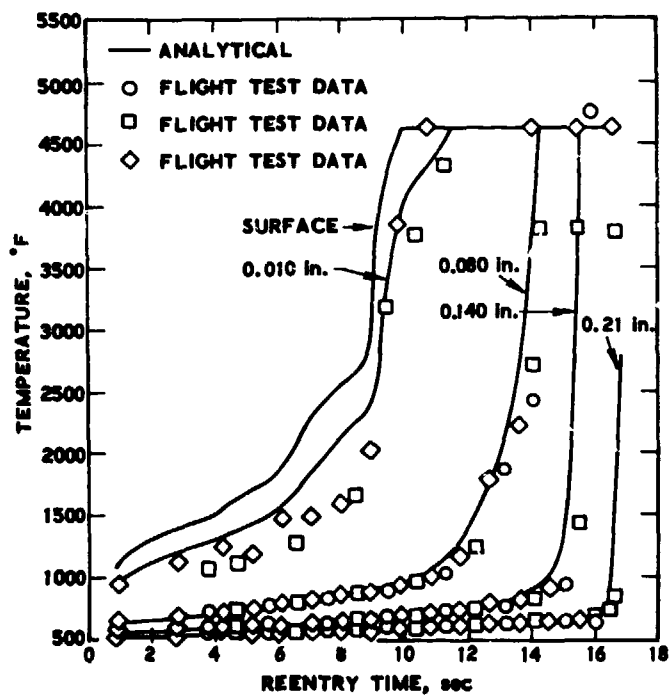


Figure 2-31. Isothermal-Type Thermocouple Temperature-Time History

3. AERODYNAMIC AND VEHICLE DYNAMIC INSTRUMENTATION

3.1 PURPOSE/INTRODUCTION

RV flight test programs require extensive on-board instrumentation in order to obtain aerodynamic and vehicle dynamic data with which to evaluate RV performance. Flight data represent the "real world" and are the only means by which reentry vehicle design parameters (maximum loads or maximum heating) can be validated. In addition, the phenomenology of specific technology areas, or "fixes," to a particular problem that cannot be simulated in ground test facilities can be fully evaluated during flight tests with the proper instrumentation. Obviously, flight instrumentation that are reliable, accurate, and inexpensive are needed to obtain the required data.

The most important aerodynamic and flight dynamic data that are generally obtained during a flight program are:

- a. Drag characteristics (total and components)
- b. Roll performance
- c. Angle of attack
- d. Stability
- e. Aerodynamic force and moment coefficients
- f. Axial and lateral loads
- g. Transition onset altitude

These typical performance parameters require evaluation for the R&D flight condition flown so that modeling techniques can be validated in order to make accurate predictions for extrapolation over the entire RV $V-\gamma$ map, including design conditions. A typical RV $V-\gamma$ map showing the entry conditions that the RV must be able to perform adequately, RV design conditions, and a typical R&D flight test matrix are shown in Figure 3-1.

The following section will deal with the required flight instrumentation needed to obtain the necessary technology data to meet the RV mission requirements. It should be noted that all of the instruments described, photographs shown, and typical data are based on ballistic RVs. The instrumentation, however, is directly applicable to maneuvering RVs.

3.2 FLIGHT INSTRUMENTATION PRINCIPLES

Table 3-1 represents the technology parameters desired from the flight program and the flight instrumentation required for the measurement. Some of the instruments required to determine transition onset altitude have been discussed in Section 2.

Table 3-1. Technology Parameter/Flight Instrumentation Requirements

Technology Parameter	Instrumentation/Data
Drag Characteristics	Axial accelerometers and pressure sensors
Roll Performance	Roll rate gyro's/magnetometers
Angle of Attack	Lateral accelerometers, pitch and yaw rate gyro's, inertial platforms
Stability ($C_{m\alpha}$, X_{cp})	Motion data, lateral accelerometer, pitch and yaw rate gyros
Axial and Lateral Loads	Accelerometers
Transition Onset Altitude	Thermal gages (rate calorimeters) acoustic gages, base pressure, and accelerometer data

3.2.1 Accelerometers (Axial and Lateral)

Accelerometers are used to measure axial and lateral "g" acceleration loadings from which aerodynamic performance parameters can be derived. The two basic types of accelerometers that have been used in past RV programs are the simple displacement potentiometer-type sensor and the more sophisticated force balance vernier step accelerometer-type

sensor. Figure 3-2 shows a schematic of the displacement-type accelerometer that consists of a seismic mass, a spring, and a dash pot damper. The readout of this type of sensor is generally made by a potentiometer voltage divider. Figure 3-2 also shows a schematic of the accelerometer with acceleration applied and the sensor at zero g's.

The potentiometer displacement accelerometer has been the most commonly used on RV flight programs during the past decade. When these sensors are used in axial load measurements (basically to derive the drag), they are usually employed in overlapping ranges such as 0 to 5 g's, 0 to 20 g's, 0 to 40 g's, and 0 to 100 g's. The above sensor ranges provide total drag measurements from ~ 140 kft to impact and, of course, cover the flow regimes from laminar, transitional, and turbulent flow. The displacement accelerometer is relatively inexpensive and rugged, but it has limited resolution and accuracy due to the fact that the output is governed by a wiper arm/potentiometer mechanism that is proportional to the "g" loads as previously discussed. A typical analog trace of a coarse range (0 to 100 g's) displacement potentiometer-type accelerometer is shown on Figure 3-3 for axial loads.

A second type of accelerometer in use is the force balance accelerometer. This type of accelerometer also employs a seismic mass similar to the displacement-type accelerometer. However, the force balance accelerometer has a constrained seismic mass and senses a slight displacement due to acceleration in the sensitive plane. The amount of force required for constraint (force balance) to restore the seismic mass to the null position is proportional to the acceleration applied. The null position is generally measured by an inductive coil and an amplified signal as shown in Figure 3-4. The force balance accelerometer is significantly more accurate and has infinite resolution. These features provide the opportunity for two major innovations. The first is the dual-range accelerometer, which is simply a force balance accelerometer with one sensing unit having a dual output consisting of two amplified levels (Figure 3-5). A typical dual-range

accelerometer, which is currently being flown on RVs, has a range of ± 3 g's and ± 30 g's. This sensor is being used to measure lateral loads in the pitch and yaw planes.

The second innovation, the vernier step accelerometer, was developed because today's sophisticated technology for weapons systems RVs requires highly accurate measurements. It has been successfully flown on several flight programs. The vernier accelerometer has five basic ranges in one single instrument and is more accurate and has better resolution than the pot-type displacement or the dual-range, force balance accelerometer; however, the vernier accelerometer is significantly more expensive. The vernier step accelerometer also operates on the force balance principle and has five amplified levels operating off the same sensing element. This instrument provides very accurate drag measurements. One channel provides a 0 to 5.0-V full-scale output having ranges from +1, to -3, -2 to -10, -8 to -24, -20 to -52, and -44 to -108; a second output defines the range at which the sensor is operating (Figure 3-6). This sensor is currently being utilized to measure axial g's on RVs. A typical analog trace from a vernier step accelerometer is shown in Figure 3-7. Axial accelerometer data are utilized to determine the axial force coefficient (C_x), which is the major component of drag and will be discussed in Section 4.

Lateral accelerometers can be either the pot displacement or the force balance type and are used in overlapping ranges in the pitch and yaw planes of the RV. Typical pot sensor ranges are ± 10 g's and ± 40 g's and ± 100 g's or ± 3 , ± 30 g's for the dual-range force balance sensors. Lateral accelerometers provide several important inputs to determine the RV performance. These are:

- a. Lateral loading
- b. RV total angle-of-attack history
- c. RV trim angle of attack
- d. The presence of nosetip asymmetries
- e. Normal force coefficient slope ($C_{n\alpha}$)

Typical flight test data from displacement pot-type lateral accelerometers in overlapping ranges (± 10 g's, and ± 100 g's) are shown in Figure 3-8. Note that fine range accelerometers (± 10 g's) show undamping at time t_1 . This undamping is a natural and expected phenomenon in which the RV angle of attack diverges slightly when the transition front moves on to the aft end of the RV. The vehicle damps out at time t_2 when the transition front moves forward. Note that both pitch and yaw accelerometers show low lateral load levels throughout the flight. This is indicative of good nosetip/RV performance. The angle of attack is derived from knowledge of the dynamic pressure, the normal force slope coefficient, and the lateral loads history and will be described later. Figure 3-9 shows a typical trace of an RV with a dual-range force balance lateral vehicle accelerometer having ranges of ± 3 and ± 30 g's. Typical angle-of-attack histories will be shown in a subsequent section. In addition to the axial and lateral accelerometers providing drag and angle of attack, they also provide a direct measure of "g" loading experienced by the RV to assess structural margins.

3.2.2 Rate Gyros

Rate gyros operate on the principle of measuring the force required to give a rotating mass angular motion rate. The rate of an angular motion perpendicular to the plane of rotation requires a proportional force to overcome the gyroscopic force and is sensed electronically. Figure 3-10 illustrates the principle of a single-axis rate gyro. Figure 3-11 is a photograph of a typical dual-axis rate gyro.

Rate gyros are utilized in the pitch and yaw planes of an RV to determine the pitch/yaw rate magnitude and frequency. Analog traces of raw flight data from the pitch and yaw rates for a typical RV flight are shown in Figure 3-12. It will be shown in Section 4 how these data are utilized to determine basic body frequency and, hence, the stability parameter C_{m_q} , which is the resultant center of pressure and static margin history for the flight vehicle.

Rate gyros are also utilized to measure the roll rate of an RV during reentry. An analog trace of the roll rate history for a typical RV is shown in Figure 3-13.

3.2.3 Magnetometers

A magnetometer is an instrument that measures the intensity and direction of magnetic forces. Magnetometers are utilized on RVs to measure the roll rate and to determine direction of the axes in inertial space relative to the earth for detailed trajectory reconstruction.

Figure 3-14 is a photograph of a typical flight unit. Raw flight data from a magnetometer are presented in Figure 3-15. The data show an increase in frequency during reentry due to the normal roll rate buildup.

3.2.4 Inertial Platforms

Inertial platforms are sophisticated instruments that determine RV altitude and angle-of-attack histories. However, these instruments are bulky and expensive when compared to accelerometers and rate gyros that can perform the same function with slightly less accuracy. Accelerometers and rate gyros provide adequate flight data for most ballistic RVs. Inertial platforms have been used on ballistic RVs where extreme accuracy is required or a detailed technology flight experiment is being implemented. However, the most common and ideal use for an inertial platform is on maneuvering RVs. Inertial platforms are beyond the scope of this paper.

3.2.5 Pressure Sensors (Steady State)

The majority of flight pressure sensors in use today⁽³²⁾ rely on a diaphragm or aneroid capsule to sense the pressure difference between the pressure to be measured and a vacuum reference pressure. The pressure differential causes a diaphragm to bend or flex and produces a diaphragm displacement proportional to the pressure applied to the sensor. Diaphragm displacement can be sensed mechanically via a linkage, wiper arm, and potentiometer similar to the "Pot" sensor shown in Figure 3-16. Another

way to sense diaphragm displacement is with strain gages (bonded, unbonded, or diffusion-deposited), which measure diaphragm displacement by resistance bridge and the accompanying imbalance that is proportional to the pressure applied. A typical solid state, strain gage pressure sensor is shown in Figure 3-17. These sensors are generally utilized to measure RV forebody and base pressure data having a range from 0 to 5 psia to 0 to 100 psia. Typical forebody flight test pressure data using a solid state strain gage are presented in Figure 3-18.

A final way to determine diaphragm displacement is by variations in capacitive or inductive coupling; this technique is generally employed on low range pressure sensors, which are more sensitive, tend to be larger, and are used to detect transition onset from base pressure measurements.

These sensors have ranges from 0 to 0.1 psia to 0 to 5.0 psia and rely on the capacitance or reluctance principle. Figure 3-19 shows a photograph of a low range, 0- to 0.5-psia, variable capacitance pressure sensor. Figure 3-20 shows low range, raw base pressure data for a typical RV flight test. Figure 3-21 shows raw flight test data from a high range, 0- to 5-psia sensor used to determine the base drag component of total drag.

Section 4 will deal with the utilization of pressure data to obtain the drag components of total drag for definition of the aerodynamic performance of an RV.

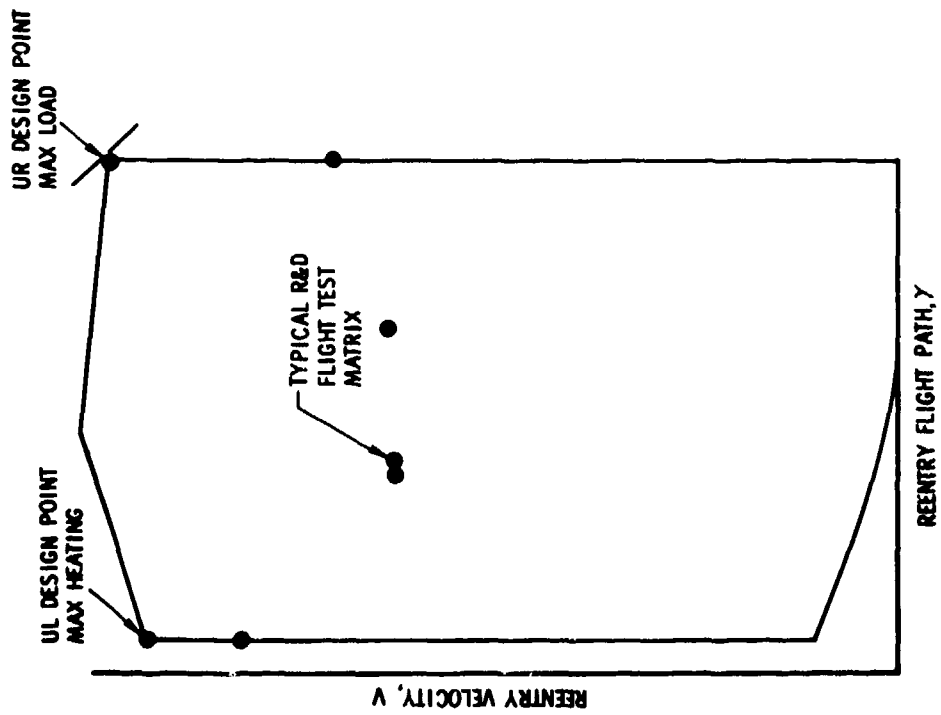
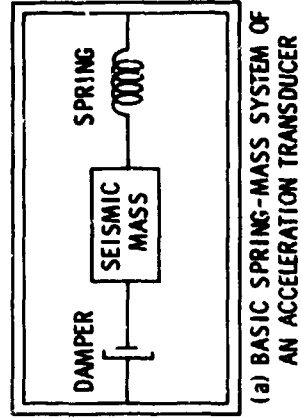
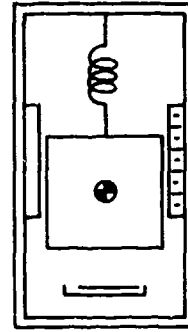


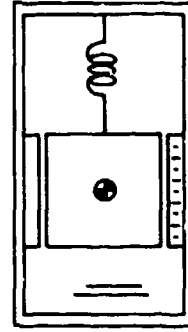
Figure 3-1-1. Typical V-gamma Map



(a) BASIC SPRING-MASS SYSTEM OF AN ACCELERATION TRANSDUCER



(b) ACCELERATION APPLIED



(c) ACCELERATION REMOVED

Figure 3-2. Single Range-Type Displacement Accelerometer

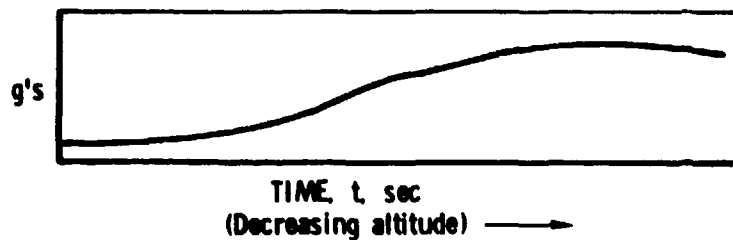


Figure 3-3. Typical Axial Accelerometer Flight Data (Displacement-Type Pot Sensor)

ACCELEROMETER

MEASURES FORCE REQUIRED TO ACCELERATE AN INERTIAL MASS TO SAME ACCELERATION AS VEHICLE

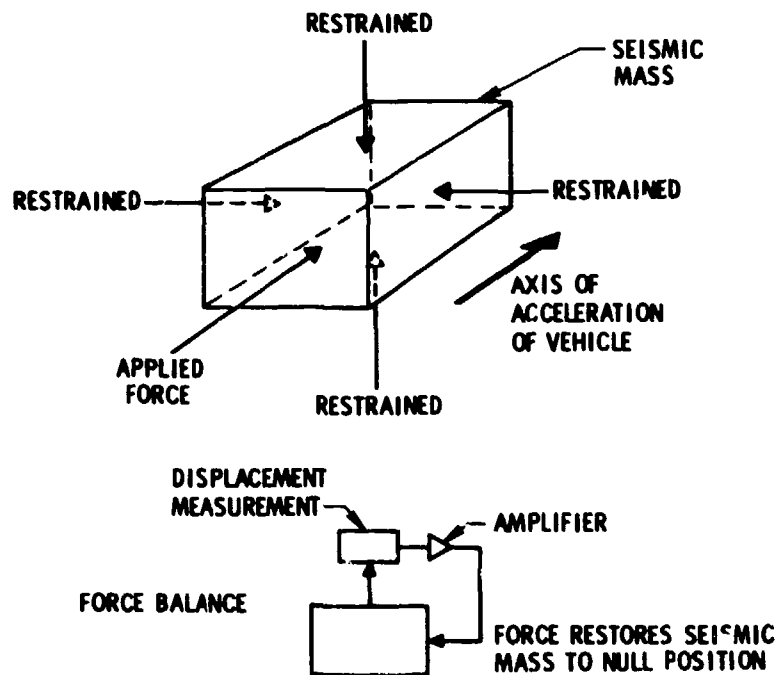


Figure 3-4. Force Balance-Type Accelerometer Schematic

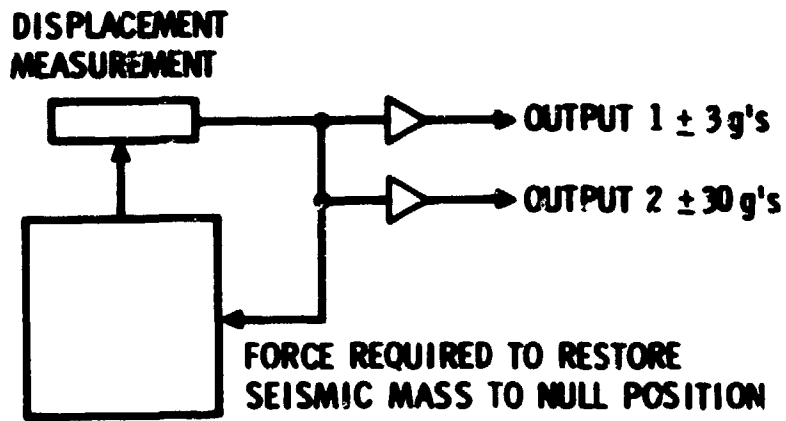


Figure 3-5. Dual-Range Force Balance Accelerometer Schematic

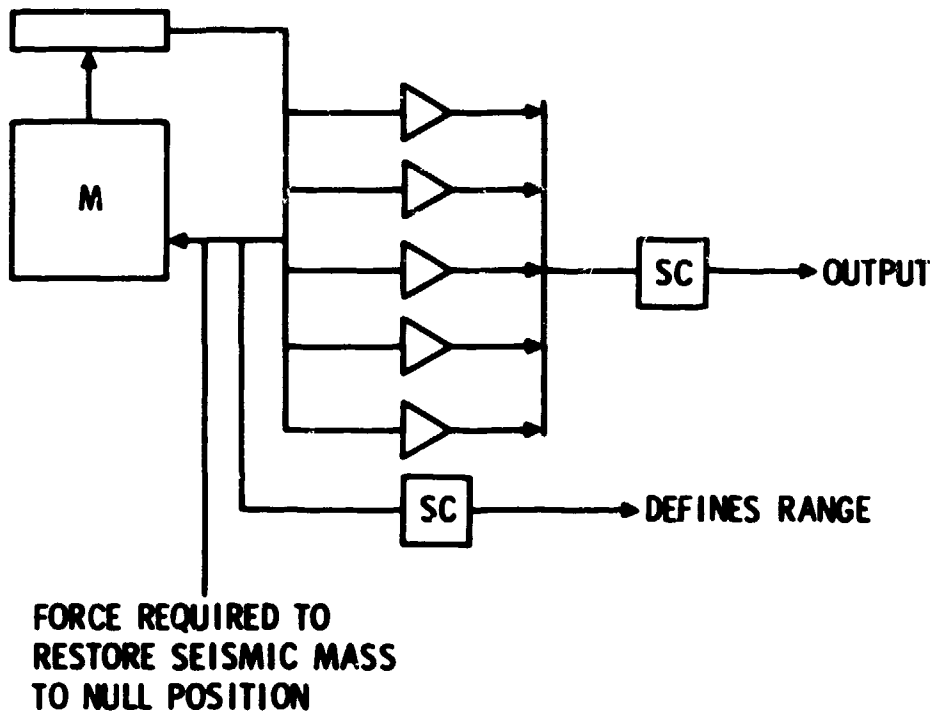


Figure 3-6. Vernier Step Accelerometer Schematic

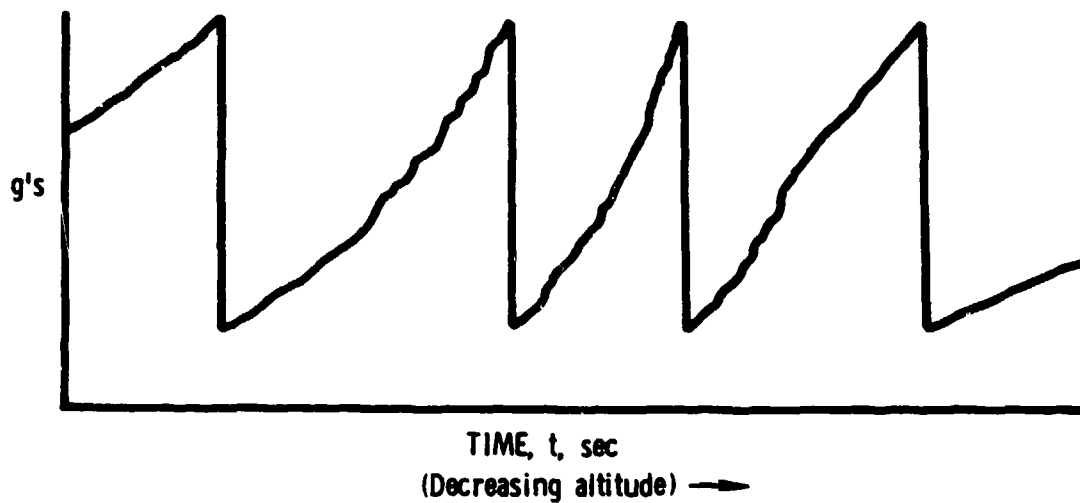


Figure 3-7. Typical Flight Data - Vernier Step Accelerometer Output

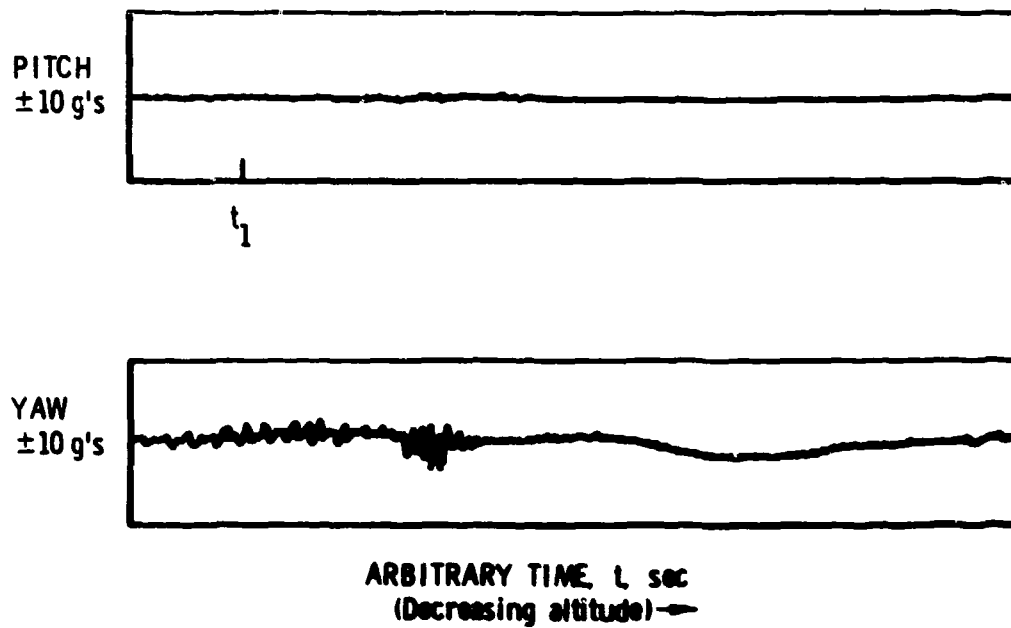


Figure 3-8. Typical Analog Traces of Raw Lateral Accelerometer Flight Data

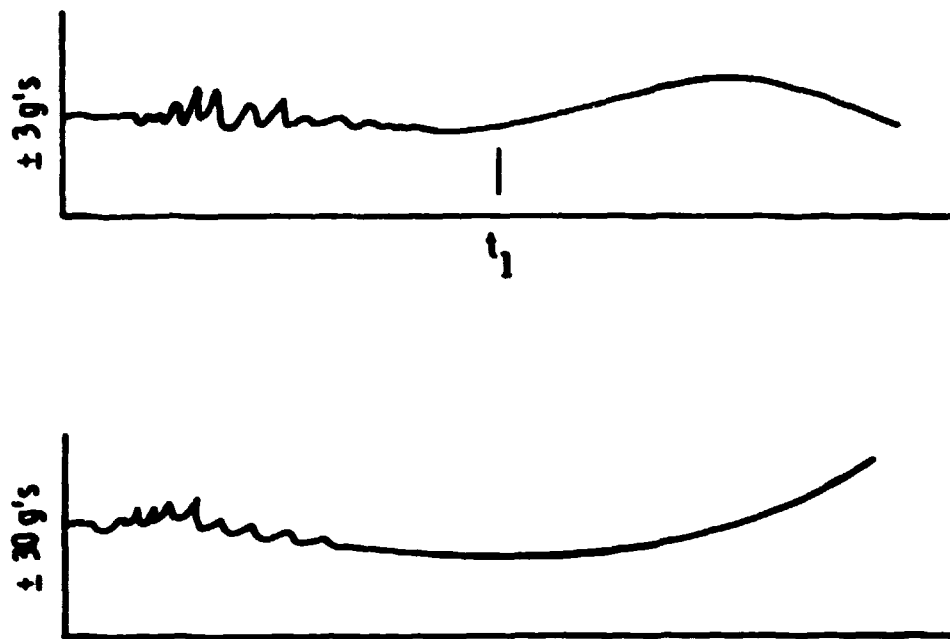


Figure 3-9. Typical Lateral Accelerometer Showing Trim Buildup

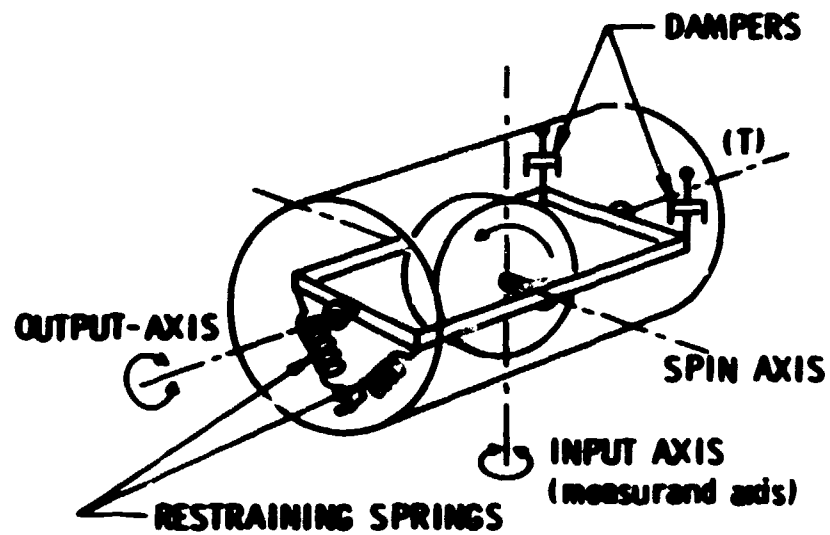


Figure 3-10. Pitch and Yaw Rate Gyro

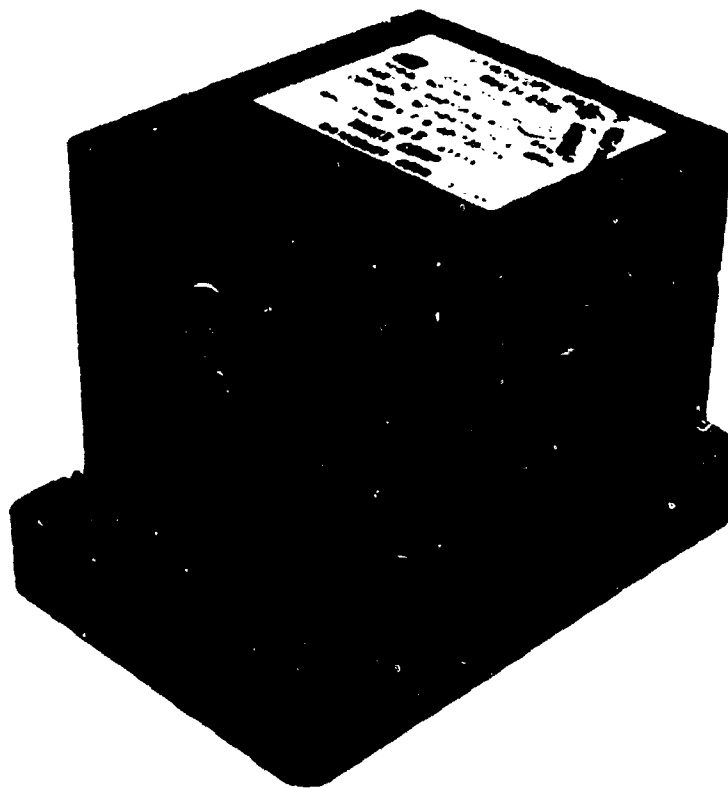


Figure 3-11. Dual-Axis Rate Gyro

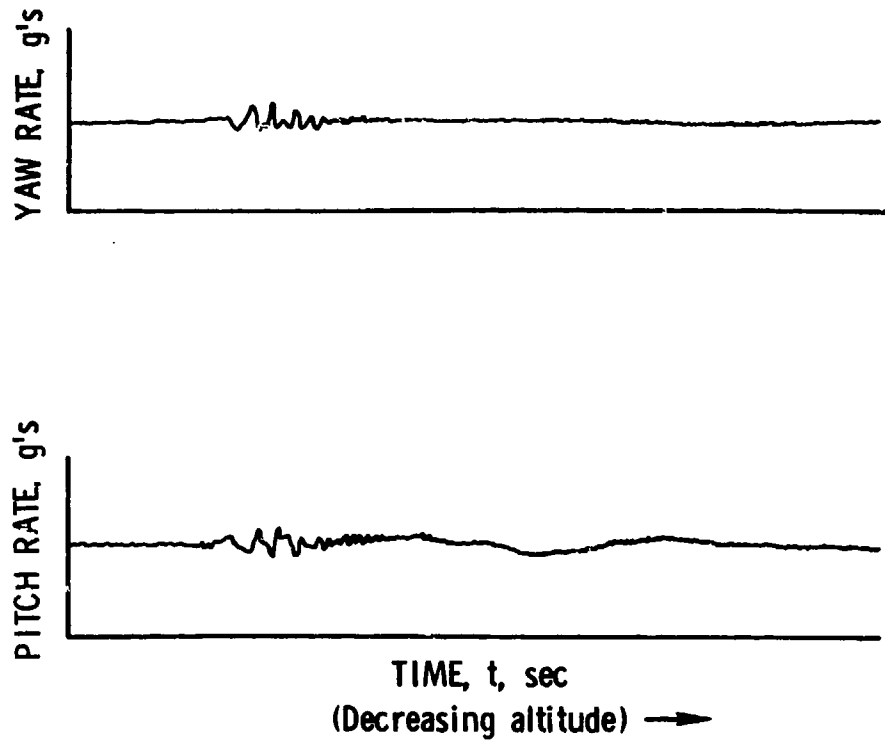


Figure 3-12. Raw Flight Data for Pitch and Yaw Rate Gyro From a Typical Reentry Vehicle

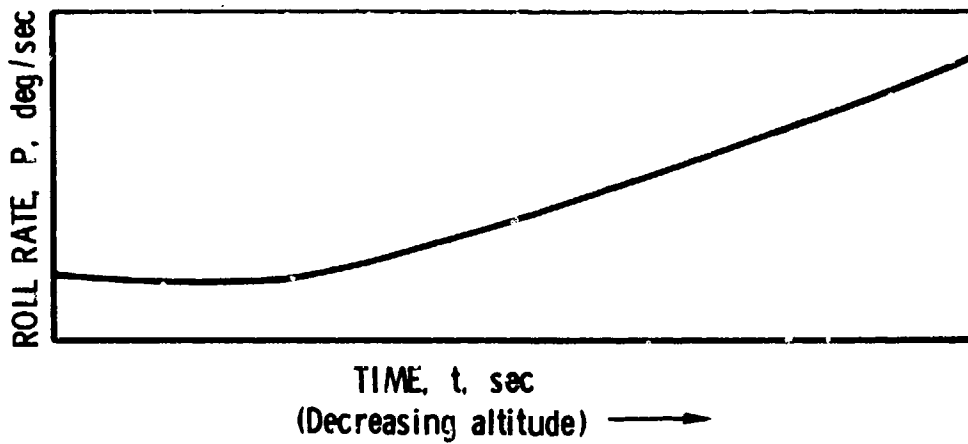


Figure 3-13. Raw Roll Rate Flight Data for a Typical Reentry Vehicle

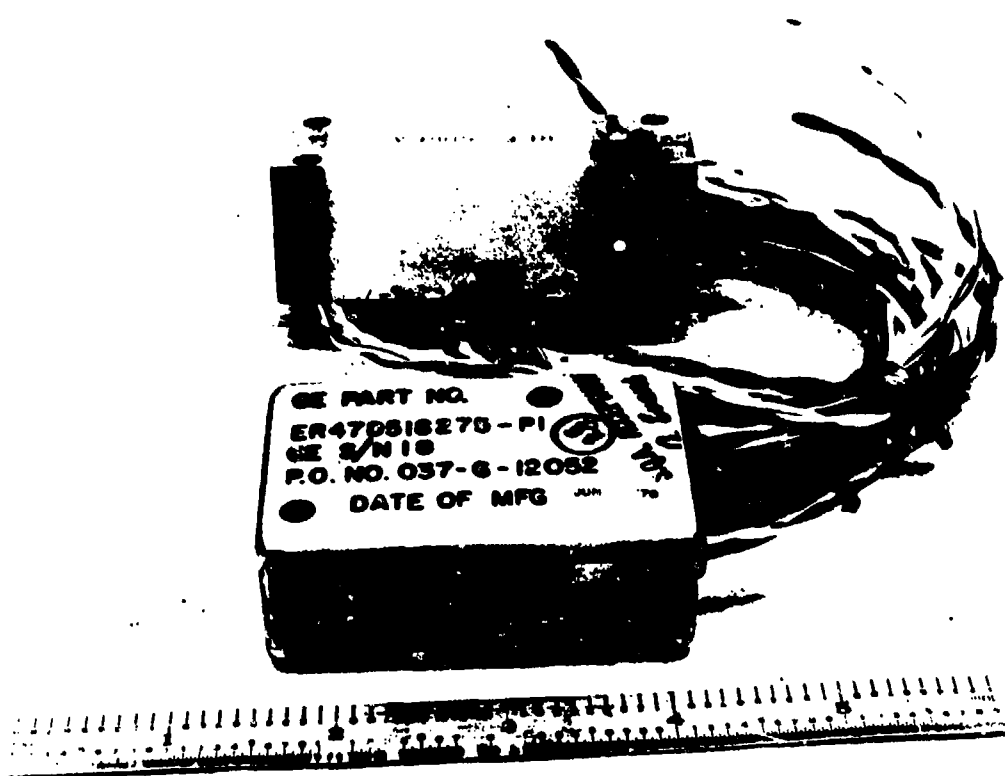


Figure 3-14. Magnetometer

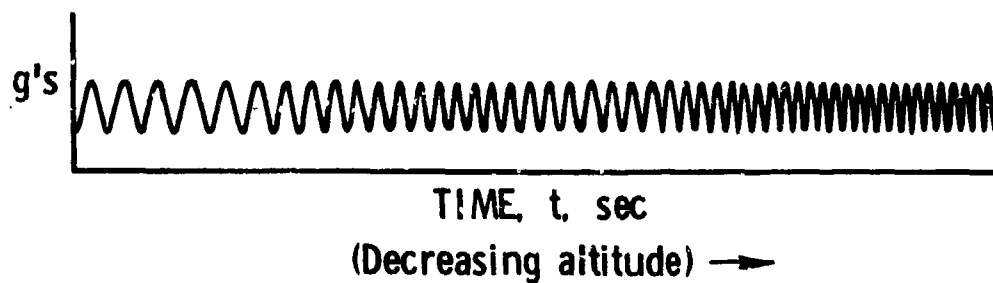


Figure 3-15. Typical Raw Magnetometer Flight Data

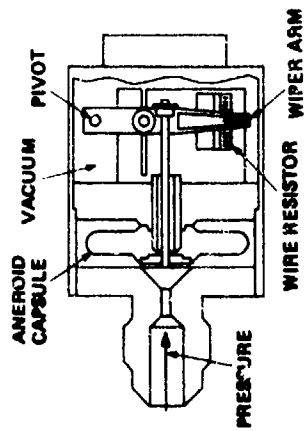
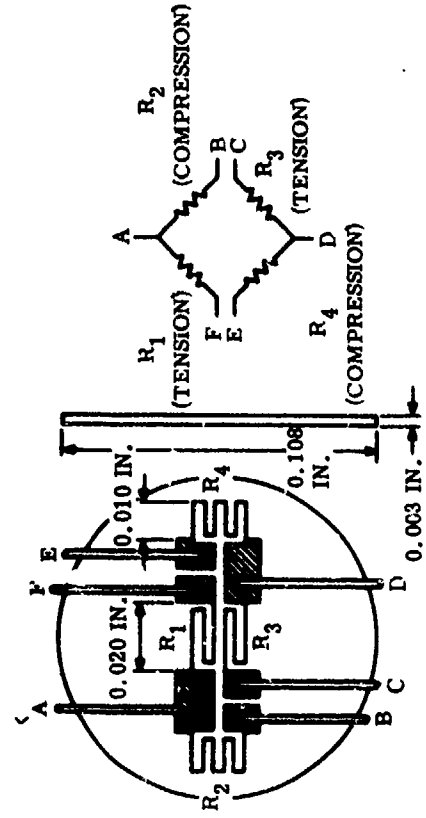
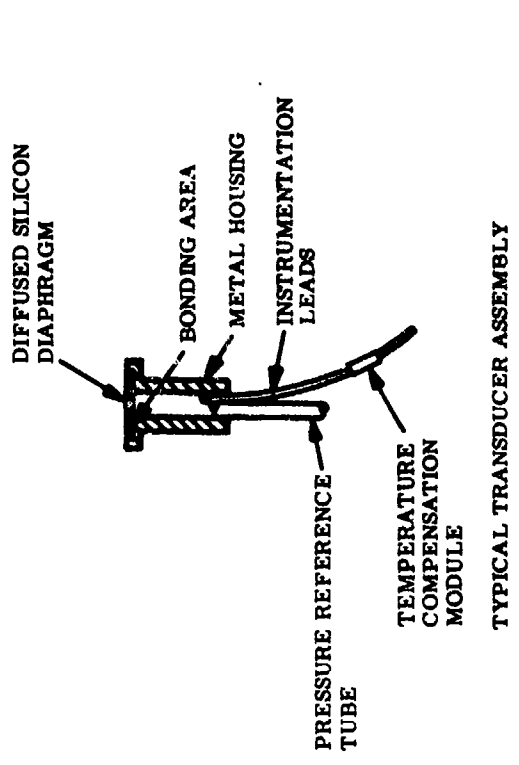


Figure 3-16. Potentiometer Pressure Sensor (Early Generation Steady State)



INTEGRAL SILICON DIAPHRAGM CONTAINING A FOUR-ACTIVE ARM WHEATSTONE BRIDGE.

Figure 3-17. Flight Pressure Sensor

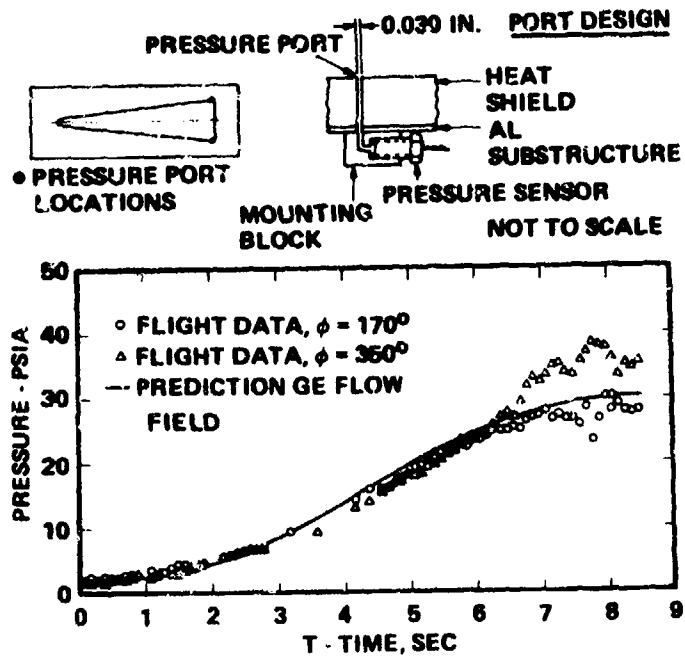


Figure 3-18. Pressure Sensor/Port Flight Experiment

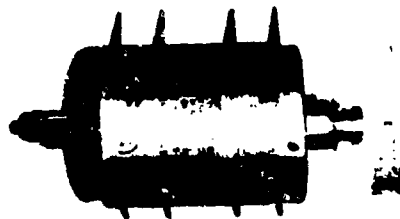


Figure 3-19. Capacitance Pressure Sensor

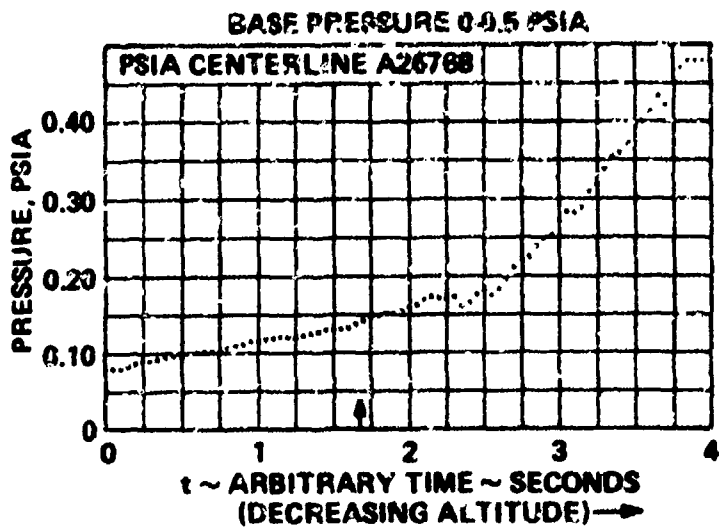


Figure 3-20. Transition Indicators (Flight B)

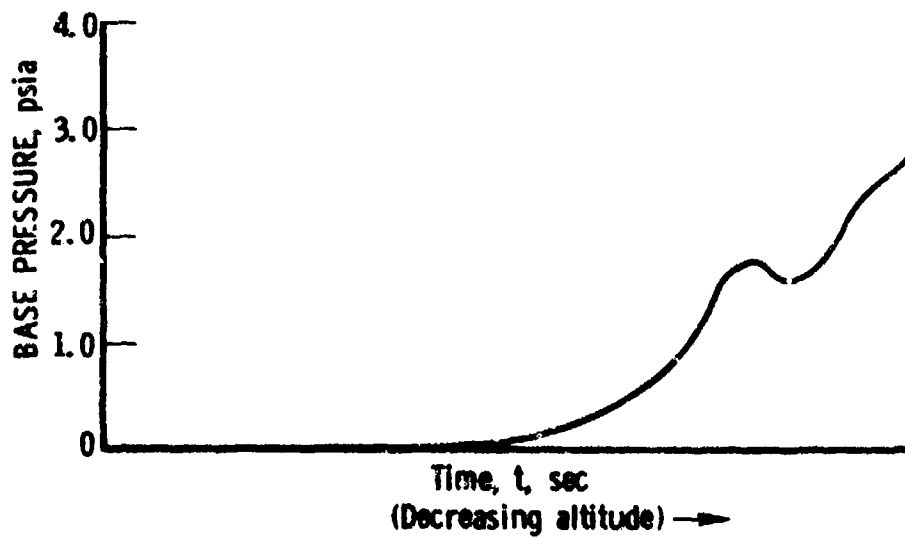


Figure 3-21. Low Range Base Pressure Data

4. AERODYNAMIC / FLIGHT MECHANIC DATA

4.1 INTRODUCTION

This section of the paper will deal with the RV performance parameters that are described from the raw flight data discussed in Section 3. Specifically, the following performance parameters will be discussed:

- a. Drag characteristics (total and components)
- b. Roll performance
- c. Angle of attack/trims
- d. Normal force and pitching moment coefficients
- e. Stability
- f. Axial and lateral loads
- g. Transition onset altitude

4.2 DRAG

The total drag of an RV is made up of three components: the inviscid forebody drag, the base drag, and the viscous drag (Figure 4-1). It is important to measure the total drag (with accelerometers) and the drag components (with pressure sensors)⁽³²⁾ so that analytical prediction techniques or models can be validated for extrapolation to design flight conditions not occurring during the flight program.

Drag is used for reentry trajectory predictions as well as for targeting and accuracy analyses.

The forebody and base drag components are obtained by integrating the flight test pressure distribution data for a given altitude as shown in Figure 4-2. This procedure is then repeated at several altitudes to obtain a history. Figure 4-3 shows the end product: the total drag, the forebody drag, and the base drag histories for a typical RV flight test.

4.3 ROLL PERFORMANCE

It is important to be able to determine the roll performance of an RV so that a statistical data base can be established for the class of heatshield for modeling purposes. It has been established that roll torque on an RV is a strong function of heatshield tape-lap splice orientation. If the heatshield tape laps are all in one direction (++), the RV will tend to spin up in that direction. Conversely, if part of the RV heatshield is ++ and part is not, the vehicle will have a lower spin rate. Figure 4-4 shows typical roll rate flight data for RVs with different heatshield constructions. It is important to control the roll rate within an optimized corridor for an RV via passive means. Too high a roll rate will cause the vehicle to encounter roll resonance with a resulting angle-of-attack divergence, high lateral loads, and a range shortening and/or a decrease in accuracy.

Too low a roll rate may cause the vehicle to spin through zero, which produces unacceptable targeting errors. Accordingly, it is important to measure the roll rate for each flight and reduce the data to coefficient form (C_{l_0} , roll torque coefficient) for phenomenology studies for extrapolation to any $V-\gamma$ flight condition. Figure 4-5 shows the nondimensionalized roll torque coefficient for several flight tests. Roll rate and roll torque coefficients can also be obtained from magnetometer data and will be discussed in a subsequent section.

4.4 ANGLE OF ATTACK/TRIMS

The angle of attack or angle of trim can be obtained in two ways. The simplest technique is to utilize the resultant lateral g's in conjunction with the predicted dynamic pressure and the normal coefficient slope. This technique assumes linear aerodynamic coefficient and represents a fairly

good approximation to the angle-of-attack history. The total angle-of-attack history for a typical reentry vehicle is presented in Figure 4-6. Note that there are two time periods of interest. Time t_1 corresponds with transition onset; the RV can be seen to diverge slightly, and then reconverge. This is the expected trend because this phenomena is experienced by all RVs. The vehicle then damps down to low values of γ and continues at low level until time t_2 when a slight undamping occurs with a subsequent divergence and then reconvergence. The vehicle then again damps down to a low angle of attack. This undamping at time t_2 is also normal and coincides with nosetip shape due to nosetip transition.

Trim angle of attack is derived by fairing a best fit line through the raw lateral accelerometer data and applying the same equation. The amount of trim an RV experience is a strong function of nosetip performance and nosetip assymetries. Trims are important since large trims both can produce trajectory errors and introduce targeting and accuracy errors.

A second technique to determine the angle-of-attack history is to integrate the rate gyro data and use the accelerometer data for boundary conditions in the equation of motion. However, this time consuming and expensive technique is currently used only when an accelerometer-derived data point requires validation or when the complete aerodynamic characteristics are known.

4.5 $C_{m\dot{\gamma}}$ STABILITY PARAMETER AND CENTER OF PRESSURE

The pitching moment coefficient slope $C_{m\dot{\gamma}}$ is an important parameter from which to derive flight test motion data because it provides a measure of the static margin of the RV during reentry. Two techniques are available to derive $C_{m\dot{\gamma}}$. The quickest technique involves use of the pitch and yaw rate gyro data for analog plots. The predominant frequency is determined for specific altitude regimes. The stability parameter $C_{m\dot{\gamma}}$ is a function of the pitch/yaw rate frequency, roll rate, and the inertia of the RV. This technique is quick, and results can be obtained a few hours after the flight.

A more sophisticated technique involves use of petal plots that entail plotting the pitch rate versus the yaw rate for specific altitude regimes. Figure 4-7 presents a petal plot for a typical flight test. The intersection of a line from the origin to the edge of the ellipse represents the $C_{m\dot{\gamma}}$ value. This technique is time consuming but is inherently more accurate when used in a stability or center of pressure (X_{cp}) assessment. Figure 4-8 presents a comparison of the $C_{m\dot{\gamma}}$ from a typical flight as derived from frequency and petal plot techniques.

The ultimate use of $C_{m\dot{\gamma}}$ is for a derivation of the static margin or center of pressure location at specific points along the reentry trajectory. Figure 4-9 presents a schematic showing the relative locations of the center of gravity (CG) and X_{cp} . For adequate vehicle performance, the CG of the RV must be forward of the X_{cp} for the entire trajectory or the RV will become unstable. It is imperative that the X_{cp} or the static margin (SM) be assessed for the RV flight program.

4.6 NORMAL FORCE AND PITCHING MOMENT COEFFICIENT

It is imperative that the basic aerodynamic characteristics (drag, stability, normal force, and pitching moment coefficients) be derived from flight data in order to validate modeling techniques that accurately predict the vehicle trajectory parameters. Drag and stability have been discussed previously. This subsection will deal with the normal force and pitching moment coefficients as a function of angle of attack. There are basically three steps involved in these microscopic analyses. First, specific altitude regimes of interest are selected where there are sufficient motion oscillations for the techniques to be valid. The angle-of-attack history is then derived by integrating the pitch/yaw rate gyro data as described in subsection 4.5. Figure 4-10 shows typical results. The second step is to determine a history of the normal force coefficient directly from the lateral accelerometer data (G_n).

Figure 4-11 presents the time histories of the normal force and pitching moment coefficients versus time. The third step is to cross-plot these results with the angle-of-attack history to obtain the final aerodynamics (pitch angle-of-attack history) shown in Figure 4-12. This technique also provides a bonus since the slope of the data (see dashed lines) will yield additional independent data to confirm the stability and center of pressure.

4.7 AXIAL AND LATERAL LOADS

The axial and lateral loads experienced are rather straightforward and merely require patching together the various range sensors and applying the proper corrections for CG offset. Figure 4-13 presents a typical axial and lateral load history.

Magnetometers can be utilized to measure both the roll rate of an RV and the RV state vector relative to the earth. Roll rate can be measured with gyros; however, only the magnetometer can provide the direction of the body axis and vehicle orientation in inertial space. These data are used when microscopic analyses are performed for detailed trajectory reconstruction to support accuracy and modeling assessments. Figure 4-14 presents typical magnetometer data.

4.8 CONCLUSIONS/FLIGHT DYNAMIC INSTRUMENTATION TRENDS

The detailed on-board flight instrumentation required for typical reentry vehicles have been described. Several types of flight measurement have been discussed to derive the same parameter. The purpose of this paper has been to disseminate typical flight test data, to illustrate what the data are used for, and to suggest trends for future RVs. The basic aerodynamic characteristics of an RV are:

- a. Drag
- b. Normal force and pitching moment coefficients
- c. Roll rate
- d. Angle-of-attack characteristics

The foregoing characteristics can be obtained with a full complement of accelerometers, rate gyros, pressure sensors, and magnetometers. The basic task of the flight test engineer is to utilize the most cost-effective instrumentation consistent with the mission requirements. The following guidelines represent recommended procedures for both RV technology flight programs.

It has been shown that the vernier step force balance accelerometer is far superior to the displacement pot-type accelerometer in terms of both accuracy and resolution; therefore, it is the recommended type.

The dual-range, force balance lateral accelerometer is superior to overlapping ranges of displacement pot-type accelerometers.

Low-range pressure measurements ($P < 1.0$ pica) are best made with capacitance-type sensors. High-range pressure measurements ($P = 5$ to 100 psia) are best made with solid state, strain gage sensors. The standard rate gyro is sufficient in its present form.

Roll rate can be obtained from a gyro or a magnetometer. It is recommended that the magnetometer be utilized on research flight programs as it provides both roll rate and the altitude of the RV in inertial space relative to the earth for detailed trajectory reconstruction and accuracy studies. However, the standard roll rate gyro would be more cost effective for standard flights.

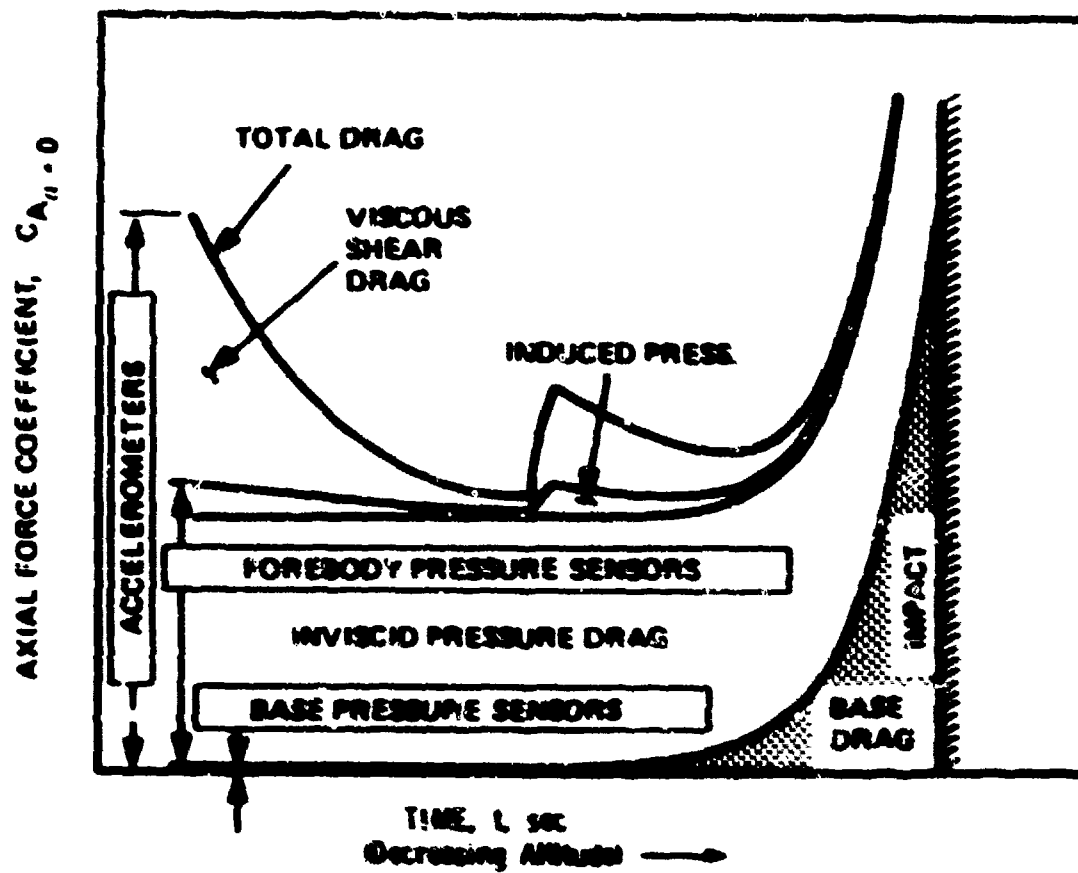
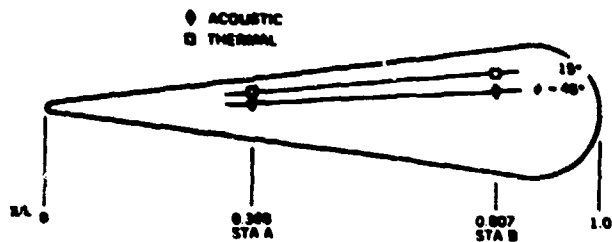
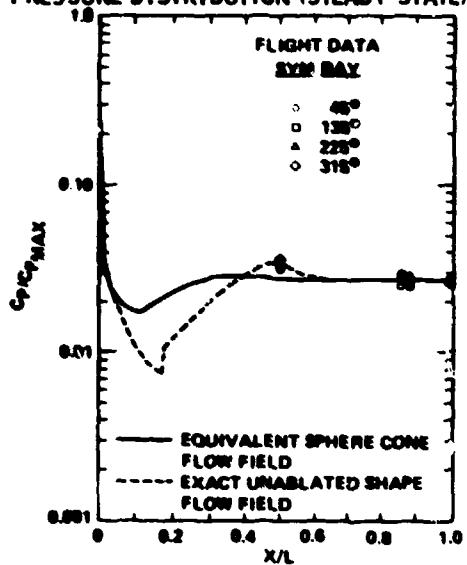


Figure 4-1. Typical Drag Component Buildup



TYPICAL FOREBODY AXIAL
PRESSURE DISTRIBUTION (STEADY STATE)



DOME SHOULDER FLIGHT TEST DATA

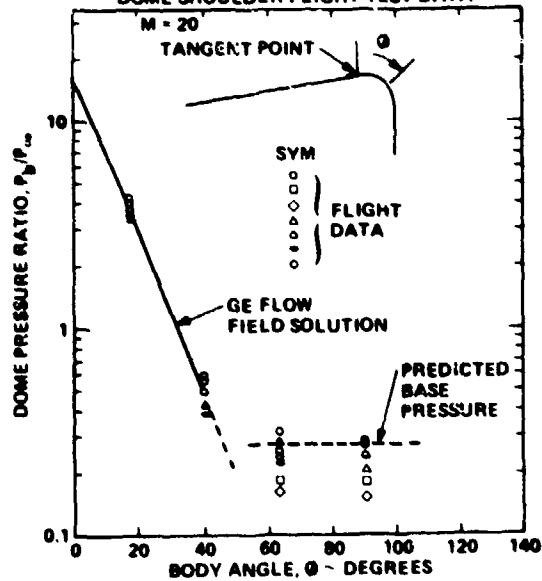


Figure 4-2. Flight Test Pressure Data

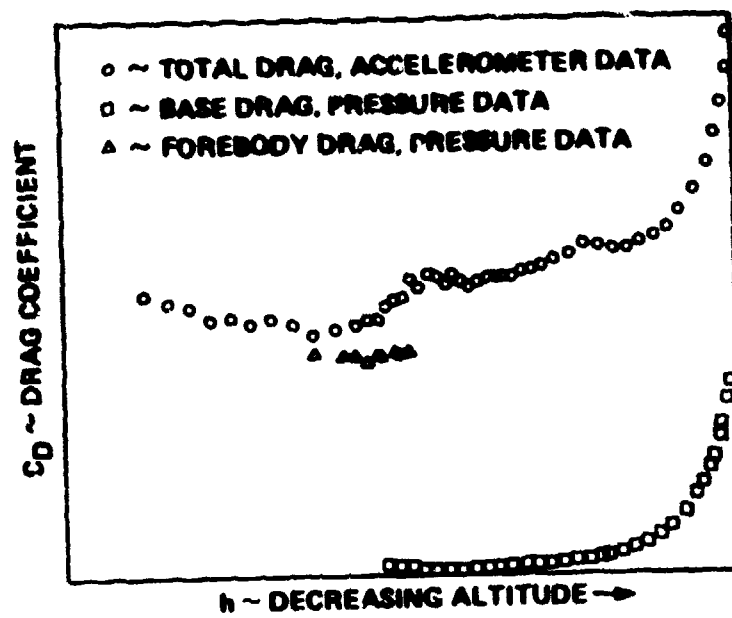


Figure 4-3. Typical Flight Test Data -
 Measured Drag Components
 vs Altitude

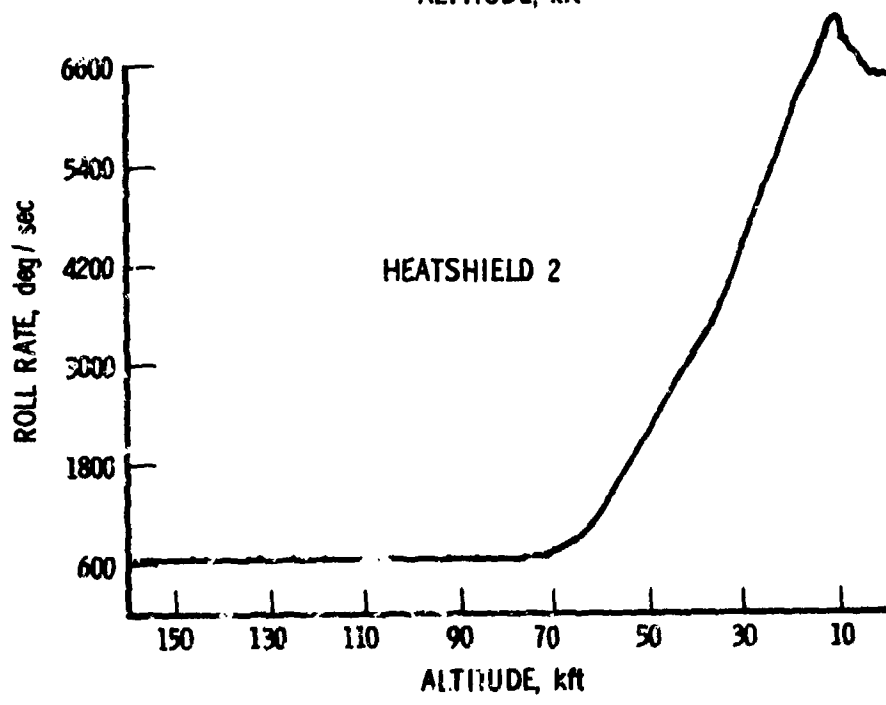
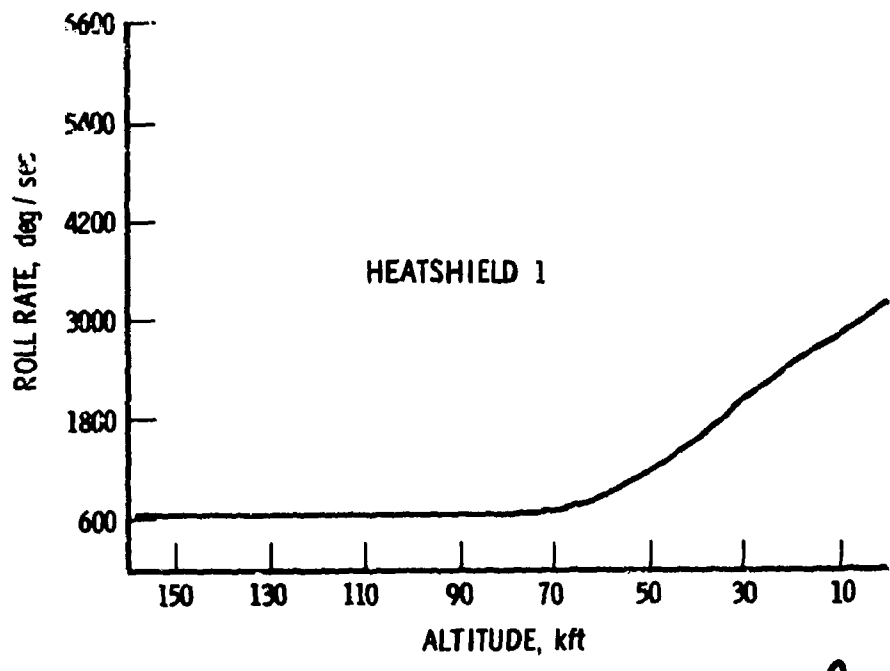


Figure 4-4. Roll Rate vs Heatshield Type and Altitude

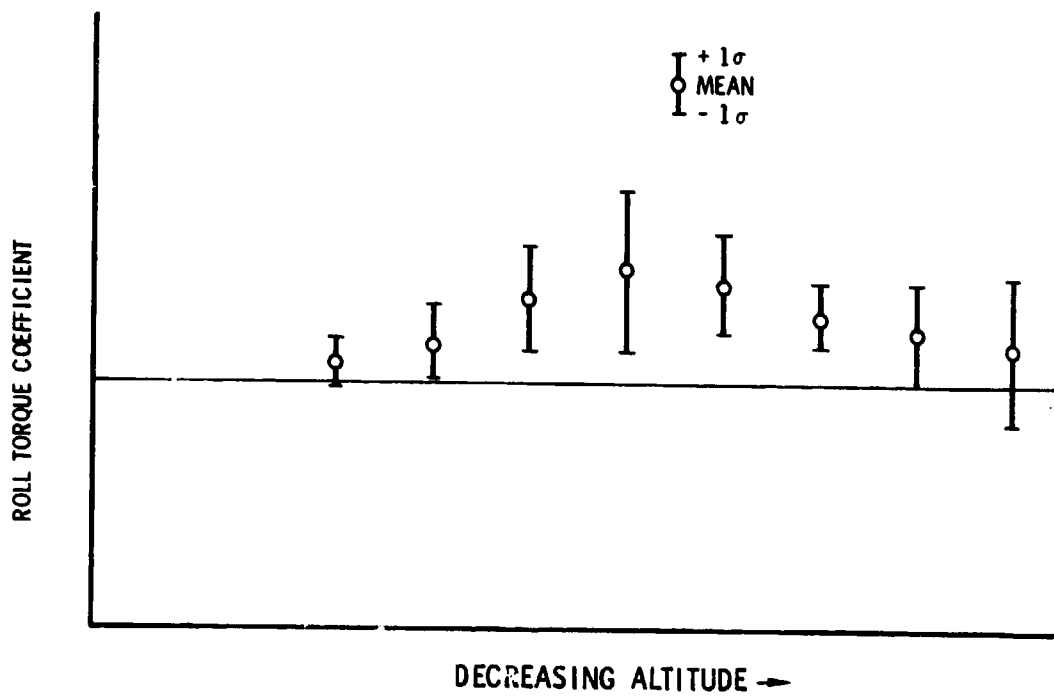


Figure 4-5. Early Buy Roll Torque Statistics

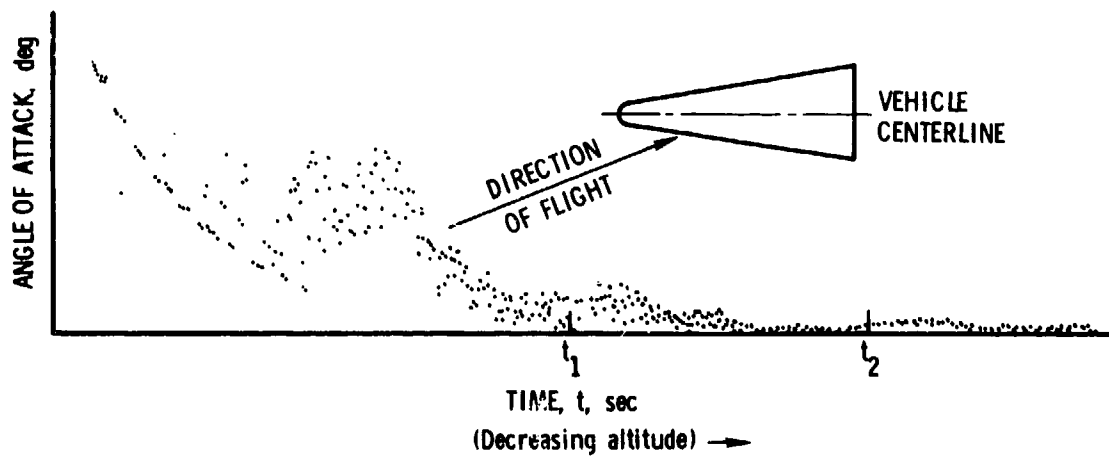


Figure 4-6. Total Angle-of-Attack History

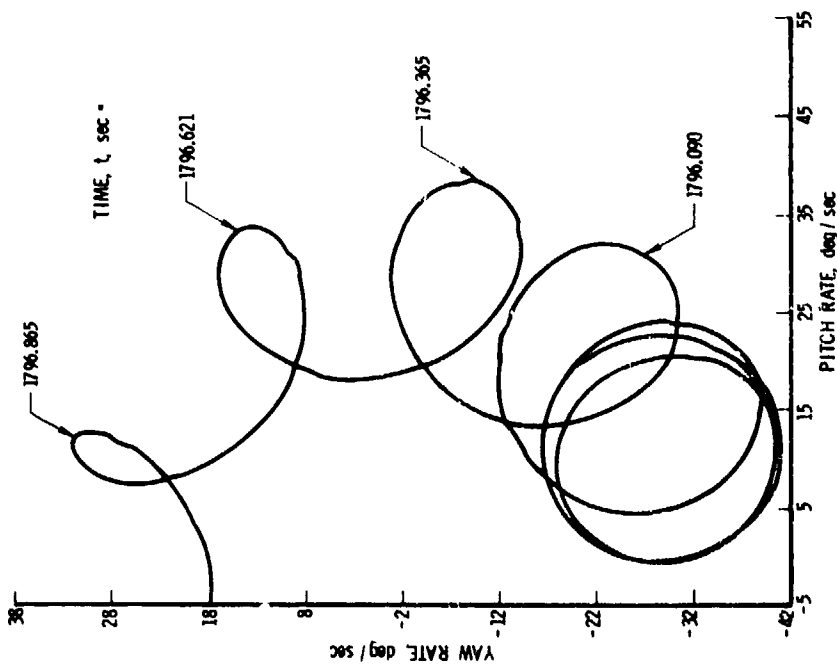


Figure 4-7. Petal Plot for a Typical Flight Test

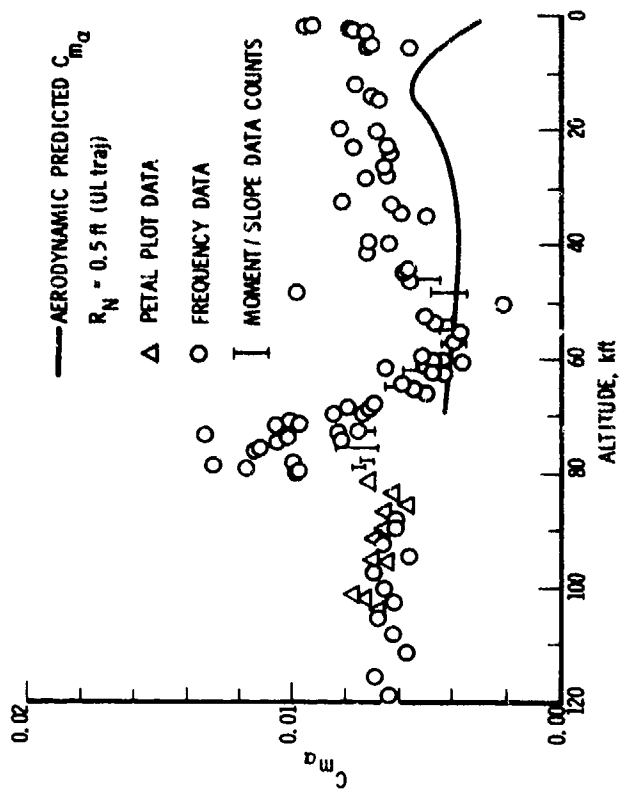


Figure 4-8. C_{m_c} vs Altitude

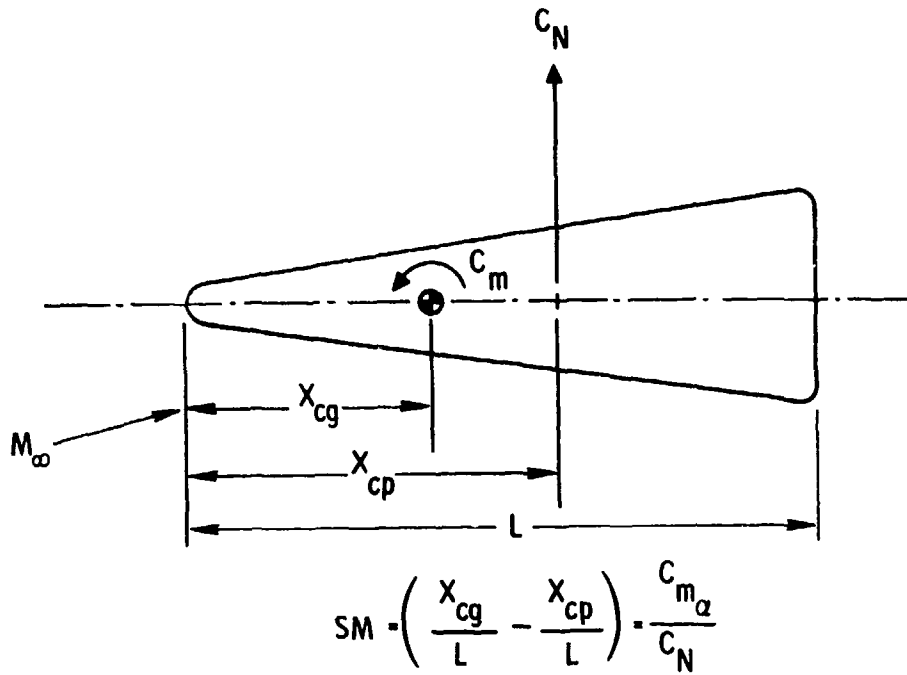


Figure 4-9. Vehicle Dynamic Schematic

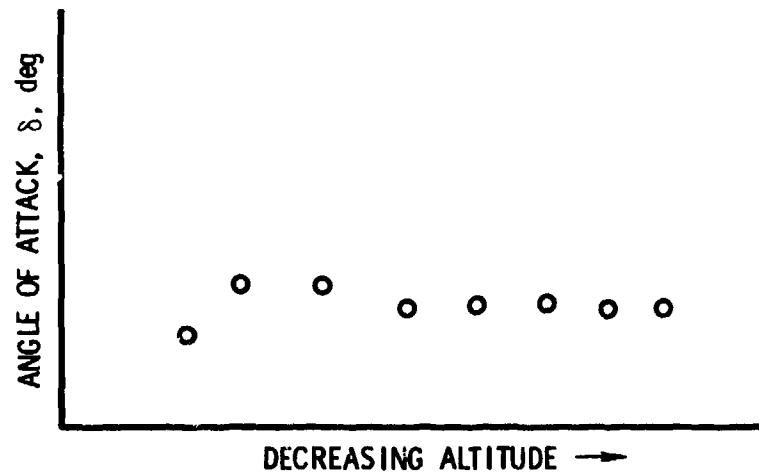


Figure 4-10. Nominal Angle-of-Attack History

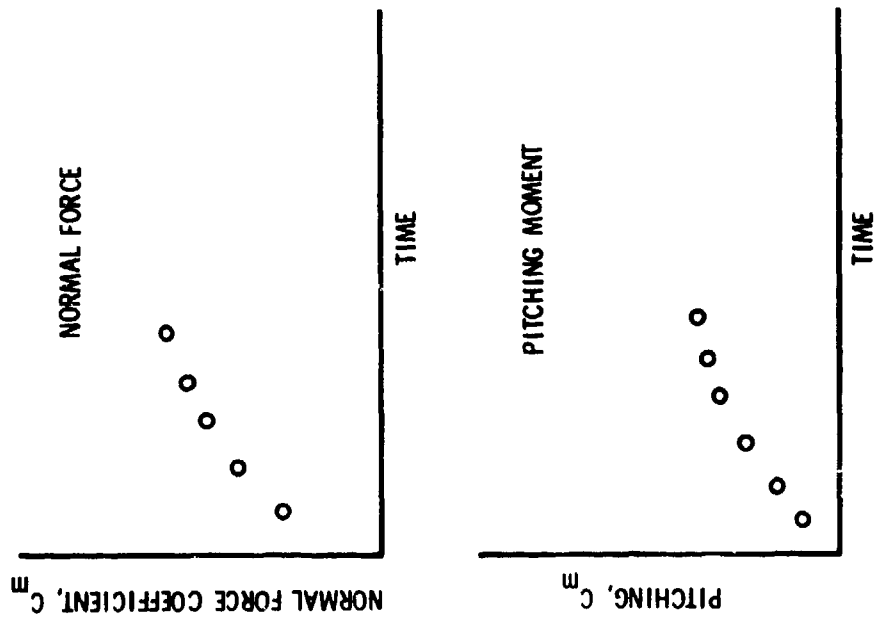


Figure 4-11. Normal Force and Pitching Moment Histories

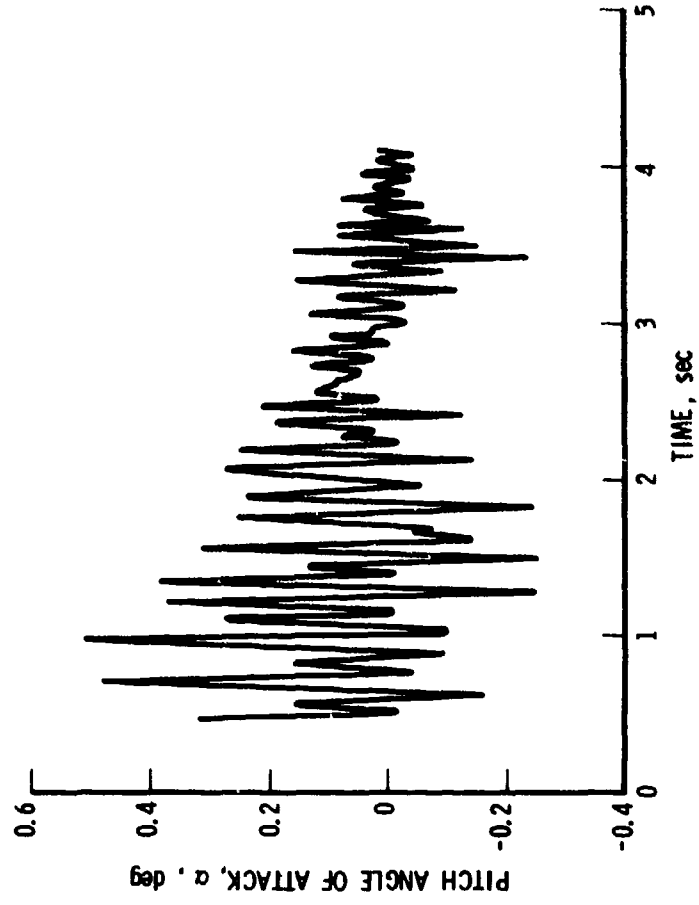


Figure 4-12. Flight Test Analysis (Angle-of-Attack Reconstruction)

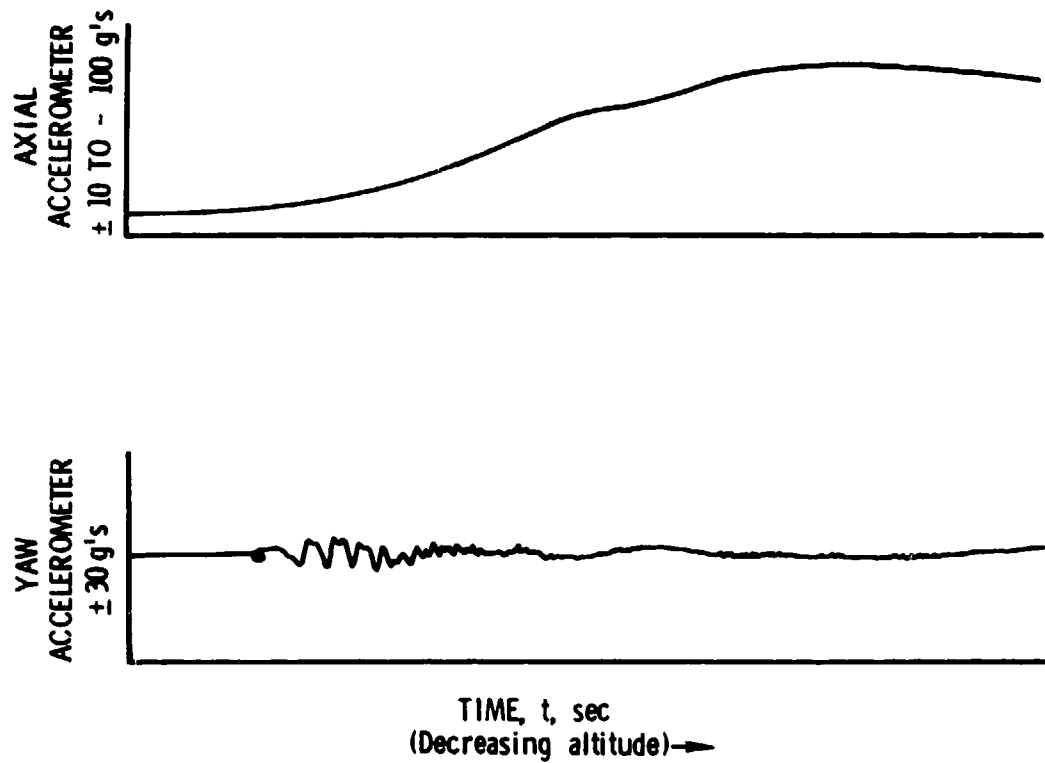


Figure 4-13. Typical Axial and Lateral Load Histories

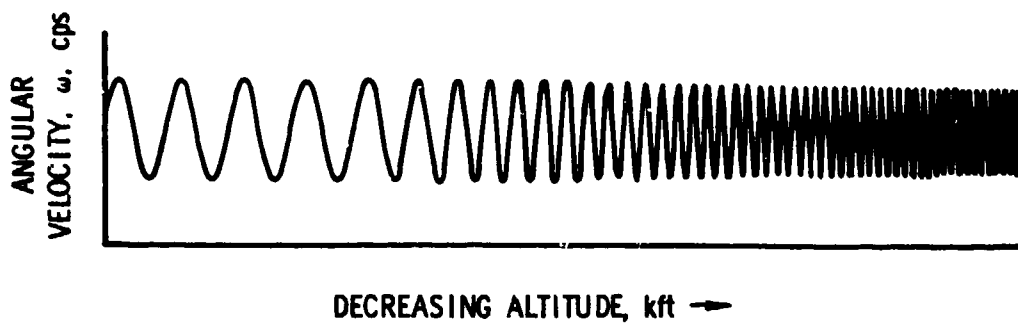


Figure 4-14. Magnetometer Data

5. FLUID DYNAMIC MEASUREMENTS

5.1 GENERAL

Fluid dynamic measurements consist of local flow field measurements near the nosetip and on the frustum and base of an RV.

The basic fluid dynamic measurements consist of:

- a. Heat transfer rate
- b. Pressure (steady state)
- c. Acoustic environment (fluctuating pressures)
- d. Boundary layer transition (inferred from above)

The purpose of the measurements is essentially the same for the previously discussed technologies; i. e., obtain in-flight measurements to determine performance parameters to verify RV prediction, modeling, and design techniques.

Since the measurement of interest is the local flow field at the surface of the vehicle, it is important that the sensor not disturb the flow field. The ideal sensor is one that would require no penetration of the surface of the heatshield. Attempts to correlate subsurface temperature measurements with surface and boundary layer phenomena have shown them to have too great a time lag for useful data, and heat transfer measurements require penetration of the heatshield. Fluctuating pressure measurements can be made with either ported or nonported gages, as discussed later. Ground tests and flight results show that holes less than ~ 0.050 -in. diameter do not affect transition, and ported gages can stay within this limitation. Although the thermal gages fill the holes in which they are installed, they do present a discontinuity at the surface. The gage and its installation must be designed to minimize the disturbance. Flight results indicate that the flow field is not disturbed sufficiently to trip boundary layer transition.

5.2 HEAT TRANSFER MEASUREMENTS

Heat transfer measurements are made with either slug (integrating) calorimeters or heating rate (differential) calorimeters. Photographs of the differential-type sensors are shown in Figures 5-1 and 5-2. The basic purpose of these measurements is to obtain the change in heating rate associated with the onset of boundary layer transition from laminar to turbulent flow. Both slug and rate calorimeters are mounted flush with the surface of the heatshield. Slug calorimeters consist simply of a copper mass with a thermocouple to measure its temperature rise (ΔT). Neglecting losses, the rise in temperature is proportional to the integrated heat input, and a change in the rate of heat input is detected by a change in the rate of rise.

Two types of rate calorimeters are in general use. The first is a Gardon type, manufactured by Hycal Engineering as their asymptotic calorimeter. As shown in the cross section of Figure 5-3, the Hycal calorimeters consist basically of a thin metallic foil of constantan, bonded on the edges of a cavity in a heat sink of copper. A fine copper wire is bonded metallurgically to the center of the foil. Heat flows into the surface of the foil and then radially into the heat sink. The radial heat flow establishes a radial temperature gradient, which is measured by the differential copper-constantan-copper thermocouple. It can be shown that $q \sim \Delta T \sim \Delta V$, so that the output voltage varies with the rate of heat flow rate (q). A typical installation is shown in Figure 5-4.

The second type of rate calorimeter is the ΔT gage. As shown in the cross section of Figure 5-5, heat flowing into the outer surface of the gage establishes an axial heat flow with a resultant axial temperature gradient. Two constantan wires, spaced axially, generate a voltage proportional to the axial heat flow. Again, it can be shown that $q/A \sim K\Delta T \sim \Delta V$, so that, as with the Gardon gage, the output voltage varies with the heat flow rate (q/A). For information, Figure 5-6 shows a photograph of the internal portion of an RV with rate calorimeters installed.

Several flight measurements have been made in which the two types of rate calorimeters were flown "side by side" to compare performance. The flight results indicated that the two sensors tracked each other, responding to changes in heat input due to variations in vehicle motion, and detected the onset of boundary layer transition. Analog traces of typical flight data for both sensors are shown on Figure 5-7. The two sensors were at the same body station and within 10° of each other. Figure 5-8 shows the progression of transition from aft to forward on a typical flight using the ΔT sensor. Subsequent flights have further demonstrated that the progression is from aft to forward, that the rate of progression varies, and that it can be asymmetric.

5.3 STEADY STATE PRESSURE MEASUREMENTS

Steady state pressure measurements have been discussed previously in the aerodynamics section. It was shown that local in-flight pressure measurements (steady state) with a pressure port through the heatshield connected to sensors within the RV were utilized to verify forebody and base flow field prediction techniques. These flight data could be integrated to obtain the forebody and base drag components of total drag as discussed in subsection 4.2.

In addition, base pressure measurements could also be utilized to determine onset of boundary layer transition at the aft end of the frustum. The above steady state pressure measurements can be made with relatively low-frequency response pressure sensors (rise time < 30 msec) and sampling rates as low as 10 to 20 samples/sec.

5.4 ACOUSTIC MEASUREMENTS

Acoustic measurements are made for two basic purposes. First, to determine acoustic overall sound pressure level (OASPL) due to fluctuating/pressure, which emanates from the boundary layer during transitional and turbulent flow, for structural analyses. Second, acoustic measurements are an excellent indicator of onset of boundary layer transition, transition

progression, and symmetry and have been found to correlate with thermal indications of transition onset. In addition, acoustic sensors can be utilized to determine the "end" of transition and, hence, the start of fully turbulent flow. It is this application of transition detection that will be discussed in detail.

Acoustic measurements for transition detection can be made via two techniques: a ported acoustic sensor or the nonported sensor. Both sensors have various advantages and disadvantages depending upon mission objectives. The operating principle of both sensors, along with photographs and typical flight data, will be shown.

5.4.1 Ported Sensor

Ported acoustic sensors have been flown on RVs^(24, 27) for the past decade and have obtained valuable flight data pertinent to the boundary layer state. It has been demonstrated in wind tunnel tests that ported acoustic sensors, which measure fluctuating pressures, reach a maximum as the transition front passes over the port as illustrated in Figure 5-9.

Flight acoustic sensors generally have utilized the piezoelectric principle that measures rate of change of pressure. The pressure port geometry (port diameter and length) is generally a tradeoff between frequency response, temperature limitations, and sensor and port erosion effects. It has generally been found that a port diameter of ~ 0.040 in. precludes erosion effects and a port passage length of ~ 0.135 in. provides a frequency response up to approximately 20 kHz.

A typical port geometry flown on an early RV with a piezoelectric acoustic sensor is shown in Figure 5-10 along with the RV configuration. A photograph of the acoustic sensor and its signal conditioner is shown in Figure 5-11. Typical raw flight test data during transition shows a buildup in boundary layer noise level (Figure 5-12). Reduced flight data in the form of sound pressure level (dB) as a function of time is presented in Figure 5-13. These flight data show that transition onset starts at the aft end of the RV

and progresses forward as expected. Additional flight acoustic data using the same port geometry and sensor on a later flight program are presented in Figure 5-14. The data can be seen to maximize at ~ 2.0 sec and indicate transition onset. Reduced flight data for the entire flight indicate transition onset and a turbulent flow OASPL of ~ 150 dB (Figure 5-15). Piezoelectric sensors have provided good data in the past; however, these types of sensors require a separate signal conditioner, and the sensor measures fluctuating pressures only.

A more recent development to measure fluctuating pressure is to utilize a miniaturized solid state strain gage sensor. This sensor has the advantage of being extremely small (see Figure 5-16 for sensing element) and, therefore, can be mounted in many configurations (e.g., a screw thread) directly to the heatshield/structure. The sensor can measure both steady state and fluctuating pressures. Figure 5-17 shows a photograph of a miniaturized integrated pressure transducer with a self-contained signal conditioner all packaged in a compact unit. This unit was recently flown and successfully measured fluctuating pressures (to determine transition onset) and steady state pressures (to determine the static pressure level) simultaneously. The installation drawing for the sensor is shown in Figure 5-18. The recent flight previously mentioned had two sensors located on the forward and aft section of the RV to determine the rate of transition progression. Figure 5-19 shows a schematic of the sensor locations, sensor installation/port design, and the predicted steady state and fluctuating pressure histories.

For the purpose of completeness, it should be noted that pressure measurements have progressed from two separate bulky sensors and separate ports to measure steady state and fluctuating pressure (10 years ago) to the present design, which utilizes a single miniaturized integrated sensor to measure steady state and fluctuating pressures simultaneously from the same port. Figure 5-20 shows a pictorial overview of this development.

Typical fluctuating pressure data from the ported acoustic sensors are presented in Figure 5-21 for the aft and forward sensors. The data show the expected trend of transition initiation at the aft end and progressing forward. The aft sensor indicates transition onset at $t \sim 0.5$ sec, while the forward sensor indicates transition at $t \sim 3.5$ sec. This time span is consistent with thermal indications. As stated previously, the solid state strain gage sensors can measure steady state and fluctuating pressures simultaneously and are illustrated in Figure 5-22.

5.4.2 Nonported Sensor

The nonported acoustic gage is a recent development called the Boundary Layer Acoustic Monitor (BLAM) gage.³³ This gage has been flight-tested with rate calorimeters for comparison. As shown in Figure 5-23, the sensing element is mounted on the inside of the heatshield and senses the acoustic noise in the flow field by the stress waves transmitted through the heatshield. It achieves the ideal sensor objective of requiring no holes in the heatshields. By good design and choice of frequency, the sensor is made highly directional and has a narrow-band frequency response, with typical results of Figure 5-23. A typical vehicle installation is shown in Figure 5-24; an internal RV, in Figure 5-25.

Due to the wide range of sound pressure levels, the BLAM signal conditioner converted the input signal to a log output signal. As shown in Figure 5-26, the resultant output gave clear indications of the presence of noise bursts well before the rate calorimeters indicated thermal transition. It should be noted on Figure 5-26 that the noise burst occurs out of phase on the two sides of the vehicle. The noise on one side is not detected on the opposite side, indicating clearly the direction sensitivity of the detectors. Careful comparison of the observed peaks in the noise signal with vehicle motion indicated a close correlation with angle-of-attack variations, even though the maximum angle of attack at this time was less than 0.2 deg.

Due to the compression of the log scale, acoustic transition is not easily detectable on Figure 5-26. The same data is shown on Figure 5-27

on a linear output scale. Acoustic transition is indicated clearly, and the sensors indicate that the transition occurs simultaneously on both sides. The thermal transition detectors on this vehicle, however, consistently showed an asymmetric transition. Incidentally, the thermal sensors showed the same correlation with vehicle motion shown by the acoustic sensors. A comparison of the BLAM output for a typical flight shows it does sense transition progression from the aft to forward station as expected (Figure 5-28).

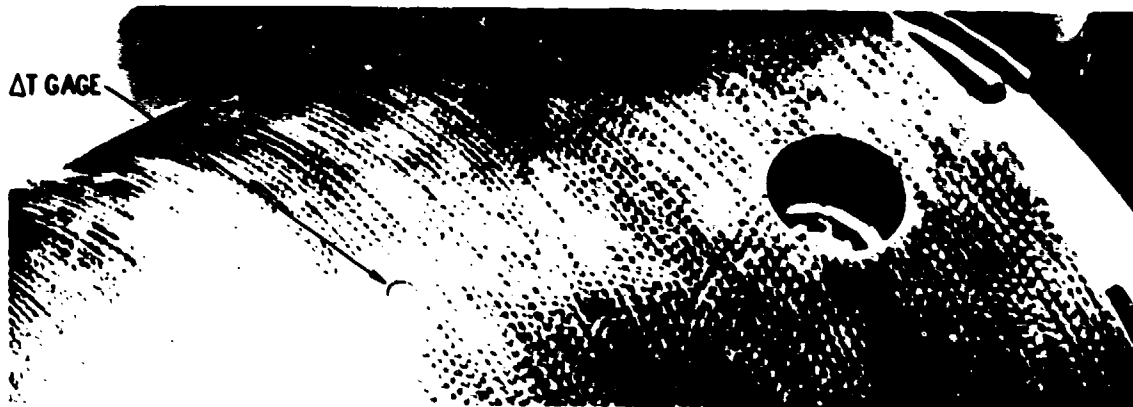


Figure 5-1. Rate (ΔT) Gage Installation in Heatshield

KULLITE
AC52



Figure 5-2. Rate and Integration Calorimeter Gages
Installation in Heatshield

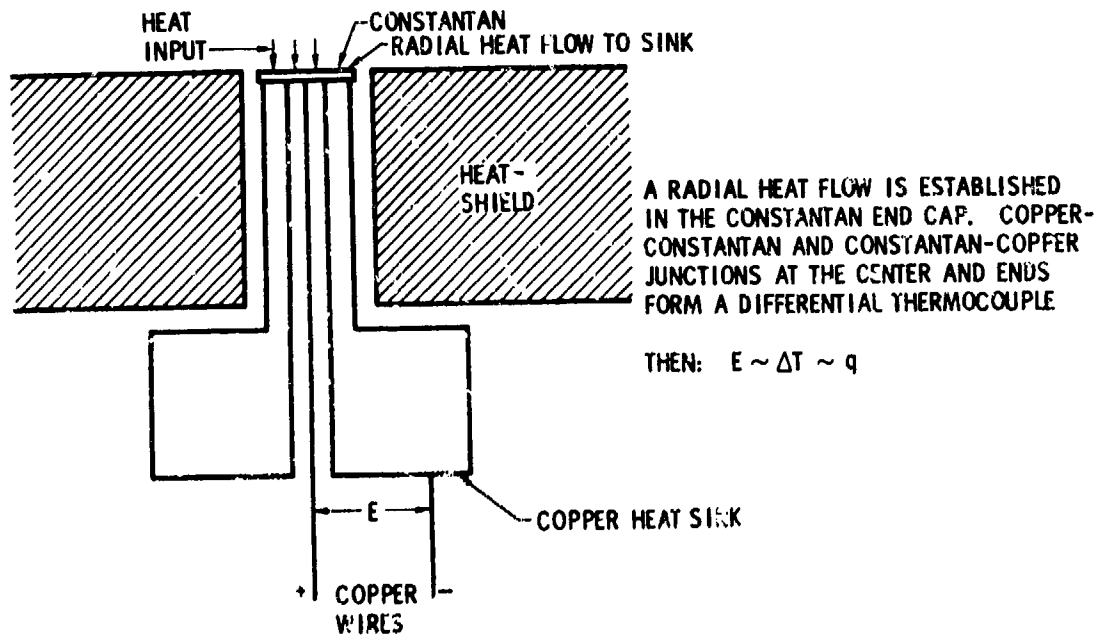


Figure 5-3. Hycal Detector Principle of Operation

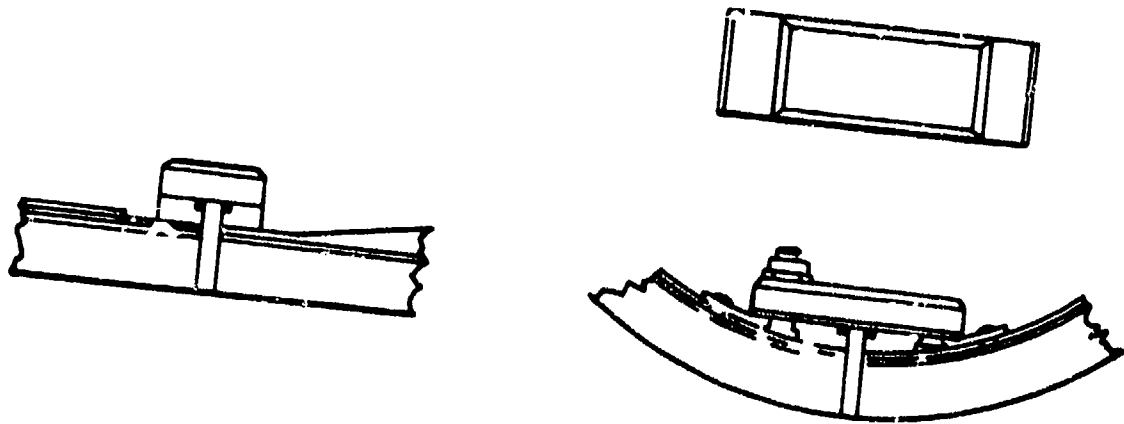
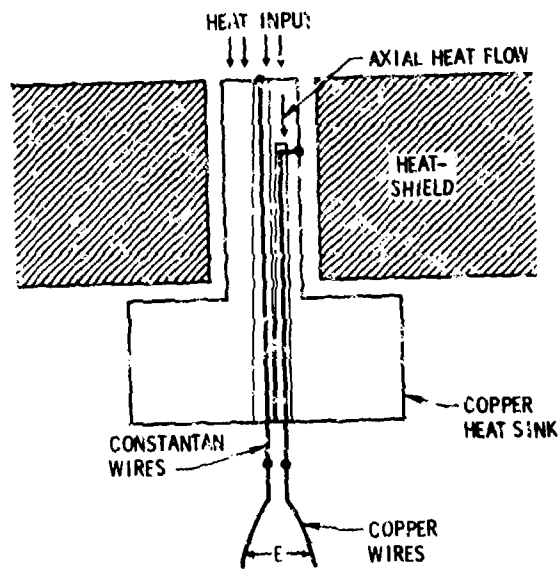


Figure 5-4. Calorimeter



AN AXIAL HEAT FLOW IS ESTABLISHED IN THE COPPER ROD. CONSTANTAN-COPPER AND COPPER-CONSTANTAN JUNCTIONS AT TWO AXIAL LOCATIONS FORM A DIFFERENTIAL THERMOCOUPLE

THEN: $E \sim \Delta T \sim \dot{q}$

Figure 5-5. ΔT Detector Principle of Operation



Figure 5-6. Internal Installation of Calorimeters

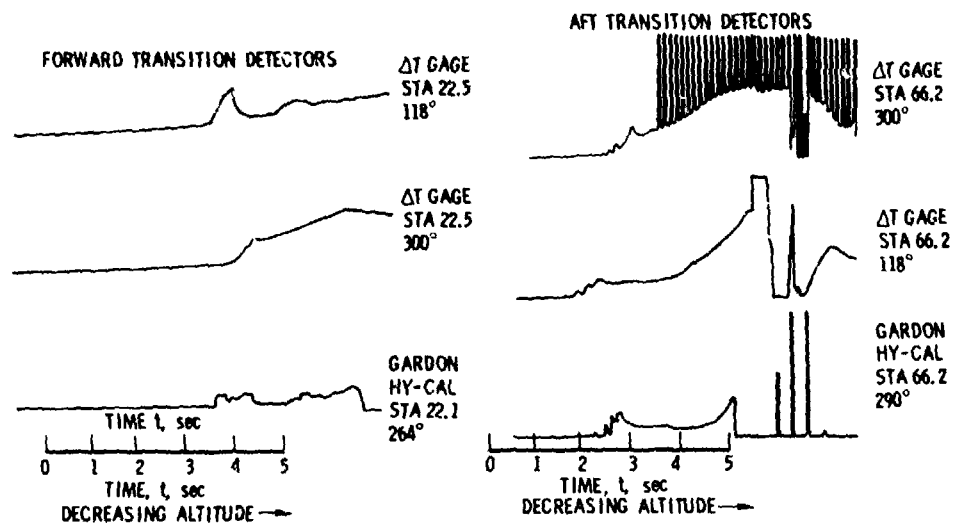


Figure 5-7. Thermal Transition Detectors

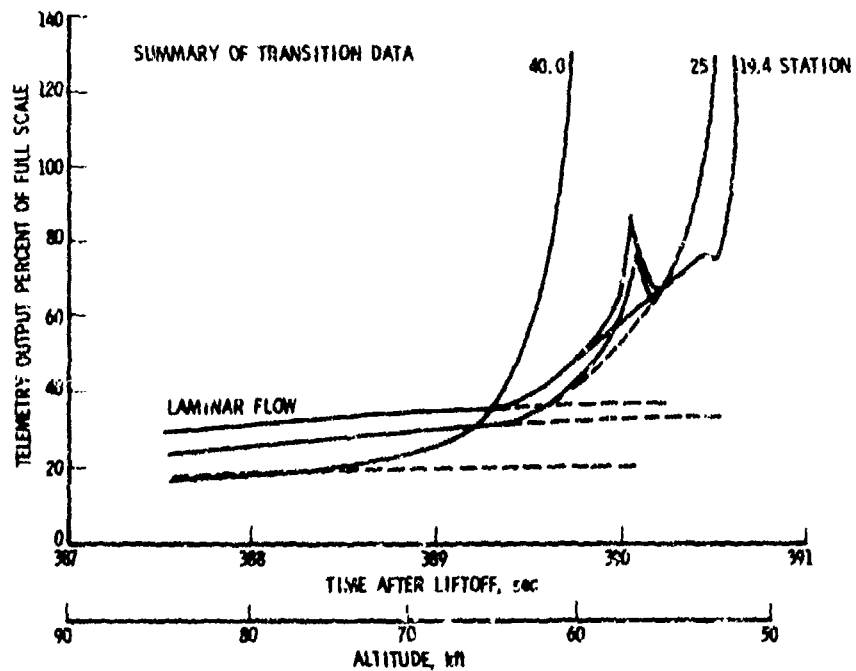


Figure 5-8. Summary of Transition Data

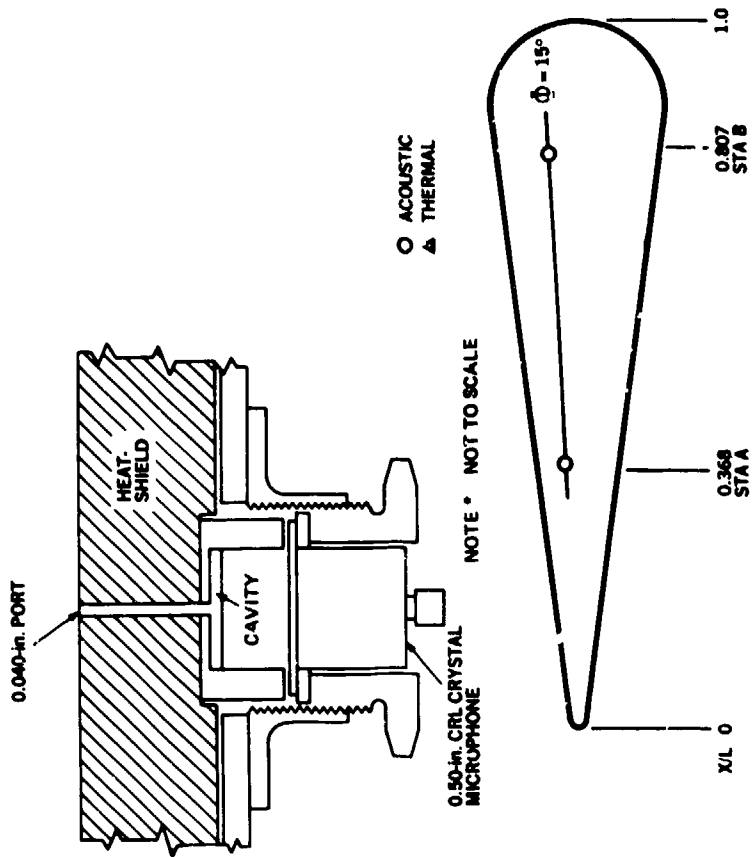


Figure 5-10. Transition Sensor Locations (Flight A)

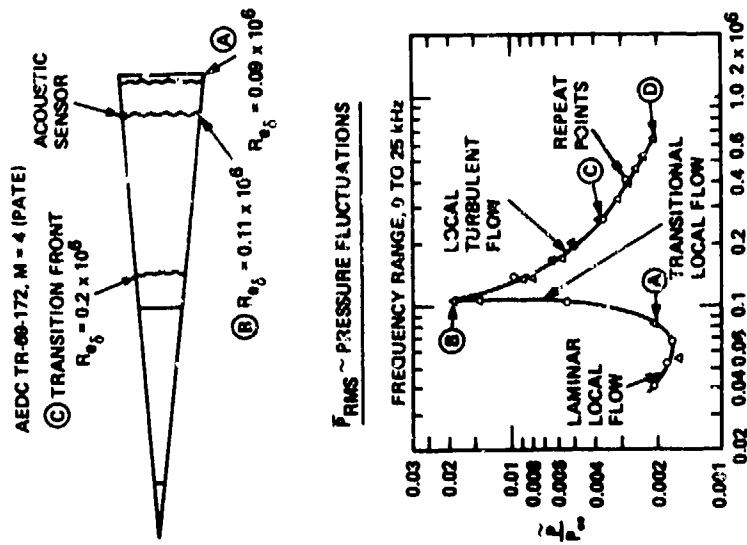


Figure 5-9. Transition Front Progression and Acoustic Sensor Response (Ground Test Data)

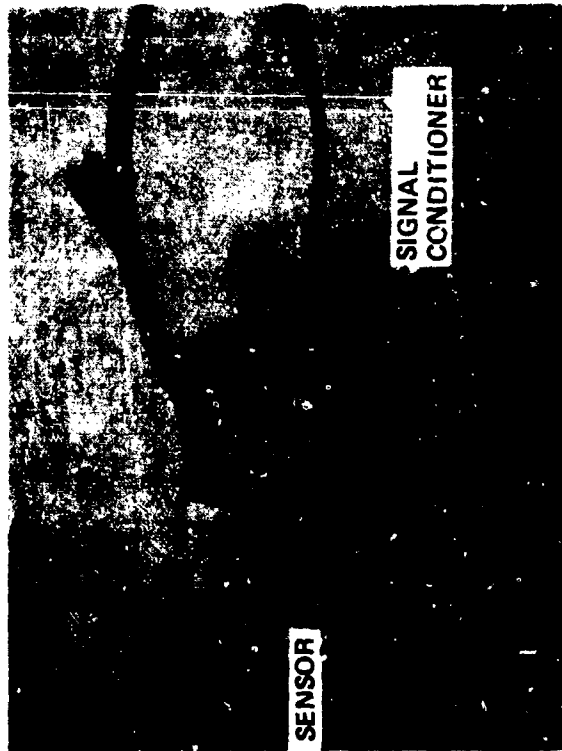


Figure 5-11. Piezoelectric Acoustic Gage for Fluctuating Pressures (Early Generation)

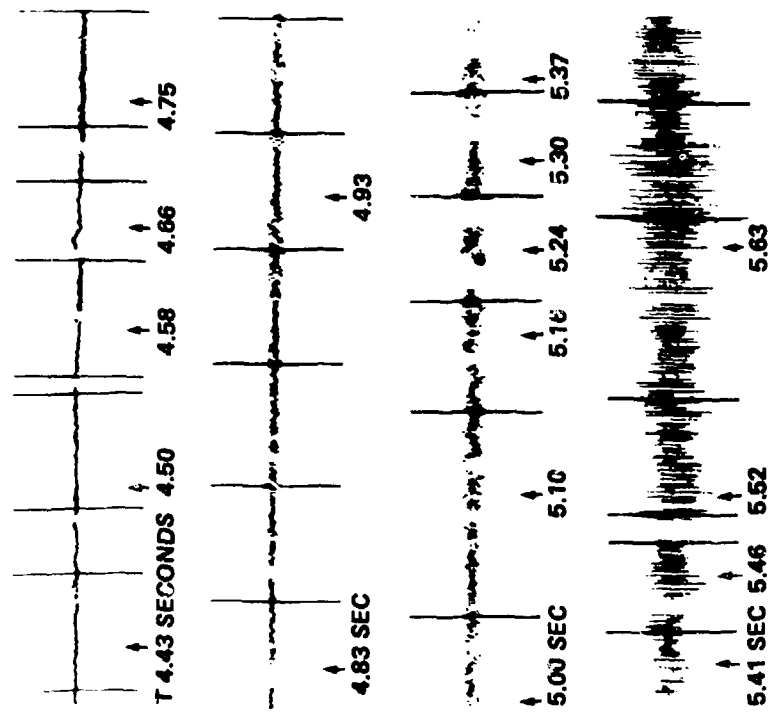


Figure 5-12. Transition Noise (Flight A)

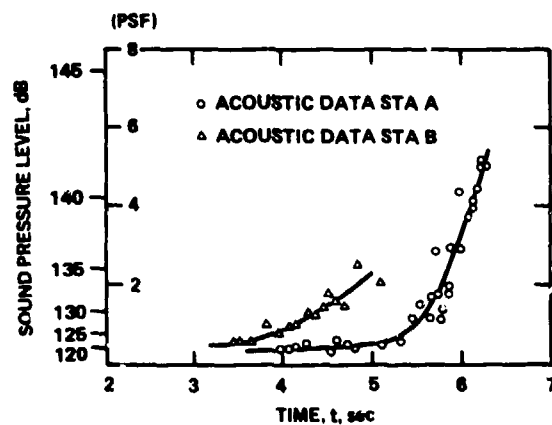
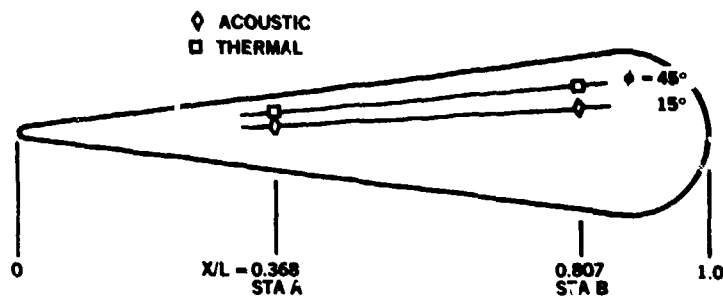


Figure 5-13. Transition Onset From Acoustic Data (Flight A)

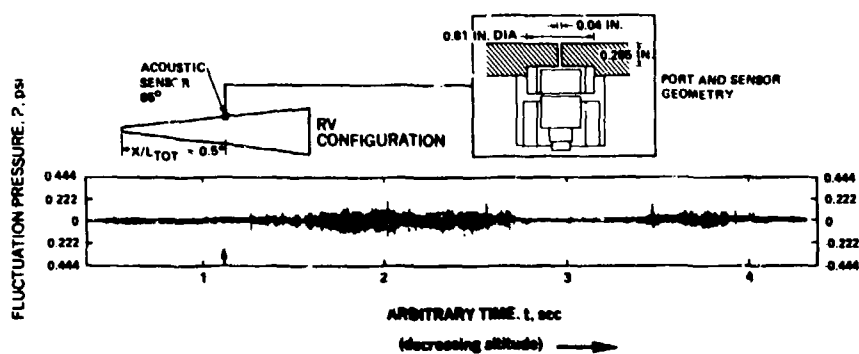


Figure 5-14. Acoustic (Fluctuating Pressure) Flight Data Showing Transition Onset (Flight B)

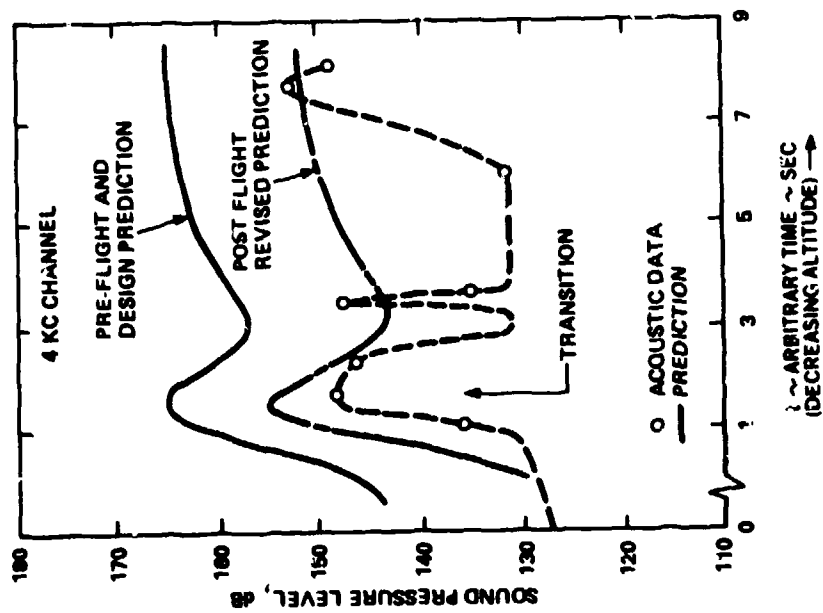


Figure 5-15. Acoustic Flight Data (Flight B)

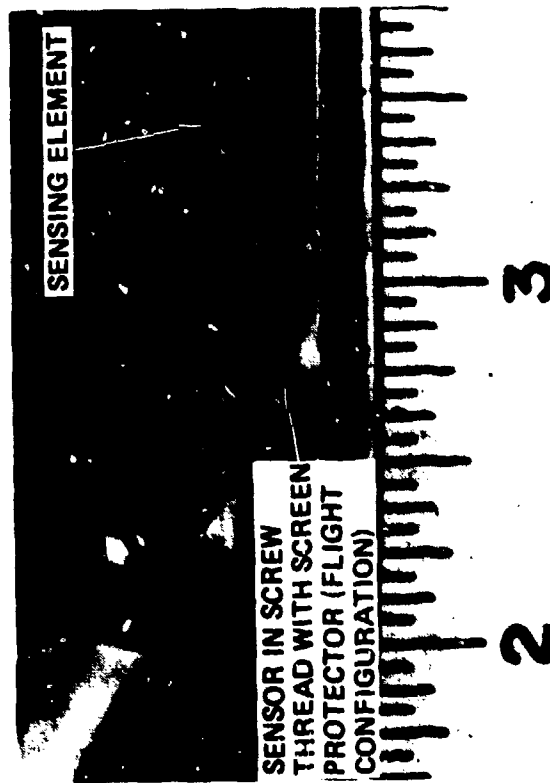


Figure 5-16. Flight Pressure Sensor



Figure 5-17. Present Generation (1976) Miniaturized Integrated Pressure Transducer for Steady-State and Fluctuating (Acoustic) Pressures

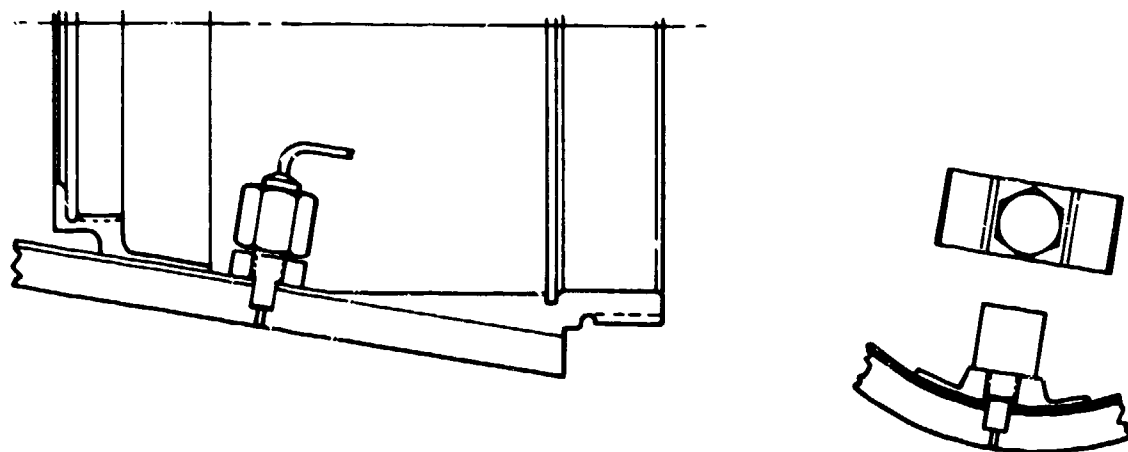


Figure 5-18. Kulite-Ported Acoustic Gage

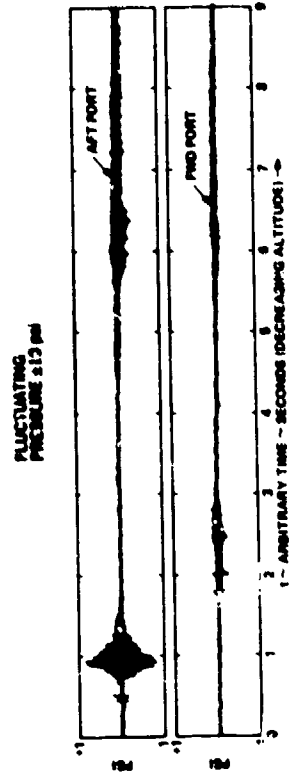
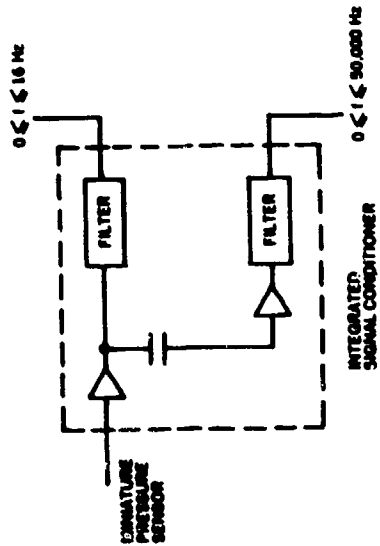
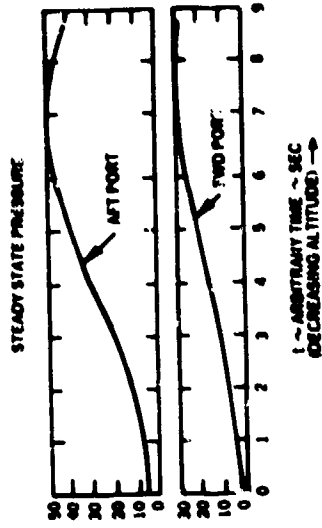
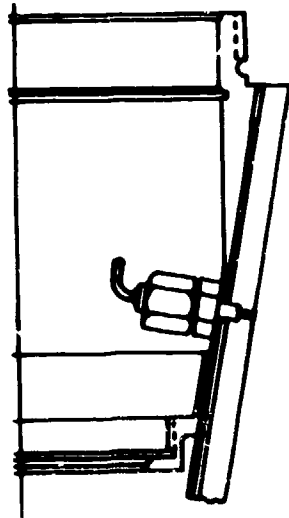
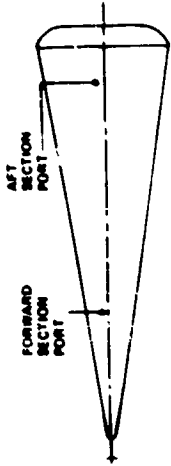


Figure 5-19. Dual-Band Pressure Measurement System for Flight Experiment

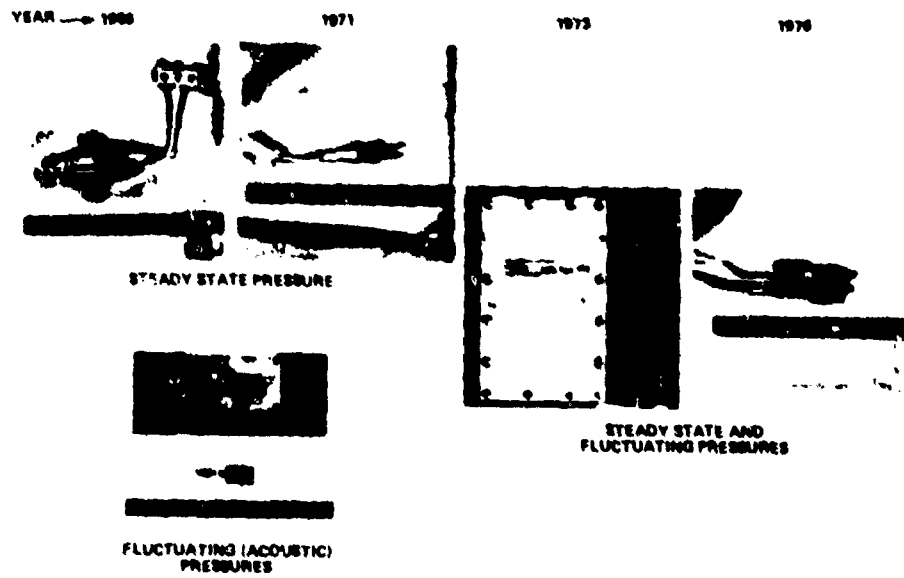


Figure 5-20. RV Flight Test Pressure Sensor Overview History

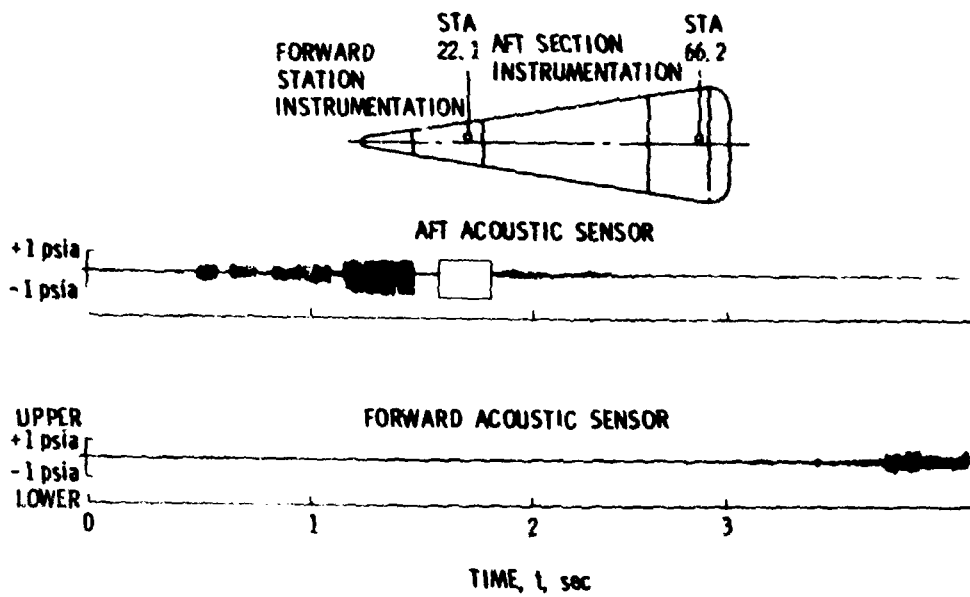


Figure 5-21. Fluctuating Pressure Time Histories

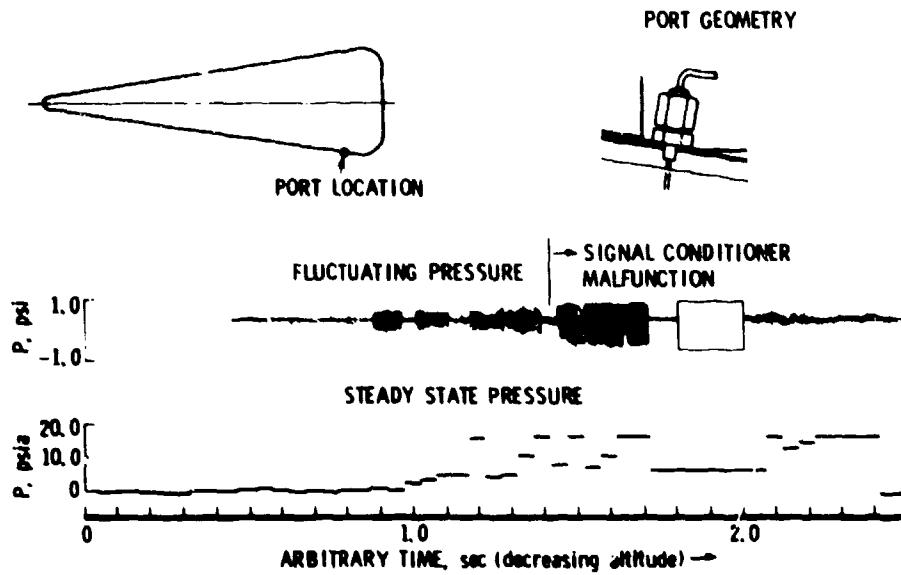


Figure 5-22. Flight Test Data Showing Simultaneous Measurement of Fluctuating and Steady-State Pressure From Same Sensor/Port

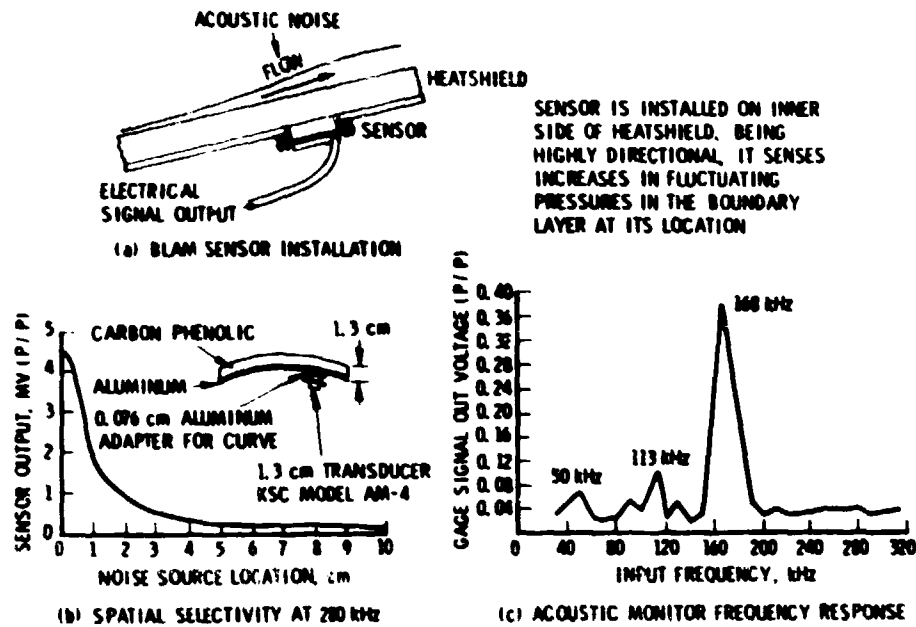


Figure 5-23. BLAM Detector Principle of Operation

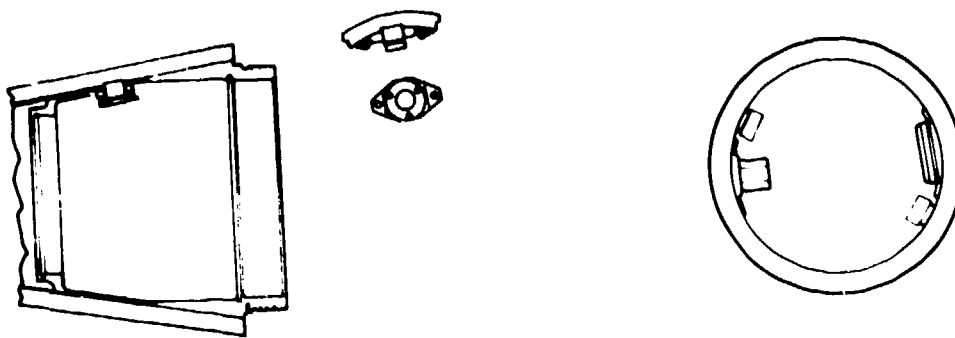


Figure 5-24 Transition Acoustic

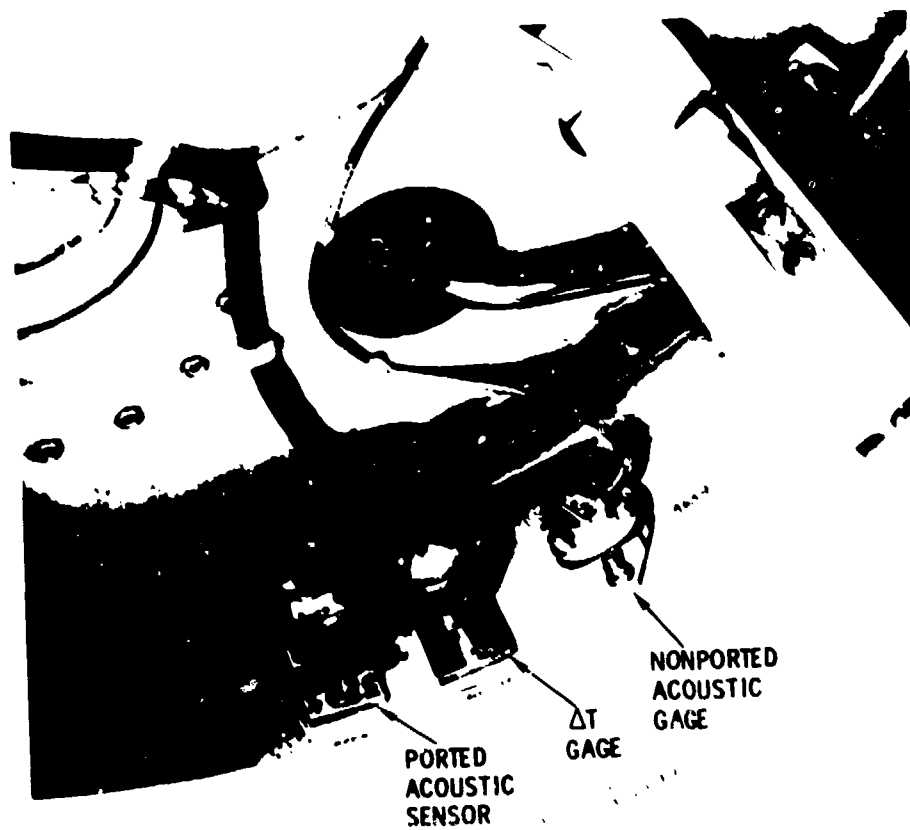


Figure 5-25. Internal RV

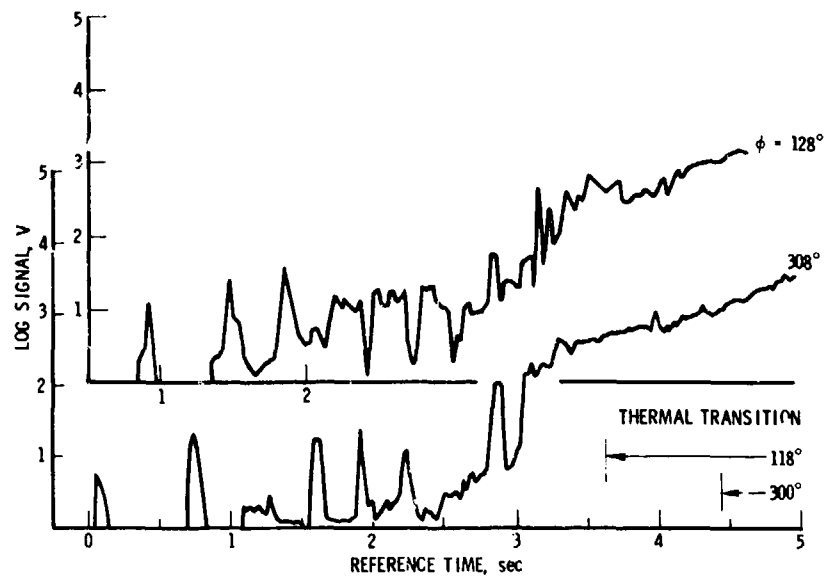


Figure 5-26. Kaman (BLAM) Transducer Output

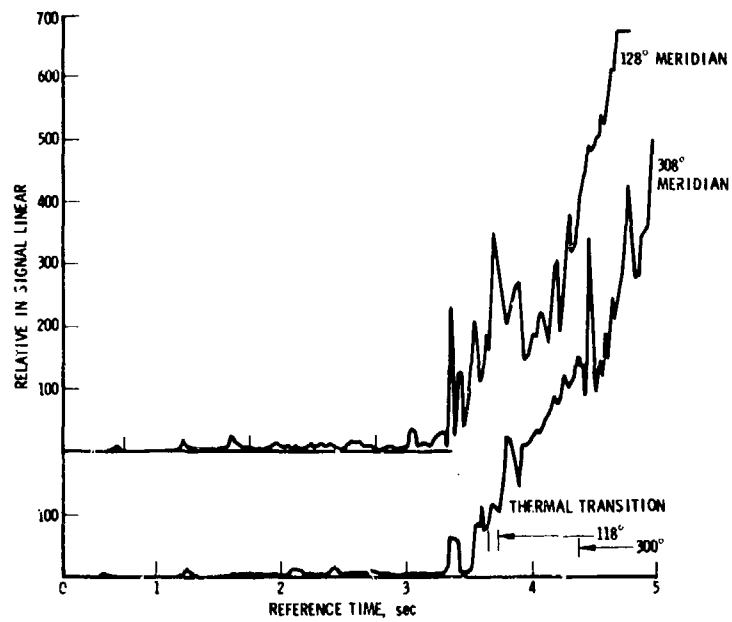


Figure 5-27. Kaman Detector

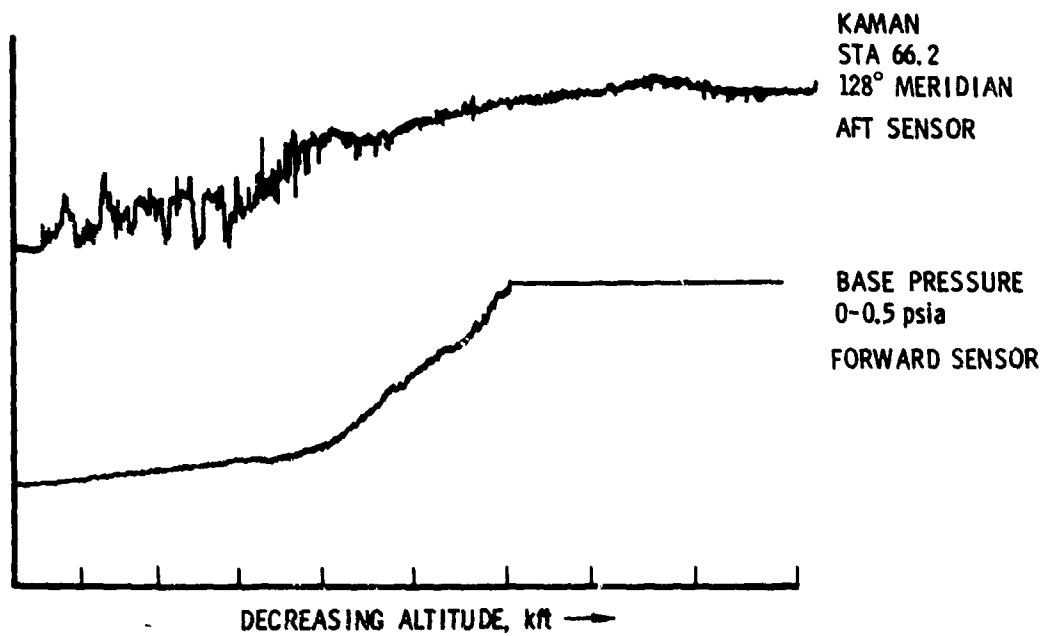
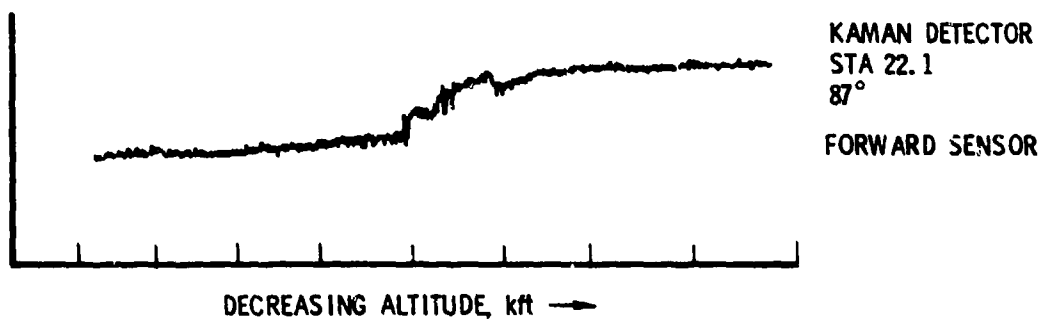


Figure 5-28. Nonported Acoustic Sensor

6. OFF-BOARD INSTRUMENTATION

The KREMS (Kiernan Reentry Measurement Site) is an instrument system composed principally of three radars and a variety of optical instrumentation and computer subsystems.³⁴ The PRESS (Pacific Range Electromagnetic Signature Studies) computer is used to transfer steering information from one instrumentation component to another or to provide initial steering information to any single radar or optical component of the system. The interaction between components is shown schematically in Figure 6-1. In addition to these major components, there exist a variety of lesser instrumentation at various points throughout the Kwajalein Missile Range (KMR). These are located on the map of the range (Figure 6-2) and will be discussed later.

The major radars are C-band, L- and S-band, and V or UHF systems. Probably the C- and L/S-band systems are the most important to SAMSO Programs since the longer wavelength radar is concerned primarily with long-range reentry vehicle detection; however, the short wavelength systems provide better spatial resolution, thereby giving better information relative to reentry vehicle performance and accuracy, which is the eventual proof of the success or failure of a SAMSO program. Thus, the C-band system (ALCOR) and the S/L-band system (TRADEX) are usually mandatory pieces of instrumentation on SAMSO flights. The 68-ft space frame radome of the ARPA-Lincoln C-Band Observable Radar (ALCOR) is shown in Figure 6-3 with the TRADEX antenna in the background. ALCOR was designed to study very wide bandwidth observables associated with targets reentering the atmosphere at high velocities. It has been in operation since January 1970.

ALCOR is a wideband C-Band radar with the exceptional range resolution of 0.5 m. This resolution is achieved by transmitting and processing the returns from a 512-MHz bandwidth linear chirp signal. Since the

bandwidth is so wide, real-time digital recording would normally be difficult. To alleviate this problem, the ALCOR receiver uses a time-bandwidth exchange technique that reduces the real-time bandwidth without loss of the range resolution corresponding to the original bandwidth. Using this method, data can be collected and recorded over a range interval of 90 m on each PRI (Pulse Repetition Interval).

A narrowband waveform covering a range window of 2.5 km is available for simultaneous use with the wideband tracker. The larger range window is useful for acquiring targets. ALCOR also has the ability to acquire and track the beacons that are flown on the major components of a target complex. Up to four different beacon codes can be accommodated by the system, giving ALCOR the capability to sequentially beacon track more than one object in a reentry complex. The characteristics of ALCOR are given in Table 6-1. The sensitivity of the radar is shown in Figure 6-4.

The TRADEX (Target Resolution and Discrimination Experiments) dual-frequency, high-power instrument radar can track in S- or L-band with simultaneous operation at the other frequency. A high-speed digital computer is the core of the radar system. Using real-time processing, the computer provides operational control of the radar by selection of the radar parameters, is an integral part of the range and angle tracking loops, drives displays, and controls the recording subsystem and processing.

The system operates coherently with a wide variety of wide bandwidth linear-frequency modulated pulses and pulse bursts available for transmission on both bands. At L-band, these waveforms are generated by an active exciter for the chirp waveform and tapped delay lines for the burst waveform. At S-band, the chirp and burst waveforms are generated passively by expansion networks. There are 13 receiver channels used to accommodate the various combinations of S/L-band transmitted chirp and burst waveforms.

The L/S-band digital-data recordings systems contain logarithmic amplifiers and phase detectors whose outputs are sampled by high-speed

Table 6-1. ALCOR Operating Parameters

	Wideband	Narrowband	Beacon
Frequency	5672 MHz	5664 MHz	Tuneable; 5416 to 5928 MHz
Transmitted Pulsewidth	10 μ sec	10 μ sec	Adjustable; 0.4 to 0.8 μ sec
Modulation	Linear FM Up Chirp	Linear FM Up Chirp	CW
Chirp Bandwidth	512 MHz	5.99 MHz	
Range Resolution	\sim 0.5 m	38 m	
Radiated Peak Power	2.25 mW		
PRF	11 to 200 pps; 389 pps Hi-PRF Mode		
Angle Track	Narrowband, Wideband, or Beacon		Antenna: 40-ft Cassegrainian
Range Track	Narrowband, Wideband, or Beacon		Feed: 4-Horn Monopulse
Data Recording	Digital Amplitude and Phase of Both Orthogonal Circular Polarizations and Metric Data, A-Scopes, RTI, Strip Charts		Transmit Polarization: RHC

analog-to-digital converters. At L-band the highest sampling is 10 MHz; at S-band it is 60 MHz. Phase and amplitude samples are accumulated, stored, and subsequently recorded on tape with simultaneous metric, mode, and status data. Pre-mission alignment and calibration of the radar is accomplished by built-in test equipment under computer control. There are test signals, continuous wave (CW) chirp pulses, and radio frequency (RF) chirp pulses available for insertion at various points in the receiver chain.

The characteristics of TRADEX are given in Table 6-2, and the sensitivity of TRADEX is given in Figure 6-5.

In addition to RV radar cross section (RCS) and metric data, ALCOR and TRADEX are used to gather environmental information. This function is of major importance in both clear air and weather environments. In weather-penetrating RV flights, these radars are used to measure the water content on the trajectory. In clear air flights they are used (particularly ALCOR) to ensure that a specified threshold water content is not exceeded prior to launch in the reentry corridor. The sensitivity of these radars relative to weather environments is shown in Figure 6-6.

The ARPA Long-Range Tracking and Instrumentation Radar (ALTAIR) (Figure 6-7) became operational in early 1970; it is a highly sensitive, dual-frequency radar that gathers coherent target return data simultaneously at VHF and UHF. Good long-range performance and excellent range resolution are obtained using both CW and linear frequency modulation pulse compression.

In operation, a central object in a multitarget complex is selected for computer-aided range and monopulse angle tracking at VHF (very high frequency) or UHF (ultrahigh frequency). The ALTAIR Recording System, with its separate computers, then acquires, range tracks, and records data on the multiple targets that are illuminated by the VHF and UHF beams. Digital data are recorded simultaneously on as many as 14 targets with a total capacity of up to 56×10^6 bps.

Table 6-2. TRADEX Operating Parameters

	L-Band	S-Band
Operating Frequency		
Center frequency	1320 MHz	2950.8 MHz
Transmitter dynamic bandwidth (-1 dB)	20 MHz	250 MHz
Power		
Peak (Typical)	1.75 MW	2.6 MW
Average (Maximum)	300 kW	60 kW
Duty Cycle (Maximum)	0.075	0.0165
Waveforms (Typical)		
Chirp		
Pulse width (μ sec)	50	9 (NB) 3 (WB)
Range Resolution (m)	285	15 (NB) 6.5 (WB)
PRF (Hz)	100 to 1500	100 to 1500
Doppler Resolution (m/sec)	$\lambda/2NT$	$\lambda/2NT$
Burst (WB)		
Pulse width (μ sec)	2	3
Range resolution (m)	15	6.5
Subpulse spacing (μ sec)	14 or 28	4 to 25
Number of subpulses	2 to 32	2 to 32
Doppler resolution (m/sec)	4054 to 126.7	6348 to 63.5
Antenna (Electrical)		
Beamwidth (3 dB, one way)	0.65°	0.25°
Efficiency	53 percent	42 percent
Gain (Center frequency)	48.2 dB	54.2 dB
Polarization		
Transmit	RC	RC
Receive	RC, LC	RC, LC
Axial Ratio	1.0 dB	1.0 dB
Sidelobes	-17 dB	-17 dB
Null Depth	30 dB	30 dB
Receivers		
Noise Temperature (Reference to antenna)	765°K	335°K
Dynamic Range (Instantaneous)	70 dB	70 dB

A series of modifications were completed in the spring of 1973 that gave the ALTAIR system an angle tracking and recording capability at UHF in addition to the existing VHF capability. Its operating parameters are given in Table 6-3.

The Army Optical Station at KREMS (Kierman Reentry Measurements Site) provides a test-bed for two passive infrared scanning radiometers (WAS and GBM) and an active infrared laser radar (LITE). The passive sensors will be operated to develop a data base on reentry bodies for the purpose of optical adjunct performance evaluation. The laser radar will be operated to develop a data base of laser cross sections of the various reentry bodies and the particulate wake.

In addition to gathering this cross-sectional data, the LITE system (Table 6-4) will be used as a practical demonstration of the techniques involved in using a laser radar in the KREMS environment; for example, experience will be gained from the reentry acquisition problem, system calibration, and handover from the laser to a microwave radar.

The wide-angle sensor (WAS) is a ground-based infrared system operating in the LWIR (long wavelength infrared) region. It has a wide field of view (WFOV), 6° in azimuth. The detector array consists of two vertical columns of 50 detectors offset in azimuth and interleaved in elevation. Each detector covers a field of 1×1 mrad. The scan frequency is variable in the following steps: 0.2, 0.3, 0.5, 0.8, 1.25, and 2.0 Hz. The operator is provided with a C-scope display of the detector outputs.

Data are recorded on an analog tape recorder and on digital tape with the NOVA Control and Recording System (NCRS). Boresighted LLTV-TV and 35-mm cameras provide additional supporting data.

The GBM-2 system provides high-resolution radiometric data on selected targets of interest. It is computer directed and when completely integrated into the AOS (acquisition of signal) will have backup acquisition and track capability. GBM-2 operated in both LWIR and SWIR (short wavelength infrared). It has an FOV 5 mrad in azimuth and 2.5 mrad in

Table 6-3. ALTAIR Operating Parameters

Waveforms	VCWL	VL	VS	VCW	UCWL	UL	US	UCW
Pulse Length (μ s)	30	30	6	0.25	16	15	3	0.1
Modulation	--	FM	FM	--	--	FM	FM	--
Bandwidth (MHz)	0.05	7	7	7	0.06	17.6	17.6	17.6
Range Resolution (m)	4500	38	38	38	1200	15	15	15
Peak Power (MW)	7	7	7	7	17	17	17	17
Average Power (kW)	78	78	62	5.2	101	95	76	5
PRF (pps)	40 to 372	40 to 372	40 to 1488	40 to 2976	40 to 372	40 to 372	40 to 1488	40 to 2976
Range (km) for single 2 pulse S/N = 0 on 1 m	3650	3550	2400	1060	5800	4700	3200	1340
Angle Track:	VHF or UHF			Antenna:		150-ft paraboloid with frequency selective subreflector		
Range Track:	VHF or UHF			Feed:		VHF - Focal point five horn monopulse UHF - Cassegrainian four horn monopulse		
Data Recording:	14 targets with amplitude and phase of LC, RC, AZ, and EL for both VHF and UHF along with metric information			Beamwidth:		VHF - 3° UHF - 1°		
				Transmit Polarization:		RHC		

Table 6-4. LITE Operating Parameters

Wavelength	Infrared
Pulse Length	20 nsec
Peak Power	60 MV
Average Power	36 W
PRF	30 pps
Beam Width	100 mrad
Range Track (active resolution)	Laser Receiver 4 m
Angle Track (passive resolution)	Focal plane TV (0.4-1.1 μm) 50 mr
Telescope	24-in. Cassegrainian
Data Recording	Digital Laser return amplitude Mount angle Kalman commands Tracking errors Housekeeping information

elevation and a collecting aperture of 46 cm. Data recording is digital using PCM (pulse code modulation) with analog backup using FM (frequency modulation). The sensor array consists of 52 detectors sensitive to the 2 spectral bands.

The LITE transmitter is a Nd:YAG laser operating at 1.06 μm , and the receiver is a 24-in. diameter telescope using a silicon avalanche photodiode as a detector at the focal plane. Also at the focal plane, which is divided by a dichroic mirror, is a TV vidicon. Angle track is established passively using the TV image, and range track is established actively using the detected laser return. The angle tracker's FOV is a circle 4 mrad in diameter; the laser receiver's FOV is approximately 270 mrad.

The LITE will be pointed by FRESS pointing commands for acquisition of the target. Once the target is visible to the TV receiver the system will go into a self-track mode.

Data are recorded digitally under control of the real-time program that resides in the LITE's MODCOMP computer. The image produced by the tracking TV is recorded on an IVC video tape recorder. A boresighted surveillance TV provides additional supporting data. This TV is fitted with a zoom lens that is continuously adjustable from 3° to 30° FOV.

A possible future ABRES use for the LITE sensor is in a direct measurement of a clear air environment; i. e., to ascertain if less than specified threshold of water content exists at altitude in the reentry corridor before launch or after splashdown. The sensitivity of LITE is shown in Figure 6-8. Note that it is about two orders of magnitude better than ALCOR.

A rather unusual piece of instrumentation available at Kwajalein is the ABRES weather aircraft (Figure 6-9). The Lear jet, with an operating ceiling of 45 kft, is used to "calibrate" ALCOR or TRADEX to the particular type of environment that exists at altitudes in the reentry corridor. This is accomplished by using the MPS-36 at Kwajalein Missile Range (KMR) to track the Lear aircraft during a "sampling" run. This tracking information is processed in the Kwajalein CDC-6600 computer producing steering information required to aim ALCOR or TRADEX to a point directly in front of the Lear. Consequently, the radar measures the reflectivity in a range gate in front of the sampling aircraft, which is in turn measuring the water content of the environment. Thus, the measured reflectivity is "calibrated" to the cloud water content, and radar measurements at spatial points not sampled by the aircraft can be evaluated in terms of water content.

The instruments aboard the Lear are primarily "particle counter" types that determine one or two dimensions of the ice crystal or water droplet and catalog them in size ranges from 2 to 5000 μm . For such a large size range, three different instruments are required. This information is periodically fed into an onboard computer that calculates mass from the measured particle distributions. This mass information and the distributions are telemetered to the ground. In addition to the size measurement, various "housekeeping" information is available; i. e., position,

heading, air speed, temperature, altitude, etc. The particle and housekeeping information is taped and can be reduced further with more complex algorithms during ground processing.

In addition to the above major pieces of instrumentation, the following auxiliary equipment is available at KMR and is located as shown in Figure 6-2:

- a. SDR (Splash detection radar) - Used to locate impact of the RV in the lagoon or near ocean. Resolution is on the order of the diameter of the "plume" ejected when the RV impacts the water surface.
- b. MPS-36 S-band radars used primarily for aircraft control but can be used to track beacon-equipped RVs.
- c. WSR-57 S-band weather radar used to estimate the severity, location, and direction of motion of weather situations.
- d. RADOTS A complex array of gimbal-mounted camera equipment steered by the KREMS radar. System photographs the RV relative to a fixed geographical location so that the trajectory can be reconstructed from the object location on the film and recorded gimbal position.
- e. BC Ballistic cameras fix-mounted and bore-sighted to a given geographical position. Trajectory reconstruction is accomplished by the RV "streak" on the film compared to the boresight information and/or the celestial background.
- f. TM Telemetry antenna that auto track the radiating object. Parabolic dishes range from 10 to 24 ft and are capable of receiving any RV transmittable frequency.

In summary it is clear that this brief description of the KMR equipment can never do technical justice to the complexity of it. However, it is hoped that the reader will gain some feeling from this description to aid him in designing or tailoring his particular experiment to the assets of the KREMS system.

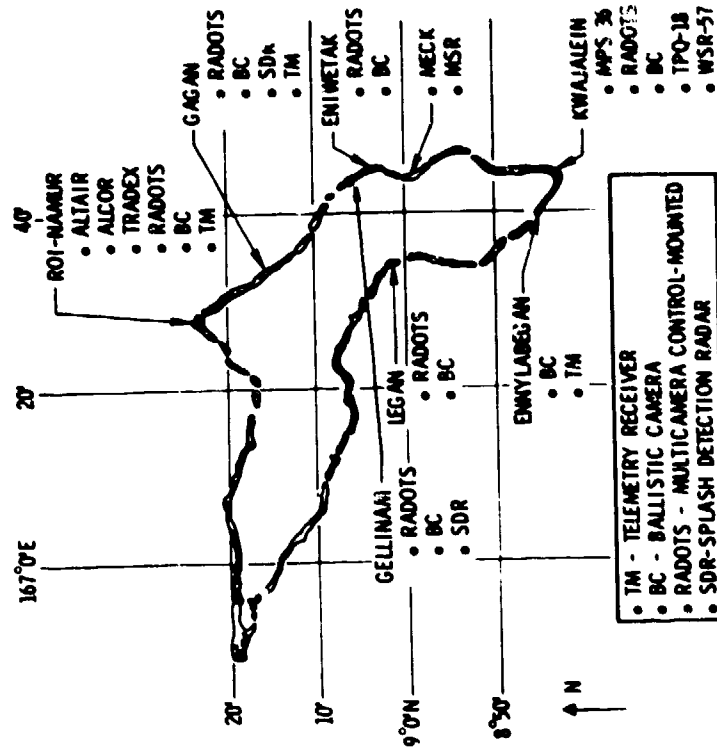


Figure 6-2. Kwajalein Missile Range

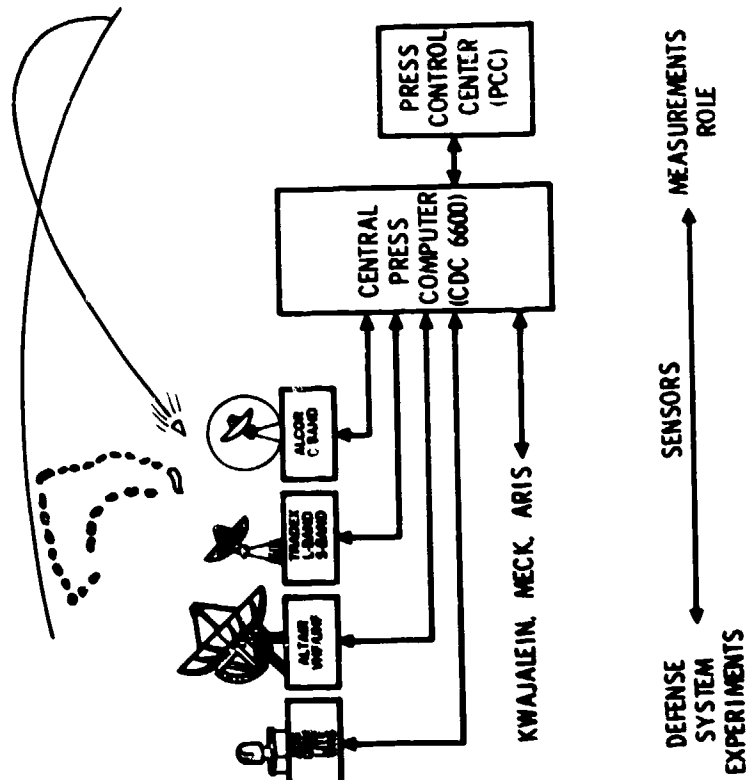


Figure 6-1. KREMS Instrumentation



Figure 6-3. ALCOR

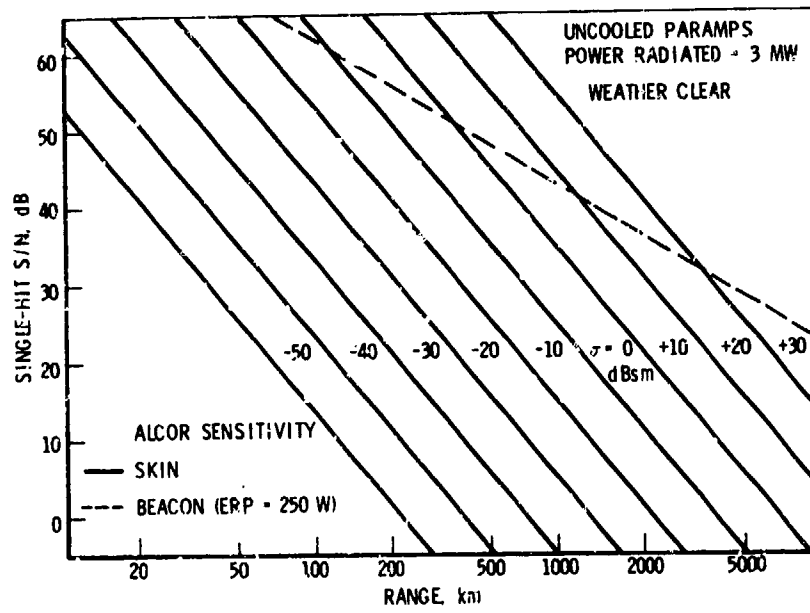


Figure 6-4. ALCOR Sensitivity

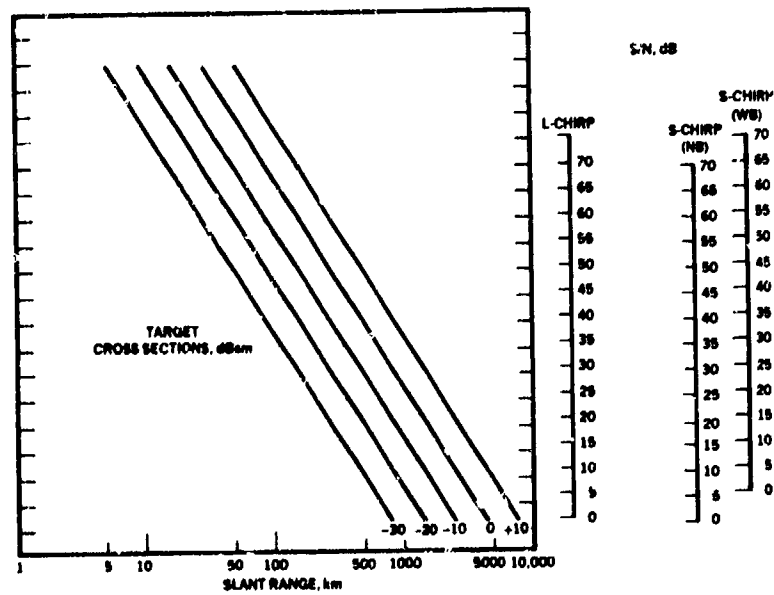


Figure 6-5. TRADEX Sensitivity

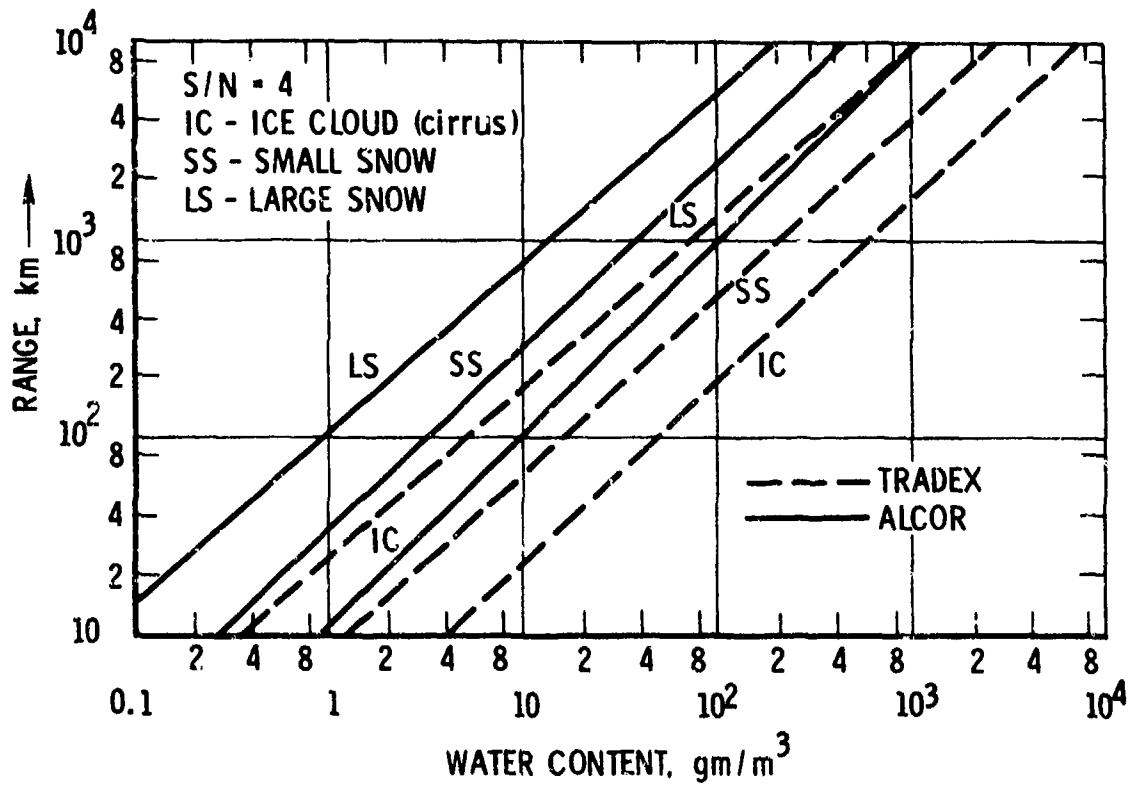


Figure 6-6. ALCOR/TRADEX Threshold Water Content Levels



Figure 6-7. ALTAIR

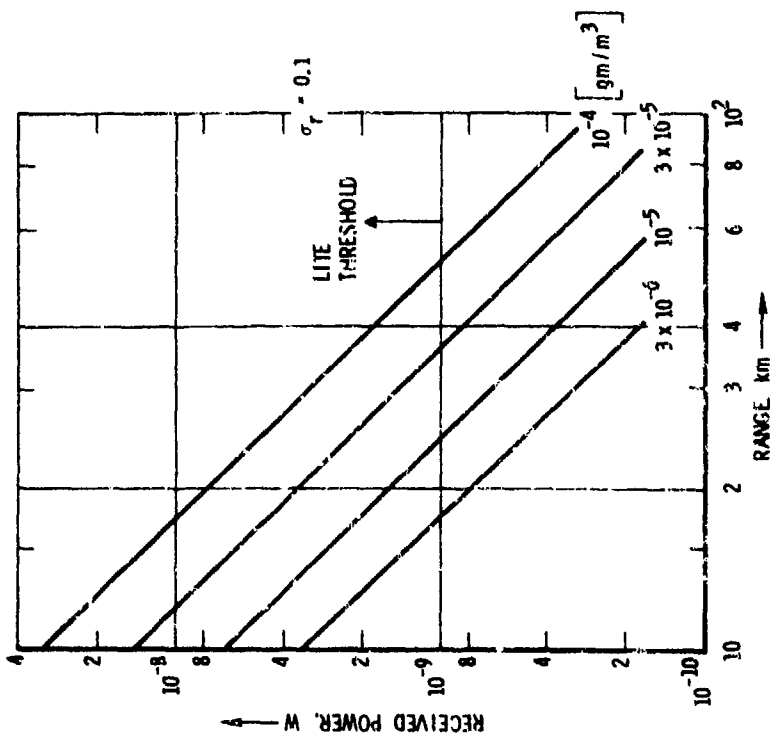


Figure 6-8. LITE Sensitivity to Ice Cloud

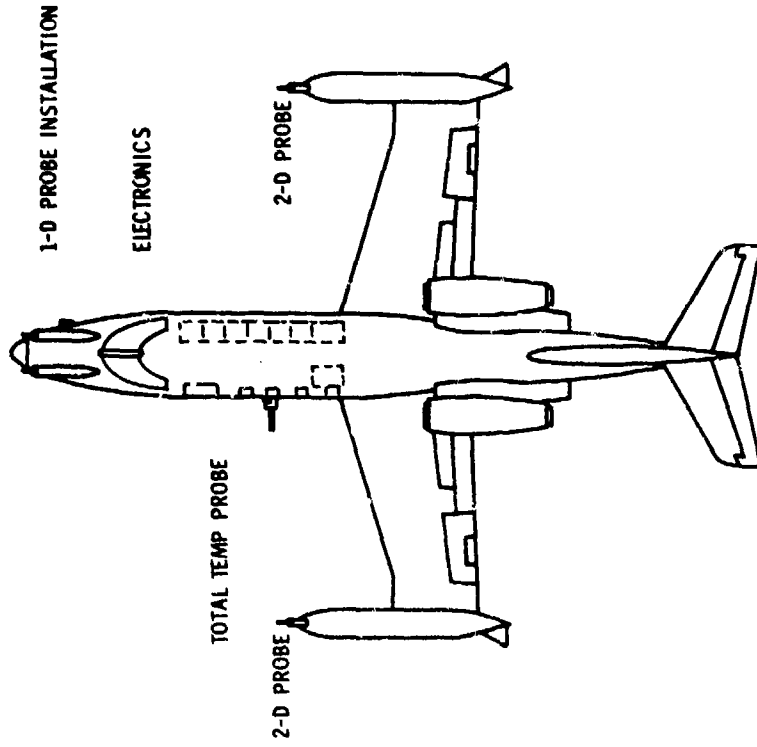


Figure 6-9. High-Altitude Weather Aircraft

7. INSTRUMENTATION ASPECTS OF FUTURE REENTRY TESTING

In planning the program for reentry system R&D for the next decade, the primary objectives will continue to be in the areas of defense penetration and of survival with accuracy in natural and hostile environments. However, one can expect to see an increasing emphasis on maneuvering RVs, as opposed to ballistic RVs, due to the potential deployment of high-performance interceptors and to the need for high accuracy.

Ballistic reentry technology is reaching a mature plateau in many areas due to recent activities and achievements. One critical area remaining is reentry performance in adverse weather.

7.1 WEATHER EFFECTS ON REENTRY VEHICLE PERFORMANCE

In recent years, our understanding of the phenomena that change the performance of an RV when it flies through clouds of water, ice, or snow particles has improved very rapidly. Basically, there are changes induced in the surface roughness and nose shape that alter, usually increasing, the drag force so that the vehicle falls short of its intended impact point.

It should be admitted at the outset that there is little hope that these phenomena can be made the subject of precise predictions for operational ballistic RVs. Our lack of knowledge of the precise meteorology that will exist when the vehicles arrive at the target area will preclude the inclusion of an accurate bias in the targeting software. At best we can only include a statistical correction of the same nature currently used for seasonal winds and density. Meanwhile, we will attempt to design our vehicles to be as insensitive to adverse weather effects as possible.

An alternative approach is to add some form of aerodynamic control to the vehicle. The two ends of the spectrum are full three-axis

control and single-axis drag modulation and some inertial instrumentation with the objective of flying an inertial path independent of the ambient weather. In this event, the weather problem reduces to ensuring that the vehicle has sufficient thermal protection to survive to impact.

For either approach in the R&D flight test phase, we need to correlate vehicle shape and performance changes with the actual weather environment on the reentry path. This latter item is difficult to achieve with the required accuracy. Currently, the technique consists of flying aircraft in the reentry corridor, before and after the event, to sample and measure the cloud content that is correlated with the radar measurements of particle reflectivity along the actual trajectory. The accuracy of this process is thought to be about a factor of 2; that is, the environment is within 50 percent less and 100 percent more than the devised value.

To do better than this, one probably needs to measure the environment from the vehicle itself. The simplest technique would be to record the history of particle impacts at certain locations on the vehicle surface with some form of accelerometer that has been calibrated with typical particle impacts in a ground facility. However, the flow field in flight moderates the mass and velocity prior to surface impact in a complex manner that jeopardizes the accuracy of this technique. Nevertheless, this technique could be valuable as a qualitative indication of weather encounters at altitudes higher than those at which the sampling aircraft operates where just a few impacts may sufficiently roughen the nosetip to cause premature transition.

It would be preferable to measure the number, size, and shape of the particles that pass through a certain area just outside the vehicle's flow field. Various radar and laser devices have been considered, for example Figure 7-1, but none have been developed for flight application.

7.2 COMMUNICATION TO AND FROM REENTRY VEHICLES

Looking at the longer term future, it is likely that operational RVs will become more complex to take full advantage of real-time data

in the battle area. Satellite systems could communicate guidance data to update the position of the RV or could provide command and control data to modify the characteristics of the preset mission. Additionally, RVs may be made to communicate with each other to permit trajectory modifications in the event that the first vehicles to reenter fail in their mission due to reliability problems, interception, etc.

Such increases in the flexibility of operational use will become possible when maneuvering RVs are part of the operational force. They can have a sufficiently large footprint of impact positions to permit in-flight retargeting over a significant area of target locations.

The simplest type of data one would need from a maneuvering vehicle would be a good guidance discrete just prior to the preset fuzing time, proving that the vehicle had reached its designated target, together with a discrete that the fuzing sequence had been initiated. Many additional elaborations may be feasible for indicating interceptor launch, nuclear kill, weather effects, etc., but in all cases the data content would be simple.

Electromagnetic communication through the base region will be necessary, preferably over a range of frequencies and aspect angles, as well as altitude and velocity conditions. Presently, our knowledge of the plasma distribution in the base area and its effects on telemetry communication is quite rudimentary. In fact, recent flight tests have provided some surprises to our understanding of base antennas for fuzing purposes.

The base flow field is complex particularly when electromagnetic, as well as aerodynamic, properties must be considered. Also in the low-altitude regime of interest, ablation products will add to the electron concentration and to the signal attenuation. In the R&D phase, the simplest experiment will be transmission from a base antenna to a telemetry aircraft; however, more complex experiments with base booms carrying pressure, temperature, and electron concentration probes may be required.

Of course, the transmitted signal must be received by subsequent incoming RVs, whose antennas may also be subject to plasma effects.

Also, this may be transmitted to distant satellites to communicate mission success back to the command authority. In the opposite direction, satellite transmissions of accurate positional data (e.g., from the Global Positioning System) may be received by base antennas to update the guidance platform and improve the accuracy of the impact point.

For applications like the above, we shall need to improve our knowledge of electron concentrations in the vehicle's flow field and of plasma effects on electromagnetic transmission over a range of frequencies and vehicle trajectory conditions.

7.3 INCREASED USE OF GROUND FACILITIES

Our interest in developing ground test facilities that more closely simulate the reentry environment is likely to continue in the foreseeable future. For one thing, the cost of reentry flight testing continues to rise, and it already consumes the major part of the ABRES budget. Sometime in the next five years it is expected we will use up the remainder of our stockpile of Minuteman I boosters, and the replacement booster is likely to be even more expensive.

Furthermore, there are beginning to be political implications that missile tests in general should be limited to slow the development of more effective strategic systems.

Of course, we must continue to flight test as a final check on each design concept, but we will attempt to gather more of the design data base from ground tests. For example, we are currently attempting to gather comparative erosion data on several nosetip materials by reentering four small RVs simultaneously at KMR. To what extent could this data be obtained from ground facilities?

At the Arnold Engineering Development Center (AEDC) the 1000-ft ballistic range G has been equipped with a removable guided rail track and recovery system, allowing launch of 2-in. diameter models at 18,000 ft/sec with undamaged recovery of complex model structures. The flight time is long

enough to produce measurable ablation and/or erosion; the latter is generated by flight through closely controlled dust (and soon ice and snow) particles at pressures and velocities close to those experienced in flight tests.

Extremely accurate instrumentation systems, including laser photography and low temperature photopyrometry, allow detailed evaluation of ablation and erosion histories for each model as well as generation of comparative performance data for both carbonaceous (passive) and transpiration-cooled thermal protection systems. Scale-up of similar facilities may be necessary to allow tests of larger sized components if flight opportunities become scarce. It will probably be desirable to increase the amount of instrumentation in or on the models themselves to fully define the environment and performance for each test. This would require much smaller, extremely high acceleration, vibration-resistant instrumentation packages.

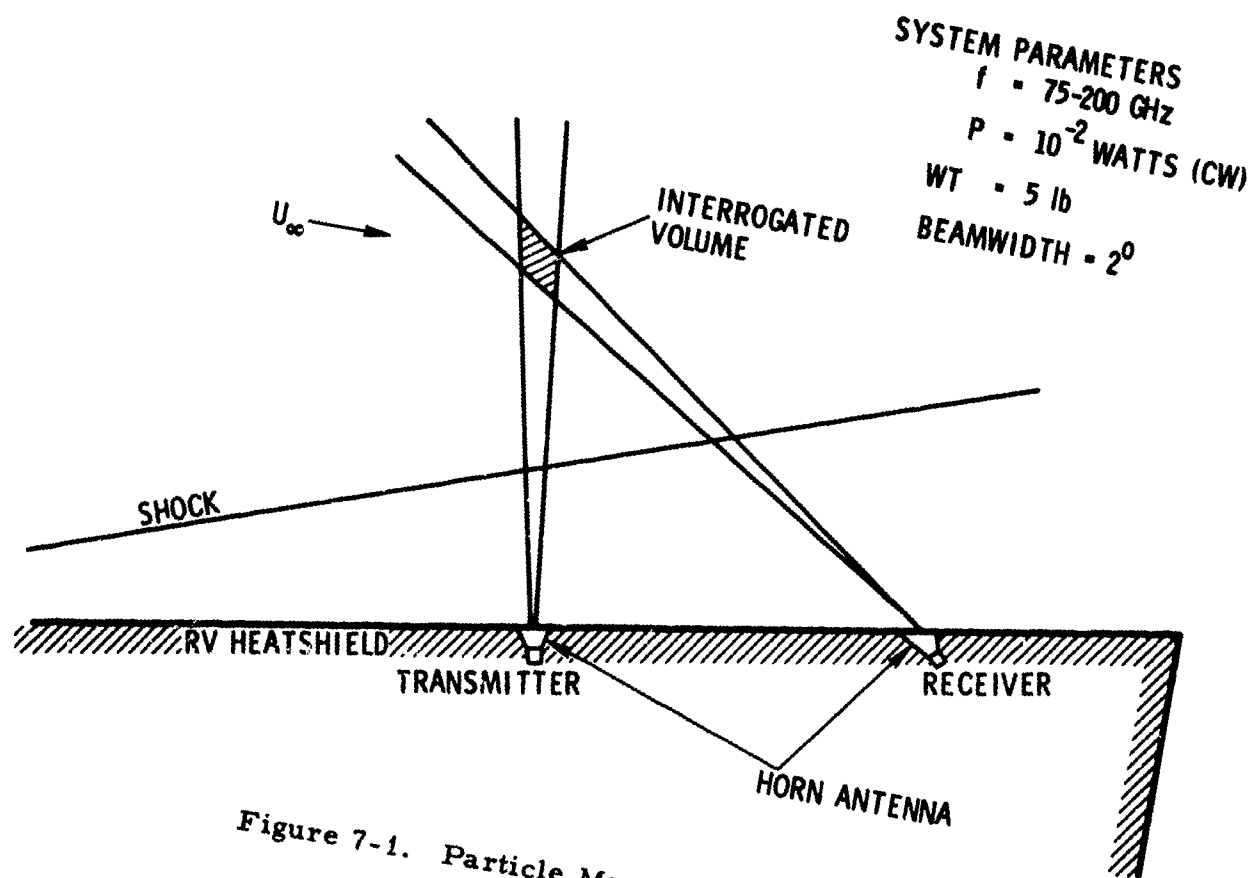


Figure 7-1. Particle Measurement Radar

REFERENCES

1. P. J. Legendre, "Reentry Vehicle Nosedip Instrumentation", ISA Paper ASI 75208 (1-17), Presented at the 21st International Instrumentation Symposium, Philadelphia, May 19-21, 1975.
2. R. D. McGunigle and M. Jennings, "Ultrasonic Ablation Recession Measurement System", ISA Paper ASI 75120 (19-24), Presented at the 21st International Instrumentation Symposium, Philadelphia, May 19-21, 1975.
3. A. J. Armini and S. N. Bunker, "A Re-Entry Vehicle Nosedip Shape Change Sensor", ISA Paper ASI 75211 (25-35), Presented at the 21st International Instrumentation Symposium, Philadelphia, May 19-21, 1975.
4. V. V. Verbinski et al., "Neutron Backscatter Ablation Gage", ISA Paper ASI 75212 (37-47), Presented at the 21st International Instrumentation Symposium, Philadelphia, May 19-21, 1975.
5. R. Eichorn et al., "A Resonant Acoustic Technique for Measuring Reentry Nosedip Recession", ISA Paper ASI 76227 (147-154), Presented at the 21st International Instrumentation Symposium, San Diego, May 25-27, 1976.
6. M. R. O'Gara and R. D. McGunigle, "Aerodynamic Noise Spectrum and Acoustic Emission Measurements on Flight Nosedips, Using a Second Generation Ultrasonic Ablation Recession Gauge", ISA Paper ASI 76228 (155-160), Presented at the 21st International Instrumentation Symposium, San Diego, May 25-27, 1976.
7. V. J. Orphan et al., "Radiometric Ablation Sensor for Measuring Shape Change of Re-entry Vehicle Nosedips", ISA Paper ASI 76260 (417-426), Presented at the 21st International Instrumentation Symposium, San Diego, May 25-27, 1976.
8. P. L. Ritchie et al., "Carbon Fiber Reinforced Graphite Nose Recession Overview", ISA Paper ISBN 87664-362-4 (21-28), Presented at the 22nd International Instrumentation Symposium, Las Vegas, May 1-5, 1977.
9. J. W. Metzger, "Optimization Experiments with Sensor Implants in Carbon-Carbon Nosedips", ISA Paper ISBN 87664-362-4 (29-40), Presented at the 22nd International Instrumentation Symposium, Las Vegas, May 1-5, 1977.

10. W. A. Fitzgerald, Jr. and A. W. Mitton, Jr., "Scintillator/Photomultiplier Ablation Detector (SPAD) for Use in Reentry Vehicles", ISA Paper ISBN 87664-362-4 (41-50), Presented at the 22nd International Instrumentation Symposium, Las Vegas, May 1-5, 1977.
11. S. N. Bunker and A. J. Armini, "Many Ray Noretip Ablation Sensor Design", ISA Paper ISBN 87664-362-4 (51-60), Presented at the 22nd International Instrumentation Symposium, Las Vegas, May 1-5, 1977.
12. A. Hanawalt et al., "TDV FWCC Noretip Experiment", ISA Paper ISBN 87664-362-4 (61-70), Presented at the 22nd International Instrumentation Symposium, Las Vegas, May 1-5, 1977.
13. P. J. Legendre et al., "Ablation Instrumentation Effects on Carbon-Carbon Noretip Performance", ISA Paper ASI 74224 (97-112), Presented at the 20th International Instrumentation Symposium, Albuquerque, May 21-23, 1974.
14. P. J. Legendre and D. C. Howey, "Ablation Instrumentation Effects on Carbon-Carbon Noretip Performance-Phase II", ISA Paper ASI 75222 (113-120), Presented at the 21st International Instrumentation Symposium, Philadelphia, May 19-21, 1975.
15. P. J. Legendre et al., "Instrumentation Installation Effects on the Performance of Tungsten Noretips", ISA Paper ASI 76226 (137-146), Presented at the 22nd International Instrumentation Symposium, San Diego, May 25-27, 1976.
16. J. I. Slaughter, Reentry Vehicle Heat Shield Sensor Techniques (U), Report TOR-469(5108-27)-5, The Aerospace Corp., El Segundo, Calif. (July 28, 1964) (C).
17. Carbon-Carbon Noretip Development Program Post-Test Summary Report, Task 2.4 - Instrumentation Study and Tests, Report AVSD-0059-73-CR, Avco Corp., Wilmington, Maine (26 January 1973).
18. J. G. Kyser and D. E. Wright, RV Ablation Sensor - A Gamma Ray Backscatter Technique, Report ER-80146, Gianni Controls Corp., Duarte, Calif. (5 March 1964).
19. D. S. Gickin et al., Review of Sensor Concepts for Application to Advanced Heat Shield Materials, Document 64SD757, General Electric Co., Philadelphia (6 July 1964).

20. A. Robinson et al., "A Backscatter Radiation Ablation Gage for Thick Reentry Vehicle Noses", Paper presented at the 21st International Instrumentation Symposium, Philadelphia, May 19-21, 1975.
21. P. J. Legendre and G. T. Chase, "The Operational Performance of Reentry Vehicle Heatshield Thermodynamic Instrumentation", ISA Paper ASI 73216 (85-86), Presented at the 19th International Instrumentation Symposium, Las Vegas, May 21-23, 1973.
22. J. M. Cassanto et al., "Use of a Miniature Solid State Pressure Transducer for R/V Flight Test Application", ISA Paper ASI 74210 (33-34), Presented at the 20th International Instrumentation Symposium, Albuquerque, May 21-23, 1974.
23. R. Lenke and J. C. Kicks, "A New Class of Miniature Pressure Transducers for Reentry Vehicle and Ballistic Applications", ISA Paper ASI 74211 (45-50), Presented at the 20th International Instrumentation Symposium, Albuquerque, May 21-23, 1974.
24. R. B. Clark and R. M. Grabow, "Performance of Multiwire Isothermal Thermocouple Sensors", ISA Paper ASI 74225 (113-122), Presented at the 20th International Instrumentation Symposium, Albuquerque, May 21-23, 1974.
25. J. M. Cassanto, "A Miniaturized Differential Pressure Transducer with Time Constant for R/V Flight Test Application", ISA Paper ASI 76229 (161-170), Presented at the 21st International Instrumentation Symposium, Philadelphia, May 19-21, 1975.
26. G. F. Wright and D. D. McBride, "In-Flight Measurements of Thermal Response of a Carbon Phenolic Heatshield", ISA Paper ISBN 87664-362-4, Presented at the 22nd International Instrumentation Symposium, Las Vegas, May 1-5, 1977.
27. J. V. Beck, "Thermocouple Temperature Disturbances in Low Conductivity Materials", Trans. ASME 84 (2), Series C, 124 (May 1962).
28. V. D. Peckham and T. F. V. Meagher, "Boundary Layer Acoustic Measurements in RV Flight Tests", ISA Paper ISBN 87664-362-4 (375-379), Presented at the 22nd International Instrumentation Symposium, Las Vegas, May 1-5, 1977.
29. C. B. Anderson, Thermal Response of Charring Ablator Heat Protection Systems Programmed for the IBM 7074 Digital Computer, Report TOR-669(S6855-20)-3, The Aerospace Corp., El Segundo, Calif. (February 1966).

30. P. J. Legendre, Design Parameters Affecting the Accuracy of Isothermal Thermocouples, E.M.E. Thesis, USC, Los Angeles (June 1974).
31. R. B. Lyons, "Cadmium Telluride Detector Development and Use in Reentry Vehicle Applications", Revue de Physique Applique, Tome 12, 385 (Février 1977).
32. S. Brelant et al., "Improvements in the Manufacture of CdTe Gamma Ray Detectors," Revue de Physique Applique, Tome 12, 141 (Février 1977).
33. J. M. Cassanto et al., "Reentry Vehicle Flight Test Pressure Measurements (Steady State and Fluctuating): An Overview Progress Report," ISA Paper ISBN 87664-362-4, Presented at the 23rd International Instrumentation Symposium, Las Vegas, May 1-5, 1977.
34. An Introduction to Project PRESS at the Kiernan Reentry Measurements Site, KREMS Booklet (15 July 1977).